Modeling and Design Optimization of Medium Frequency Transformers for Medium-Voltage High-Power Converters

Thèse N° 7511

Présentée le 9 août 2019

à la Faculté des sciences et techniques de l'ingénieur
Laboratoire d'électronique de puissance
Programme doctoral en energie

pour l'obtention du grade de Docteur ès Sciences

par

Marko MOGOROVIC

Acceptée sur proposition du jury

Prof. S. Haussener, présidente du jury
Prof. D. Dujic, directeur de thèse
Prof. T. Thiringer, rapporteur
Dr G. Ortiz, rapporteur
Prof. J. Biela, rapporteur

2019

ÉCOLE POLYTECHNIQUE
FÉDÉRALE DE LAUSANNE

École Polytechnique Fédérale de Lausanne
Power Electronics Laboratory
Station 11
1015 Lausanne, Switzerland

http://pel.epfl.ch

Dedicated to my family

Abstract

Novel high-power medium-voltage converter technologies offering galvanic insulation are needed to support the development of the emerging medium-voltage direct-current grids and further improve the performance of various other applications such as traction, renewable energy and e-mobility. With the recent advancements in the power semiconductor industry, resulting in faster and more efficient switches with extended voltage and current capabilities, these converters, often referred to as solid-state transformers (SSTs) or power electronic transformers (PETs), have become increasingly attractive.

Besides the power semiconductor modules, the central component of any such converter, having a significant impact on its efficiency and power density, is the medium frequency transformer (MFT) that provides the necessary galvanic insulation and input-output voltage matching. However, the progress of the magnetic components has not been following the same pace as the semiconductor industry. In contrast to traditional line frequency transformers (LFTs), normally operating at low grid frequency with sinusoidal voltage and current excitation, MFTs operate on higher switching frequencies with square voltage and in general non-sinusoidal current waveforms, characteristic for the given power electronic converter topology. This has implications on the transformer losses and dielectric withstand requirements. Moreover, a correct design of electric parameters is essential for the proper operation of these converters and therefore imposes strict requirements on the accuracy of the corresponding models. Unlike the traditional LFTs, MFTs have not yet reached the technological maturity, leaving many areas open for research.

To that end, this thesis focuses on the technical challenges tied to modeling and design optimization of the MFTs for the emerging SSTs. The available technologies and materials, suitable for medium-frequency operation are identified and classified in respect to different application requirements, thus defining the design space. A detailed analysis and modeling of all the relevant phenomena governing the MFT electrical behavior as well as limiting the operation and design range is performed. A synthesis of all these models is done in form of a design optimization algorithm capable of generating the set of all feasible transformer designs. Moreover, design filters are developed allowing to interactively search for the most preferable design alternatives in terms of hot-spot temperatures, weight, volume and efficiency. As a proof of concept, a 100kW, 10kHz MFT prototype has been realized according to the optimal specifications resulting from the proposed design optimization tool. The accuracy of the utilized models was confirmed via thorough testing, including: electric parameter identification, partial-discharge test, full-power loading test and an extensive thermal run within the realized back-to-back resonant test setup.

With the established design methodology and reliable models, a technology coordination and an MFT design sensitivity study has been performed on the SST level. A 0.5MW, 10kV input-series output-parallel series resonant converter based topology has been selected for the case study, taking into account different available semiconductor ratings and the resulting converter modularity. This study has shown that, considering the available technologies and materials, the expected MFT power density reaches its apex at around 10 – 20kHz. While modern wide-band-gap semiconductors will for sure increase the efficiency and power density of the converter stage, this result indicates that further size reduction of the magnetic components above these frequencies will only be possible through improvements in the materials - providing core and winding materials with better high frequency loss characteristic.

Keywords: *Solid State Transformer, Medium Frequency Transformer, Modeling, Design, Optimization*

Zusammenfassung

Neuartige Hochleistung-Mittelspannungswandler mit galvanischer Isolation sind erforderlich um die Entwicklung der entstehenden Mittelspannungsgleichstromnetze zu unterstützen und die Leistung verschiedener anderer Anwendungen – wie elektrischer Antriebe, erneuerbare Energien und Elektromobilität – weiter zu verbessern. Mit den jüngsten Fortschritten in der Leistungshalbleiterindustrie, die zu schnelleren und effizienteren Schaltern mit erweiterten Spannungs- und Stromfähigkeiten geführt hat, sind diese Wandler, die oft als Solid State Transformer (SSTs) oder Power Electronic Transformer (PETs) bezeichnet werden, immer attraktiver geworden.

Neben den Leistungshalbleitermodulen bildet der Mittelfrequenztransformator (MFT), der den Wirkungsgrad und die Leistungsdichte erheblich beeinflusst, die zentrale Komponente eines solchen Wandlers, der die erforderliche galvanische Isolation und Eingangs- / Ausgangsspannungsanpassung liefert. Der Fortschritt der magnetischen Komponenten verlief jedoch nicht so schnell wie in der Halbleiterindustrie. Im Gegensatz zu herkömmlichen Netzfrequenztransformatoren (LFTs), die normalerweise bei niedriger Netzfrequenz mit sinusförmiger Spannungs- und Stromerregung arbeiten, arbeiten MFTs bei höheren Schaltfrequenzen mit Rechteckspannung und im allgemeinen nicht-sinusförmigen Stromformen die für gegebene Leistungselektronik-Topologien charakteristisch sind. Dies hat Auswirkungen auf die Transformatorverluste und an die Anforderungen für die dielektrische Beständigkeit. Darüber hinaus ist eine korrekte Auslegung der elektrischen Parameter für den ordnungsgemäßen Betrieb dieser Umrichter unabdingbar und fordert eine hohe Genauigkeit der entsprechenden Modelle. Im Gegensatz zu herkömmlichen LFTs haben MFTs noch nicht die technologische Reife erreicht, so dass viele Bereiche für die Forschung offen bleiben.

Zu diesem Zweck konzentriert sich diese Arbeit auf die technischen Herausforderungen der Modellierung und Designoptimierung von MFTs, welche Bestandteil zukünftiger SSTs sind. Um einen Designraum zu definieren, werden die verschiedenen Technologien und Materialien die für den Mittelfrequenzbetrieb geeignet sind mithilfe unterschiedlicher Anwendungsanforderungen identifiziert und klassifiziert. Es wird eine detaillierte Analyse und Modellierung aller relevanten Phänomene durchgeführt um das elektrische Verhalten der MFTs zu definieren sowie den Betriebs- und Auslegungsbereich zu begrenzen. Die unterschiedlichen Modelle werden mithilfe eines Optimierungsalgorithmus vereint, welcher in der Lage ist die möglichen Transformatordesigns zu generieren. Zusätzlich werden Filter entwickelt, die es ermöglichen nach unterschiedlichen Parametern wie Hot-Spot-Temperaturen, Gewicht, Volumen oder Effizienz zu priorisieren. Als Proof of Concept wurde ein MFT-Prototyp mit 100kW und 10kHz realisiert, dessen optimierte Designparameter mithilfe des vorgeschlagenen Optimierungstools gefunden wurde. Die Genauigkeit der verwendeten Modelle wurde durch gründliche Tests bestätigt. Dazu gehören: Elektrische Parameter, Teilentladungstest, Belastungstest mit voller Leistung, sowie ein mehrstündiger thermischer Dauerlauf innerhalb des realisierten Back-to-Back Resonanz-Testaufbaus.

Mit der vorgestellten Designmethodik und den präzisen vorgestellten Modellen wurde auf SST-Ebene eine Technologiekoordination und eine MFT-Sensitivitätsstudie durchgeführt. Für die Fallstudie wurde eine auf Resonanzwandler basierende Topologie von 0.5MW, 10kV, Eingang-seriell und Ausgang-parallel ausgewählt. Dabei wurden die verfügbaren Halbleiterklassen und die daraus resultierende Modularität des Wandlers berücksichtigt. Diese Studie hat gezeigt, dass unter Berücksichtigung der verfügbaren Technologien und Materialien die erwartete MFT-Leistungsdichte ihren Höhepunkt bei 10 – 20kHz erreicht. Während moderne Halbleiter mit breiter Bandlücke die Effizienz und Leistungsdichte der Wandlerstufe sicher erhöhen werden, zeigt dieses Ergebnis, dass eine weitere

Größenreduzierung der magnetischen Komponenten durch eine zusätzliche Erhöhung der Arbeitsfrequenz nur durch eine Verbesserungen der Materialtechnologie möglich ist, so dass Kern- und Mantelmaterial bessere Charakteristiken bei hohen Frequenzen aufweisen.

Schlüsselwörter: *Solid State Transformer, Mittelfrequenztransformator, Modellierung, Design, Optimierung*

Acknowledgments

"Not all those who wander are lost"
J.R.R. Tolkien

The Ph.D. journey I undertook almost four years ago, was inspired by this quote. Along this journey a number of people directly or indirectly played a very important role and I would like to take this opportunity to acknowledge their efforts and support.

First of all, I would like to express my gratitude to Prof. Dražen Dujić for providing me the opportunity to do this research in the newly established Power Electronics Laboratory (PEL) at EPFL and showing his faith in my abilities as a researcher. His confidence and guidance over the last four years have helped me overcome many research challenges. As one of the first Ph.D. students in the lab, I had the opportunity to observe and learn from the challenges he faced in his effort to provide a relaxed yet highly efficient research environment in the laboratory. Apart from the scientific discussions, it was always a pleasure to exchange ideas with him on various topics.

I would like to thank Mr. Roland Wetter for all his help and advice concerning practical realization of the prototypes and test setups. He had a key role in helping me orient myself within the EPFL infrastructure and various facilities.

I would like to thank the team from the workshop Mr. Roland Dupuis and Mr. Karim Collomb for helping me with manufacturing of various mechanical components and their constructive advice that resulted in much better quality realization.

I would like to thank all the students who did their projects with me which directly or indirectly helped to increase the depth of certain conclusions.

I would like to thank Mr. Felix Moritz for proofreading and correcting the German version of the abstract.

I would like to thank the jury members, Prof. Sophia Haussener (EPFL), Prof. Jürgen Biela (ETHz), Prof. Torbjörn Thiringer (Chalmers University of Technology) and Dr. Gabriel Ortiz (ABB Switzerland) who agreed to evaluate my work, dedicated time for it and provided their valuable feedback that helped in improving the quality of the thesis.

Over the last four year, I have shared many wonderful experiences with and learned from all the members of PEL. I would like to thank them for all the long conversations and insights they have shared with me. It was truly a pleasure to spend all those times with them. On a personal note, I would also like to express my gratitude to all my friends in EPFL, Switzerland and all over the world. I would especially like to thank Ozrenko, Uzair, Ivo, Ivan, Igor and all the other guys who were always around for their support and close friendship.

In the end, I would like to thank my family for their constant support and unconditional love which was always the foundation of any of my achievements.

Lausanne, June 2019

Marko

List of Abbreviations

AC	alternating-current
BIL	basic lightning impulse
DAB	dual active bridge
DC	direct-current
DSO	distribution system operator
FEM	finite element method
GaN	gallium nitrite
GOES	grain oriented electrical steel
HVDC	high-voltage direct-current
LFT	line frequency transformer
MFT	medium frequency transformer
MVAC	medium-voltage alternating-current
MVDC	medium-voltage direct-current
PET	power electronic transformer
SDDM	statistical data driven models
Si	silicon
SiC	silicon carbide
SRC	series resonant converter
SST	solid-state transformer
ZVS	zero voltage switching

Contents

Abstract i

Zusammenfassung iii

Acknowledgments v

List of Abbreviations vii

List of Symbols vii

1 Introduction 1
- 1.1 Line Frequency Transformers vs Solid State Transformers 1
  - 1.1.1 Foreword 1
  - 1.1.2 Line Frequency Power Transformers 1
  - 1.1.3 Solid State Transformers 2
- 1.2 Applications and Requirements 3
  - 1.2.1 Traction 3
  - 1.2.2 Utility Grids 4
  - 1.2.3 MVDC Grids 5
- 1.3 Challenges 6
  - 1.3.1 Objectives of the Thesis 7
  - 1.3.2 Contributions of the Thesis 7
- 1.4 Outline of the Thesis 8
- 1.5 List of publications 9

2 Background and State of the Art 11
- 2.1 Transformer basics 11
- 2.2 MFT Scaling Laws: A Qualitative Analysis 13
- 2.3 Challenges 15
  - 2.3.1 Skin and proximity effect 15
  - 2.3.2 Edge Effect 16
  - 2.3.3 Thermal Coordination 17
  - 2.3.4 Accurate Electric Parameter Design 18
  - 2.3.5 Non-Sinusoidal Excitation 20
  - 2.3.6 Insulation Coordination 21
- 2.4 State of the Art 21
- 2.5 Summary 23

3 Design Optimization Process 25
- 3.1 A High-Level Description 25
- 3.2 Relevant Features and Specifications 26
  - 3.2.1 MFT Features and Specifications 26
  - 3.2.2 Additional Features 27
- 3.3 Design Space 28

3.3.1 Construction Types 28
3.3.2 Design Choices 29
3.3.3 Materials 33
3.4 Summary 36

4 Analytical Modeling 37
4.1 Introduction 37
4.2 Core Losses 38
4.2.1 Literature Review 38
4.2.2 Application of the IGSE 39
4.3 Winding Losses Modelling 41
4.3.1 Literature Review 41
4.3.2 Dowell's Model 41
4.3.3 Practical Application of Dowell's Model 44
4.4 Leakage Inductance Modelling 46
4.4.1 Literature Review 46
4.4.2 Dowell's Model 47
4.4.3 Practical Application of the Dowell's Model 49
4.4.4 FEM Analysis 49
4.4.5 Hybrid Leakage Inductance Model 50
4.5 Magnetizing Inductance 52
4.6 Thermal Modeling 53
4.6.1 Thermal Network Model Based on the 3D Transformer Geometry 53
4.6.2 Thermal FEM Analysis 56
4.7 Conclusion 57

5 Statistical Data-Driven Modeling 59
5.1 Introduction 59
5.2 Leakage Inductance Modelling Of Asymmetric Winding Structures 60
5.2.1 Proposed Modeling Method 61
5.2.2 Application of the Model 65
5.2.3 Experimental Verification 66
5.3 Local Electric Field Modeling Within MFT Insulation 67
5.3.1 Proposed Modeling 69
5.3.2 Simulation Results 71
5.4 Geometry Dependent Core Loss Modeling 72
5.4.1 FEM Analysis 73
5.4.2 Proposed Modeling Approach 75
5.4.3 Experimental Verification 80
5.5 Conclusion 81

6 Design Optimization 83
6.1 Literature Review 83
6.2 Design Optimization Algorithm 83
6.3 Optimal Design Selection 86
6.4 Conclusion 89

7 Proof of Concept **91**
7.1 MFT Prototype 91
7.2 Experimental Verification 92
7.2.1 Electrical Parameter Measurement 92
7.2.2 Electrical Measurements in a Resonant Test Setup 94
7.2.3 Thermal Measurements 97
7.2.4 Dielectric Withstand Test 98
7.3 Conclusions 99

8 Sensitivity Analysis of MFT Design **101**
8.1 Introduction 101
8.2 Converter Design 103
8.2.1 Selection of the number of cells 103
8.2.2 Cell Design 104
8.3 Quantitative Analysis of the MFT Design Trade-Offs 105
8.3.1 Scope Of The Analysis 105
8.3.2 Method of Analysis 107
8.4 MFT Design Analysis 108
8.4.1 Switching Frequency and Efficiency 109
8.4.2 Switching Frequency and Insulation Voltage 109
8.4.3 Optimal Number Of ISOP Connected Cells 110
8.4.4 Optimal Number Of Parallel Connected DC-DC Converters Within a Cell 114
8.5 Conclusion 116

9 Conclusion and Future Work **117**
9.1 Summary and Contributions 117
9.2 Overall Conclusions 119
9.3 Future Work 120

Appendices **121**

A Test Setup Instruments **123**
A.1 Used Instruments 123

1

Introduction

1.1 Line Frequency Transformers vs Solid State Transformers

1.1.1 Foreword

From the very early days of humanity, the progress of the society in general was always closely tied to the ability to tame and utilize the forces of nature. Already in the 3rd century BC the ancient civilizations were using the vertical water wheels to power the grain mills [1]. Primitive gear mechanisms were used to transfer the mechanical torque from one to the other, usually not more than a couple of meters. The complexity and immense transmission losses of these mechanical systems were restricting the power transfer to any real distances in a modern sense. It was only with the beginning of the electrification in the 19th century AC that the power transfer to some practical distances became possible. However, the early electrical systems were based on a relatively low-voltage direct-current which also featured a low transmission efficiency due to the high ohmic losses. At the same time an alternative mode of electrification, the alternating-current, emerges, leading to the so called war of the currents [2]. Starting in the 1880s, the alternating-current gained its key advantage over direct-current with the development of functional transformers that allowed the voltage to passively be ”stepped up” to much higher voltages for efficient transmission and then ”stepped down” to a lower end-user voltage, suitable for business and residential use [3]. This made the alternating-current power systems into a dominant technology for modern generation, transmission and distribution of the electrical energy.

1.1.2 Line Frequency Power Transformers

According to the definition in the international standard IEC 60076-1[4] - *”A power transformer is a static piece of apparatus with two or more windings which, by electromagnetic induction, transforms a system of alternating voltage and current into another system of voltage and current usually of different values and at the same frequency for the purpose of transmitting electrical power”.*

A transformer is defined as a passive device since no control action is required for its normal operation. Based on Faraday’s law of induction [5], the alternating-currents flowing through one of the transformer windings generate the alternating-electromagnetic fields resulting in electromotive-force (induced voltage) in all the others via the electromagnetic coupling. By means of an appropriate turns ratio between the windings, an arbitrary input-output voltage ratio can be achieved. However, the operation frequency on each terminal is the same - dictated by the excitation frequency on the primary winding.

Traditionally, within the alternating-current (AC) transmission and distribution systems, transformers are directly connected to the grid, thus operating at low grid frequencies. There are a couple of main standard utility grid frequencies:

- 50 and 60Hz - characteristic for the utility grids in European and other countries, e.g. USA. Usually, the entire utility grid of one country is operating on either one or the other frequency. However, there are also some exceptions where both systems are used, e.g. Japan, Saudi Arabia, and South Korea. Full lists of countries utilizing 50Hz and 60Hz can be found in [6]
- 16.7Hz - characteristic for legacy railway grids. Due to the high expenses associated with the eventual transition to a modern 50/60Hz system, the existing infrastructure dating from the early electrification period, when direct-current (DC) machines were operated as prime movers in trains at sufficiently low frequency AC to limit the commutation arcing, is still in use.

Power transformers are one of the oldest and most mature technologies in electrical engineering, having reliably served in the previously mentioned applications for more than a century. Operation voltages, frequencies, shapes and materials are standardized and the general guidelines in terms of best practices have been empirically well confirmed over the years, resulting in relatively simple, highly efficient (above 99%) and reliable transformers at relatively low cost (roughly 10kUSD/MW).

However, the weight and/or volume of the transformer can be problematic or even prohibitive for certain applications such as on-board traction or aerospace, respectively. Direct grid connection implies fixed operation at the grid frequency which can results in quite sub-optimal transformer characteristics, especially in traction applications within the legacy railway grids operating at 16.7Hz [7]. Historically, the standard frequency for the grid interconnection was limited to 50/60Hz due to the limitations of the other components in the system, e.g. the generators, motors and transmission.

Moreover, as passive devices, transformers do not facilitate the active power flow control or the necessary interfacing of the power systems operating at different frequencies since a full global conversion to either 50Hz or 60Hz is currently not an economically viable option.

1.1.3 Solid State Transformers

Similar to the paradigm shift caused by the passive transformer, the recent advancements in power electronics have enabled the efficient energy conversion and interconnection of any kind of AC or DC electric systems - the so called solid state transformer (SST), as presented in **Fig. 1.1**. As can be seen, an SST consists of at least two converter stages, and a medium/high frequency transformer (MFT). The converter stages enable active control of the input and output states, currents and voltages, thus facilitating the power flow control between any types of interfaced systems. One or more MFTs are used both for input output voltage level matching and galvanic isolation.

In contrast to line frequency transformers (LFTs) operating at fixed line frequency, MFTs operate within the converter at higher (switching) frequencies, decoupled from the rest of the system. In that respect, their operating frequency is an internal design parameter which can be used to optimize the overall converter characteristics such as volume, weight, efficiency etc.

In low-power low-voltage applications, the operation of power electronic converters at increased frequencies, enabled by fast switching of the modern semiconductor modules, resulted in a great decrease of the volume and weight of the passive components leading to a drastic increase of the

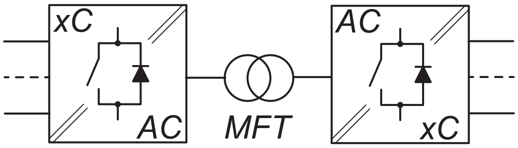

Fig. 1.1 Simplified depiction of the SST concept showing the key components, the converter stages and the MFT, where xC represents any type of AC or a DC system.

converter power density. As an illustrative example, a modern laptop charger has effectively above 50% higher power density (lower volume and weight) compared to the early brick-sized versions. This trend in low-power low-voltage applications (various appliances) has inspired the notion of applying the similar concepts in higher power and voltage applications (SSTs) - generation, traction, transmission etc.

While the foundations of the concept can be traced back to 1969 [8]–[10], only recently, the proliferation of the high-power silicon (Si) semiconductor devices and advances in magnetic materials have truly given life to the SSTs. In that respect, there has been a great increase in the SST research interest in the recent years, resulting in several prototypes, predominantly from industry. Especially now, the fast advancements in power semiconductor industry and the expected proliferation of the wide-band gap high power semiconductor devices such as silicon carbide (SiC) and gallium nitrite (GaN) are further promoting the concept.

1.2 Applications and Requirements

There are several applications where SSTs can either bring significant benefits or even serve as enabling technologies. These are the main driving forces of the research in the field, constantly pushing the requirement limits.

1.2.1 Traction

Traction applications may be the ones to see the most drastic performance improvements [11]. These applications are supplied by single-phase AC grids operating at: (i) 16.7Hz, 15kV, legacy grids and (ii) 50Hz, 25kV, more modern railway grids. The traction power supply is located on-board the locomotive implying serious weight and volume constraints. In that respect, SSTs have an inherent key advantage, especially compared to the bulky 16.7Hz on-board transformers.

The reduction of the volume and weight, enabled by the SST technology, implies cost savings and efficiency improvements on the system level for such applications. Therefore, the railway was a natural early adopter of the concept. Several successful pilot projects were conducted by the major industry players in Europe such as ABB [12]–[15], Alstom [16], [17] etc. One of the most prominent examples of a successfully deployed traction SST is the ABB's power electronic traction transformer (PETT), as shown in **Fig. 1.2**, which was commissioned on a shunting locomotive and successfully passed its one-year field trial [14], [15].

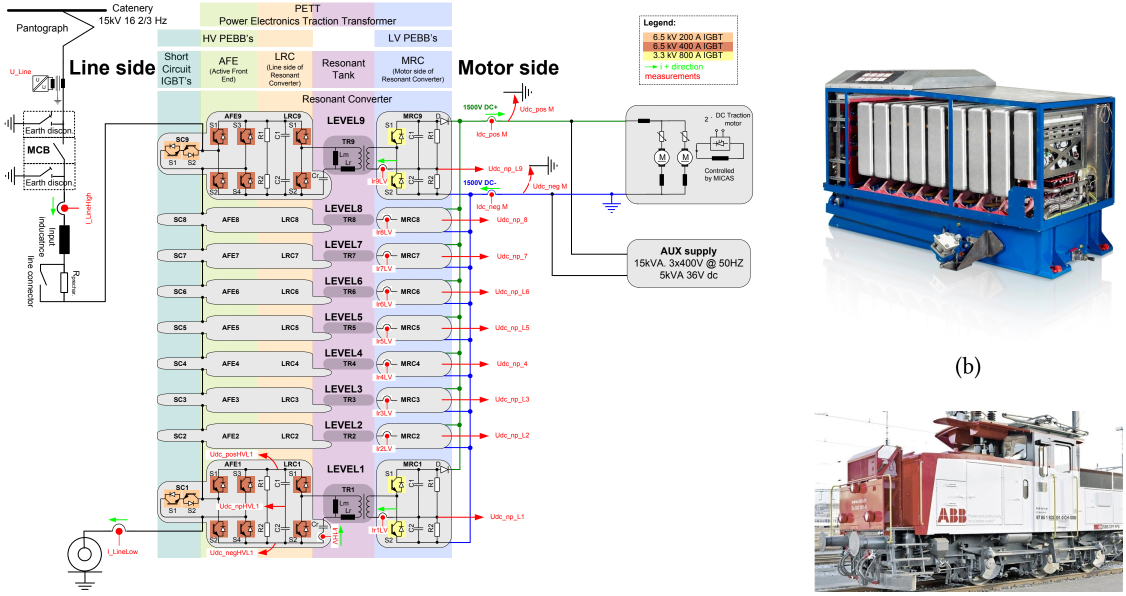

(a)

(b)

(c)

Fig. 1.2 ABB PETT [14], [15]: (a) electrical scheme showing the 9 identical input-series ouput-paralel connected converter cells, each consisting of two converter stages and an MFT; (b) The final converter assembly; (c) The commissioned shunting locomotive where 1.2MW PETT has replaced the original 16, 7Hz single phase transformer and semi-controlled thyristor rectifier rated at 450kW, achieving threefold power increase within the same volume.

1.2.2 Utility Grids

Unlike the traction applications, single-phase grids often operating at very low 16.7Hz frequencies, medium voltages, 15 – 25kV and powers of up to several MW, utility grids are 3-phase and operate at 50 – 60Hz with much higher powers in MW – GW ranges and with a much wider spectrum of standard voltage levels, e.g. 3.3, 4.16, 6, 11, 15, 20kV etc.

Taking into account the high-powers and utilization, efficiency plays the most important role in these applications. On the other hand, the interconnection/conversion is implemented in substations where volume and weight are usually not so critical.

Moreover, already at 50−60Hz passive transformers are much more compact compared to their traction counterparts operating at 16.7Hz. Finally, taking into account the excellent efficiency of passive utility transformers (above 99%), the SST concept, with efficiency up to 98%, is not a competitive solution in terms of these raw gains.

What SSTs do offer to utilities is controlability. They can serve as actuators to facilitate the control of power flows, interfacing of grids operating at different frequencies or battery power storage etc. In other words, although they are inferior to passive utility transformers in terms of efficiency, cost and reliability, they represent the essential enabling technology for many envisioned functionalities of the modern/future power systems - smart grid concept.

One of the most prominent pilot projects in this area is first ever 1MVA SiC based solid state power substation interfacing 13.8kV and $465/\sqrt{3}$V, 60Hz utility grids, as shown in [18]. Impressive volume

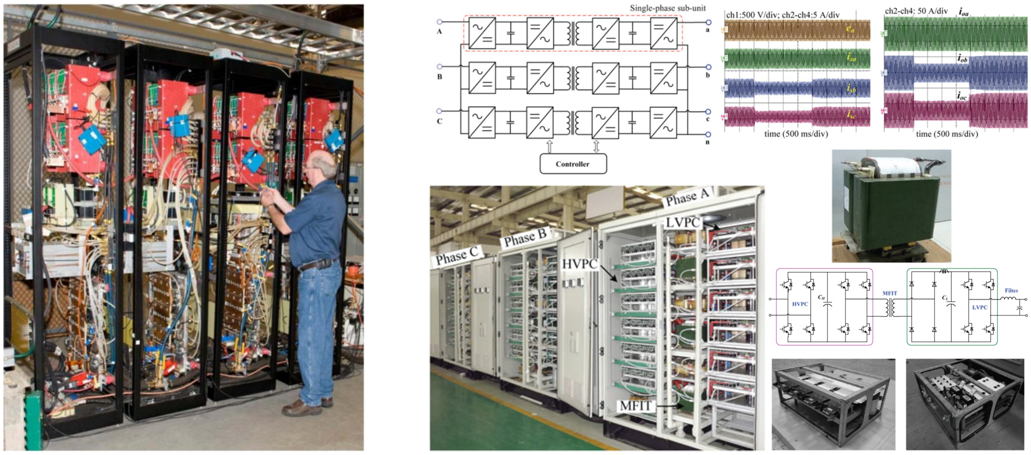

(a) (b)

Fig. 1.3 (a) A 13.8kV to 465/$\sqrt{3}$V,60Hz, 1MVA SiC enabled solid state power substation [18]. (b) HUST, Wuhan - a 10kV to 400V, 50Hz, 0.5MVA electric power transformer (EPT) [19].

and weight reduction compared to the passive 60Hz LFT was reported, 50% and 75%, respectivelly, while the achieved efficiency was 97%.

Another more recent example that has been implemented in the field is the (HUST, Wuhan) 10kV to 400V, 50Hz, 0.5MVA electric power transformer (EPT) [19], as displayed in **Fig. 1.3(b)**. It features 3.3kV and 1.2kV IGBTs on the on the HV and LV side, respectively, operating at 1kHz switching frequency and 30kW MFT units.

1.2.3 MVDC Grids

Nowadays, with an increased proliferation of the distributed renewable power sources, such as wind and solar, that are interfaced to the medium-voltage alternating-current (MVAC) distribution grids, the idea of medium-voltage direct-current (MVDC) distribution has been gaining more and more popularity. The efficiency and power throughput of the lines would naturally increase and power transfer would be possible to longer distances without any stability issues, characteristic for the AC systems. These concepts have already been deployed with great success at the high voltage transmission level - high-voltage direct-current (HVDC) systems allowing for a very strong interconnection over very large distances.

SSTs are the natural converters that would enable the MVDC distribution, allowing the interfacing of any type of utility, distributed renewable sources, energy storage and residential and industrial consumers, as shown in **Fig. 1.4(a)**. Moreover, a MVDC distribution grid fully equipped with SSTs would feature full controlability of all the states, facilitating the implementation of all the smart-grid concept functionalities, e.g. virtual plant, etc.

However, the benefits of the DC transmission increase with the line lengths and powers. Therefore, the economic viability of MVDC distribution grids is still debatable. Moreover, the compliance with typically very conservative requirements of the distribution system operator (DSO) is usually prohibitive.

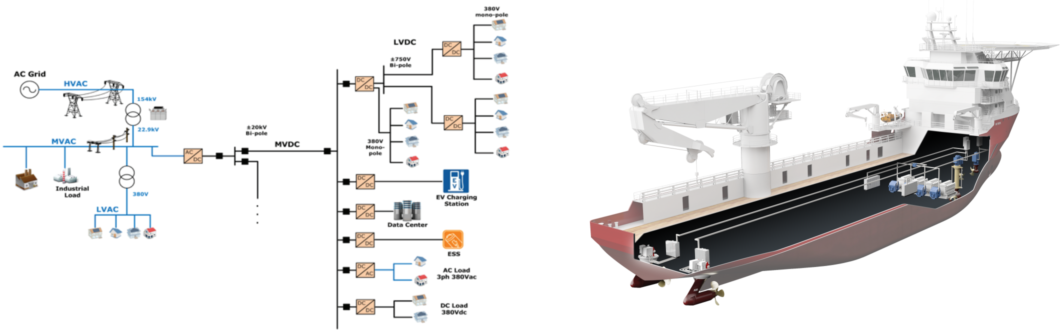

(a)

(b)

Fig. 1.4 (a) Example of a MVDC distribution grid [25]. (b) Example of a MVDC ship distribution [26].

While the situation is complicated for MVDC distribution on shore, there are not so many restrictions (no DSO regulations) when it comes to various industrial and in particular marine applications. These are therefore the natural early adopters of the concept. There are several system level benefits of the MVDC distribution: improved partial load efficiency, no frequency synchronization of the generators, integration of storage technologies, etc. While LVDC system are already commercialized, the MVDC is still a research topic. Spearheaded by the major industry players, there has been a lot of research effort recently in the field [20]–[22] analyzing full or partial (power link between the generators and prime movers) MVDC distribution and the still unsolved problems of direct MVDC protection [23], [24], as displayed in **Fig. 1.4(b)**.

1.3 Challenges

There are many challenges preventing the SSTs to make the step from a several pilot projects to real market penetration. While most of these are business related, e.g. higher cost of converters etc., the concerns about the complexity and the associated reliability of these systems are another strong impediment. In order to accept all of this, the improvement of the main figures of merit needs to be strong enough.

As can be seen from the various application requirements, the main SST trade-off is the one between efficiency and power density. With the recent advancements in power semiconductor industry and the expected proliferation of the wide-band gap high power semiconductor devices such as SiC and GaN, the high frequency operation, which resulted in drastic decrease of the converter weight and volume in low-voltage low-power applications, is now possible for high-power MV SST applications. This however sets an entirely new reference for the MFTs, as the key enabling components of the SSTs, having a detrimental influence on the total converter efficiency and power density.

Unfortunately, the developments of the magnetic components have not been following the pace of the power semiconductor industry. Many challenges related to high frequency operation, MV insulation and high power processing capabilities remain not fully addressed. Finally, it is a question if and how this frequency scaling can be translated to high power MV applications.

1.3.1 Objectives of the Thesis

In view of the above discussion, this thesis focuses on the technical challenges tied to modeling and design optimization of the MFTs with regard to different requirements and present commercial technologies. The following points are analyzed in particular:

- Identification of the design space - available technologies, design choices and materials suitable for MFTs
- Summary of the available modeling, suitable for design optimization. Improvements of the accuracy and validity range of the existing and derivation of new models for the most critical phenomena.
- Synthesis of an MFT design optimization methodology, based on the derived models and design space.
- Verification of the design optimization methodology on a realized 100kW, 10kHz MFT prototype with an integrated resonant tank for the series resonant converter (SRC) operation.
- Investigation of the potential of different design variations for the improvement of MFT efficiency and power density on the SST level.

1.3.2 Contributions of the Thesis

The main contributions of the thesis are:

- A knowledge basis that increases the confidence in the technology and narrows down the gap between the often too optimistic expectations and reality.
- The proposed corrections/modifications of the existing analytical models, providing improved accuracy and extended validity range with minimal or no added complexity.
- The proposed statistical data driven models (SDDM), that allow to capture the complex effects, with otherwise prohibitively high computational cost for design optimization, in rather simple and fast executing multi-variable polynomial models.
- The results of the thorough testing of the electrical, dielectric and thermal behavior that serve as a proper benchmark for verification and improvement of the accuracy of the utilized models.
- Conclusions of the MFT design sensitivity analysis, exposing the limitations for the expected frequency scaling of the MFTs, with regard to the available design space and the implications on the converter level.

1.4 Outline of the Thesis

The thesis is organized in three parts and contains nine chapters.

The first part contains a critical analysis of the MFT design space considering the SST applications, identifying and classifying the available technologies and materials, suitable for operation within the voltage, power and frequency range of interest:

> **Chapter 2** discusses the basic motivation and technical challenges tied to transformer operation at medium frequency within power electronic applications. Moreover, an analysis of the state-of-the art is provided in respect to required specifications and selected technologies and materials.
>
> **Chapter 3** provides a high level description of the MFT prototyping and design optimization. Desired MFT features and relevant technologies and materials are identified and classified, forming the design space for the design optimisation.

The second part presents the relevant modeling of the underlying MFT physics, design optimization and experimental verification on a realized 100kW, 10kHz MFT prototype:

> **Chapter 4** provides a review of the available analytical modeling techniques and the necessary developments for the application on the MFT structure. Several modifications are proposed improving the accuracy and application range of the critical models, allowing to properly address the high-power MV medium-frequency applications.
>
> **Chapter 5** proposes a new class of neural-network inspired data-driven models, especially derived for design optimization purposes. These models allow for an efficient (3 – 5 orders of magnitude faster compared to the finite element method (FEM)), yet sufficiently accurate (within 5 – 10% error relative to FEM), estimation of the complex effects with otherwise impractically high computational cost and/or convergence issues.
>
> **Chapter 6** presents the synthesis of all the models into a brute-force based design optimization algorithm. Detailed description of the proposed design optimization procedure is provided on an example of the 100kW, 10kHz MFT designed for the operation within the SRC, featuring integrated resonant tank.
>
> **Chapter 7** describes in detail the realized 100kW, 10kHz MFT prototype and the experimental verification of its electric, dielectric and thermal properties.

The third part provides a detailed analysis of the potential for MFT scaling on the SST level, considering both the readily available Si power semiconductor devices and the emerging SiC with extended blocking voltages and operation frequency range:

> **Chapter 8** analyzes the impact of the selected power semiconductor modules and the resulting converter modularity and operation frequency on the MFT scaling. The case study is performed on a typical 0.5MW 10kV input series output parallel SRC based converter topology example.
>
> **Chapter 9** provides the summary of the main findings and contributions of this thesis and outlines the future work to be carried out.

1.5 List of publications

The publications resulting directly from the *PhD Thesis* are:

Journal papers:

J1. M. Mogorovic and D. Dujic, “Sensitivity Analysis of Medium-Frequency Transformer Designs for Solid-State Transformers,” *IEEE Transactions on Power Electronics*, vol. 34, no. 9, pp. 8356–8367, Sep. 2019

J2. M. Mogorovic and D. Dujic, “100 kW, 10 kHz Medium-Frequency Transformer Design Optimization and Experimental Verification,” *IEEE Transactions on Power Electronics*, vol. 34, no. 2, pp. 1696–1708, Feb. 2019

Conference papers:

C1. M. Mogorovic and D. Dujic, “Computationally Efficient Estimation of the Electric-Field Maximums for the MFT Insulation Coordination,” in *2019 IEEE Energy Conversion Congress and Exposition (ECCE)*, Oct. 2019, accepted

C2. M. Mogorovic and D. Dujic, “Modeling And Experimental Verification of Geometry Effects on Core Losses,” in *10th International Conference on Power Electronics – ECCE Asia (ICPE 2019-ECCE Asia)*, May 2019, pp. 1–7

C3. M. Mogorovic and D. Dujic, “Computationally Efficient Leakage Inductance Estimation of Multi-Winding Medium Frequency Transformers,” in *PCIM Europe 2019; International Exhibition and Conference for Power Electronics, Intelligent Motion, Renewable Energy and Energy Management*, May 2019, pp. 1–6

C4. M. Mogorovic and D. Dujic, “Sensitivity Analysis of Medium Frequency Transformer Design,” in *2018 International Power Electronics Conference (IPEC-Niigata 2018 -ECCE Asia)*, May 2018, pp. 2170–2175

C5. M. Mogorovic and D. Dujic, “Medium frequency transformer leakage inductance modeling and experimental verification,” in *2017 IEEE Energy Conversion Congress and Exposition (ECCE)*, Oct. 2017, pp. 419–424

C6. M. Mogorovic and D. Dujic, “Thermal modeling and experimental verification of an air cooled medium frequency transformer,” in *2017 19th European Conference on Power Electronics and Applications (EPE’17 ECCE Europe)*, Sep. 2017, P.1–P.9

C7. M. Mogorovic and D. Dujic, “Medium Frequency Transformer Design and Optimization,” in *PCIM Europe 2017; International Exhibition and Conference for Power Electronics, Intelligent Motion, Renewable Energy and Energy Management*, May 2017, pp. 423–430

Technical tutorials:

T1. M. Mogorovic and D. Dujic, “High-Power Medium-Frequency Transformer Design Optimization,” pp. 1–120

Given at:

- 10th International Conference on Power Electronics – ECCE Asia (ICPE 2019-ECCE Asia), in Busan, South Korea, 2019
- 19th IEEE International Conference on Industrial Technology ICIT 2018, Lyon, France, 2018
- 19th International Symposium on Power Electronics Ee 2017, Novi Sad, Serbia, October, 2017
- IEEE Energy Conversion Congress and Exposition ECCE 2017, Cincinnatti, OH, USA, 2017
- 19th European Conference on Power Electronics and Applications (EPE'17 ECCE Europe) in Warsaw, Poland, 2017

Workshops and seminars:

W1. M. Mogorovic and D. Dujic, "Design Optimization of MFT for High-Power MV Applications," in *ECPE Workshop: New Technologies for Medium-Frequency Solid-State Transformers*, Feb. 2019, pp. 1–56

W2. M. Mogorovic and D. Dujic, "Medium Frequency Transformer Design Optimization Tradeoffs," in *Future Swiss Electrical Infrastructure (SCCR-FURIES) Technical Workshop 2018*, Sep. 2018, pp. 1–34

W3. M. Mogorovic and D. Dujic, "MFT Modeling and Design Optimization," in *2016 Future Swiss Electrical Infrastructure (SCCR-FURIES) anual conferance*, Oct. 2016, pp. 1–120

2

Background and State of the Art

This chapter provides the necessary transformer basics and a qualitative analysis of the transformer scaling laws. Moreover, an overview of the specific challenges, related to operation at elevated frequencies, is provided. Based on these notions, the state of the art is discussed in detail.

2.1 Transformer basics

The most basic transformer consists of two windings magnetically coupled through a ferromagnetic core, such as depicted in **Fig. 2.1**. Note that this type of winding arrangement is used only for the purposes of the analysis. A transformer can be described by the next system of equations

$$V_1 = R_{\sigma 1} I_1 + \frac{d\psi_1}{dt} \tag{2.1}$$

$$V_2 = R_{\sigma 2} I_2 + \frac{d\psi_2}{dt}. \tag{2.2}$$

where V_1 (V_2), $R_{\sigma 1}$ ($R_{\sigma 2}$) and ψ_1 (ψ_2) are the primary (secondary) winding voltage, resistance and total flux. As can be seen in **Fig. 2.1**, the primary and secondary winding total flux both consist of their own leakage flux and the mutual flux. This translates into the next equations

$$\psi_1 = N_1 \phi_{\sigma 1} + N_1 \phi_m = L_{\sigma 1} I_1 + N_1 \phi_m \tag{2.3}$$

$$\psi_2 = N_2 \phi_{\sigma 2} + N_2 \phi_m = L_{\sigma 2} I_2 + N_2 \phi_m \tag{2.4}$$

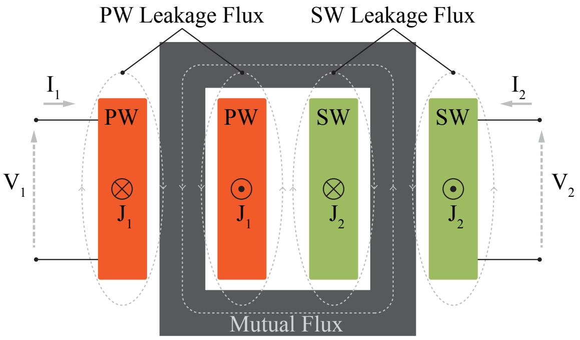

Fig. 2.1 Simplified depiction of the transformer for the derivation of the equivalent circuit. Note that the transformer construction with primary and secondary windings on separate core limbs is used in special applications where high leakage inductance is needed. This however is useful for more obvious derivation of the equivalent circuit [29].

where ϕ_m is the mutual flux, $\phi_{\sigma 1}$ ($\phi_{\sigma 2}$), N_1 (N_2) and $L_{\sigma 1}$ ($L_{\sigma 2}$) are the leakage flux, the number of turns and the leakage inductance of the primary (secondary) winding.

While the mutual flux is almost fully confined within the core, the leakage flux path is partially or fully going through the air. Due to the high magnetic permeability of the core material, the mutual flux is several orders of magnitudes higher compared to the leakage. Note that the shape of the real leakage flux paths does not look exactly as depicted **Fig. 2.1**, which is only an illustration.

Substitution of (2.4) in (2.2) leads to

$$V_1 = R_{\sigma 1} I_1 + L_{\sigma 1}\frac{dI_1}{dt} + N_1\frac{d\phi_m}{dt} \tag{2.5}$$

$$V_2 = R_{\sigma 2} I_2 + L_{\sigma 2}\frac{dI_2}{dt} + N_2\frac{d\phi_m}{dt} \tag{2.6}$$

The magnetization flux can be eliminated by multiplying the second equation by N_1/N_2 and subtracting it from the first,

$$V_1 - R_{\sigma 1} I_1 - L_{\sigma 1}\frac{dI_1}{dt} = V_2' - R_{\sigma 2}' I_2' - L_{\sigma 2}'\frac{dI_2'}{dt} \tag{2.7}$$

where

$$V_2' = \frac{N_1}{N_2}V_2, \quad I_2' = \frac{N_2}{N_1}I_2, \quad R_{\sigma 2}' = \left(\frac{N_1}{N_2}\right)^2 R_{\sigma 2} \quad \text{and} \quad L_{\sigma 2}' = \left(\frac{N_1}{N_2}\right)^2 L_{\sigma 2} \tag{2.8}$$

are the secondary winding electrical parameters referred to the primary side.

Moreover, if we observe the open secondary circuit operation and take into account the losses in the core material ($\mu = \mu_{Re} + j\mu_{Im}$), some amount of additional active and reactive current exists in the primary winding due to the core losses and magnetization, respectively. In other words, the transformer acts as an inductance with losses.

$$I_1 + I_2' = I_m \tag{2.9}$$

Based on this conclusion and (2.7) and (2.9), a lumped element equivalent circuit of a transformer can be derived, as given in **Fig. 2.2**. An ideal transformer can be added at the secondary terminals if the conversion of the electric parameters to the real secondary side reference is needed. Equivalently, all of the parameters can be referred to the secondary winding terminals if this simplifies other developments.

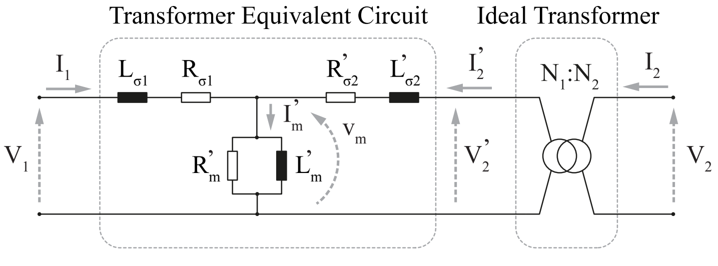

Fig. 2.2 A detailed lumped element equivalent electric circuit of a transformer, suitable for modeling of most effects on the converter level.

This lumped circuit representation allows to model most of the relevant effects on the converter level and will be used throughout this thesis for this purpose. Proper modeling of the parameters of this equivalent circuit on the other hand, is a more complex task that requires a deep analysis of the transformer geometry and other physical characteristics. This is addressed in detail in **Chaps. 4** and **5**.

2.2 MFT Scaling Laws: A Qualitative Analysis

As already mentioned, the converter operation at elevated frequencies has led to a great increase in power density in low-voltage low-power applications. The underlying frequency scaling mechanism, in its simplest form, can be shown through the core area product expression [30]

$$A_p = A_{Fe}A_{cwa} \approx \frac{P_n}{K_f K_u B_m J_m f_{sw}} \tag{2.10}$$

where A_{Fe} is the core cross-section, A_{cwa} is the core window area, P_n is the processing power, K_f is the waveform coefficient, K_u is the core window utilization coefficient, B_m is the peak flux density, J_m is the current density and f_{sw} the switching frequency.

As can be seen the area product represents an artificial link between the estimated power processing capability of the core and its size, which also provides a good figure of the total transformer size. Among the parameters in this expression K_f is defined by the converter waveform, K_u is limited by the transformer construction and B_m and J_m by the material properties and thermal constraints, whereas the switching frequency seems to be limited only by the semiconductor capabilities. According to this expression the transformer size decreases inverse proportionally to the increase of the switching frequency, which shows great potential for the increase of the power density. This has many positive implications: easier integration, less material utilization, lower investment cost and environmental footprint etc.

However, the approximate relation (2.10) provides only a very simplified estimation of the transformer size, in function of the electric requirements and selected design alternatives, that is suitable for fast design. It does not show the effects on the MFT internal characteristics such as temperature gradients and the relative cost. A more comprehensive step-by-step qualitative analysis of the scaling laws of each variable characterizing the MFT in mechanical and electric sense, under the assumption of the same transformer construction and equal material utilization in terms of current and flux densities, is described in **Tab. 2.1**.

Starting from the basic relations such as the calculation of the arbitrary MFT surfaces, volume and weight, it is possible to derive the scaling laws for more complex characteristics which are not so intuitively obvious, such as the temperature rise, relative losses and the relative cost. As can be seen, the relative cost is reverse proportional to both size and frequency. Therefore, from the material quantity and cost point of view, high power MFTs appear even more attractive than their smaller counterparts.

However, it can be seen that the temperature rise is proportional to the linear spatial dimension and the sum of the additional winding ($F(f_{sw})$) and core (f_{sw}^a) loss correction factors associated to high frequency effects. Consequently, the temperature gradients increase with the increase of the

Tab. 2.1 MFT scaling laws for constant material utilisation - magnetic flux and current density

Variable	Formula	Proportion	Simplified Shell MFT Structure
Cooling Surface	$S_c = C_1 l^2$	k^2	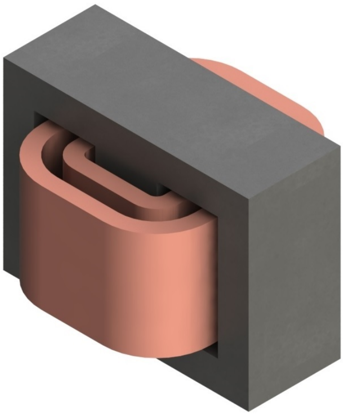
Volume and Mass	$M = \gamma V = C_2 l^3$	k^3	
Current	$I = J S_{Cu}$	k^2	
Induced Voltage	$U = C_3 f_{sw} B_m S_{Fe}$	$f_{sw} k^2$	
Apparent Power	$P = UI$	$f_{sw} k^4$	
DC Resistance	$R_{DC} = N\rho l / S_{Cu}$	$1/k$	
Copper Losses	$P_{Cu} = F(f_{sw}) R_{DC} I^2$	$F(f_{sw}) k^3$	
Core Losses	$P_{Fe} = K f_{sw}^a B_m^b V$	$f_{sw}^a k^3$	
Temperature Rise	$\Delta\theta = (P_{Cu} + P_{Fe})/(\alpha S_c)$	$k(F(f_{sw}) + f_{sw}^a)$	
Relative Losses	$P_r = (P_{Cu} + P_{Fe})/P$	$(F(f_{sw}) + f_{sw}^a)/(k f_{sw})$	
Relative Cost	$\epsilon = M/P$	$1/(k f_{sw})$	

Where: l, k - spatial dimensions, C_i - proportionality constants, γ - MFT average density, $F(f_{sw})$ - skin and proximity effect correction factor

transformer size (processing power), as well as the frequency. Depending on the type of insulation, additional insulation reinforcement may as well substantially increase the thermal resistances towards the ambient (e.g. solid type insulation). Therefore, the frequency, power processing and voltage domain where the described scaling can be preserved without additional cooling effort is limited.

On the other hand, relative losses decrease reversely proportional to the size increase, indicating that the higher power rated transformers should yield a better efficiency. The frequency dependency is a function of the winding ($F(f_{sw})$) and core (f_{sw}^a) loss frequency correction factors. The frequency exponent of the core materials, $a > 1$, and therefore the relative core losses increase with the frequency increase in the amount depending on the material properties. Skin and proximity correction factor ($F(f_{sw})$) is negligible for low frequencies (Δ[1] < 1), but increases exponentially at higher frequencies ($\Delta > 1$) [31]. Therefore, the relative winding losses have a minimum at some frequency where penetration ratio is around one. Consequently, depending on the core material properties, and loss distribution between the core and the windings, the total relative losses are a convex function of frequency either having a minimum point (around $\Delta \approx 1$) or an increasing trend in the entire frequency range, depending on the initial gradient.

As can be seen, while the potential for the cost savings, increase of power density and efficiency are raising great expectations, there are many coupled effects that influence the scaling of the MFT.

---

[1] Δ is the penetration ratio, as will be defined in **Sec. 4.3**

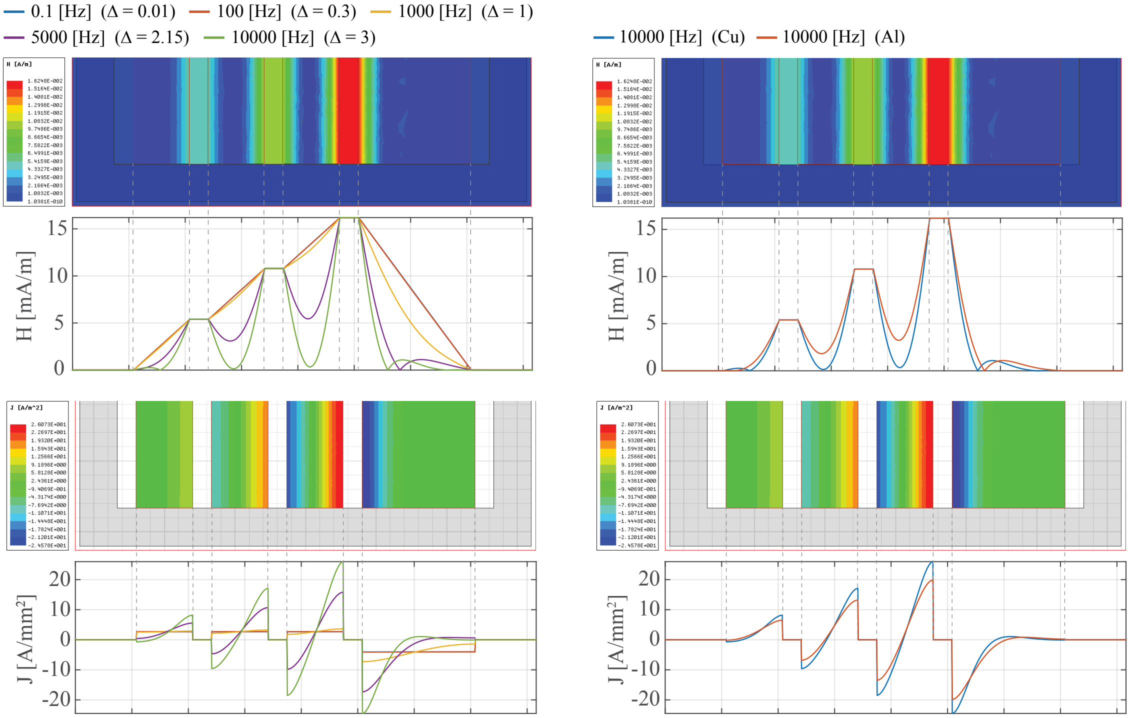

(a) (b)

Fig. 2.3 H (top) and J (bottom) field distributions within the core window area of an ideal[2] foil winding transformer: (a) for copper windings at several different frequencies covering the Δ range from 0.01 to 3; (b) for copper and aluminum windings at a same frequency.

2.3 Challenges

This section provides an overview of the main challenges that restrict the MFT frequency scaling. A brief discussion is provided through a couple of illustrative examples that highlight the underlying mechanisms. A detailed description and modeling of these phenomena will be provided later on in **Chaps. 4** and **5**.

2.3.1 Skin and proximity effect

In order to illustrate the skin and proximity effects, a winding structure composed of foil winding layers, as shown in **Fig. 2.3(a)**, is considered. As can be seen, these effects become stronger with the increase of the operating frequency. This implies a non-uniform current density within the winding conductors and an under-utilization of the conductor material which manifests as an increase of the AC resistance compared to the DC value. Moreover, it can be seen that in case of high frequencies (relative to the foil conductor width - Δ > 1), the current density in some of the foil winding layers may even become negative in certain regions due to the strong proximity effect. These conductor regions, in this case, do not only not contribute to the conduction of the primary current, but generate pure losses.

This shows that the skin and proximity effects must not be neglected at higher frequencies, as a simple increase of the conductor cross-section (increase of the foil width) does not necessarily decrease the conduction losses as in case of DC, but can even result in the opposite effect. Therefore, depending on the operating frequency, appropriately thin foil conductors, with appropriately low Δ have to be used to limit the skin and proximity effects. In order to get the high enough cross section (low enough DC resistance), several of these thin foil conductors can be stacked together and paralleled instead.

This however again decreases the utilization of the area decimated for the winding conductors, as certain space is necessary for the insulation between the paralleled sheets of these composite winding structures. Moreover, the thickness of the insulation enamel does not decrease proportionally to the conductor thickness, resulting in lower conductor volume utilization factors for composite windings consisting of more thinner foils or finer stranded Litz wires [32].

While the increase of the frequency allows the increase of the transformer processing power without increasing the maximum current or flux density, as shown in **Tab. 2.1**, the additional insulation within the composite winding structures, necessary for mitigation of the additional frequency dependent losses, results in increased conductor volume. The same is true for the transformer cores made out of conductive ferromagnetic materials, where thin lamination is necessary to limit the eddy current losses within the lamination sheets.

Besides the resulting conduction losses (AC resistance), the skin and proximity effects have an impact on the transformer leakage inductance as well. As can be seen in **Fig. 2.3(a)**, the induced eddy currents suppress the magnetic field from the inner conductor volume. The total leakage magnetic field energy and the resulting leakage inductance of the MFT therefore decreases with the increase of frequency.

Finally, as can be seen in **Fig. 2.3(b)**, the conductor material has an impact on the skin and proximity effect. Due to the lower conductivity of aluminum, the induced eddy currents have a lower magnitude compared to the ones in copper. Nevertheless, this also implies a higher base DC resistance for the same conductor cross-section.

2.3.2 Edge Effect

Using thin foil sheets limits only the skin and proximity effects related to the magnetic field component parallel to the foil surface. Unlike the ideal foil winding transformer, where foil sheets spread throughout the whole core window height, realistic windings would have some dielectric spacing separating them from the core that facilitate the necessary insulation, especially in case of MV or HV applications, as displayed in **Fig. 2.4**.

As can be seen, in the case of the realistic winding arrangement, the component of the magnetic field perpendicular to the foil surface is nonzero in regions close to the foil edges. Moreover, this is also true for the portions of the windings outside of the core window area. Even though the magnitude of this component of the magnetic field is relatively small compared to the parallel component, it can have a significant impact on the losses since the foil width, seen from the perpendicular direction is the foil height which is several orders of magnitude larger - thus even with the relatively low field magnitude, eddy currents can be significant since they can flow freely, closing large loops.

---

[2] The foil winding extends over the full height of the core window.

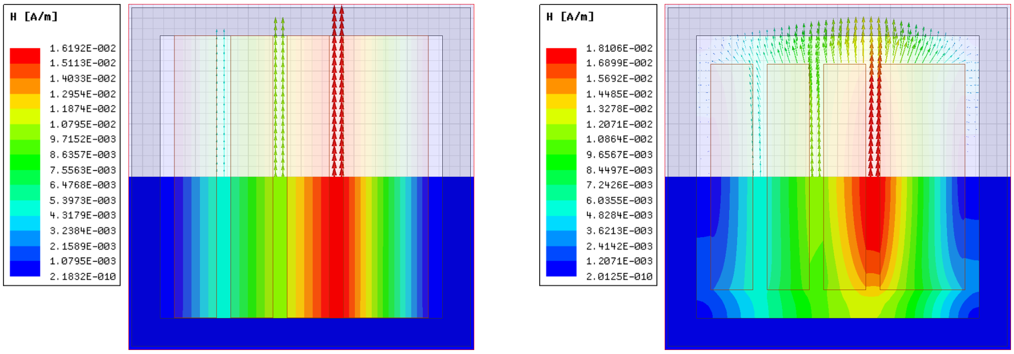

(a) (b)

Fig. 2.4 The H field vector (top) and magnitude (bottom) distribution within the core window area in case of (a) ideal foil windins and (b) realistic foil windings where some dielectric distance must exist to facilitate the required insulation level, especially in case of medium voltage applications.

Note that for a different type of composite winding such as Litz wire for example, where equivalent conductor width seen from all directions is the same, the loss contribution of this perpendicular component of the field can usually be neglected.

2.3.3 Thermal Coordination

In steady state operation, the heat generated by the transformer losses and the heat exchanged with the environment must be in equilibrium. The heat exchange with the environment happens over the MFT boundary surfaces via convection and radiation heat transfer mechanisms, as illustrated in **Fig. 2.5**. In that respect, the frequency scaling of the MFT, i.e. decrease of its size, implies a decrease of its boundary cooling surfaces, resulting in higher thermal resistances towards the ambient, as given in **Fig. 2.5(c)**. Unless the cooling effort is enhanced or losses decreased in some way, this leads to higher hot-spot temperature gradients which may be prohibitive, depending on the maximum allowed material temperatures.

Moreover, depending on the utilized core and winding type the conduction thermal resistance between the hot-spots and the cooling surfaces of the MFT can vary. The implemented (outer) winding insulation, as shown in **Fig. 2.6(a)**, has a strong impact on the equivalent thermal impedance of the winding hot-spots towards the ambient - from oil with very good convection cooling properties to solid epoxy cast with relatively low thermal conductivity.

In addition to this, as earlier mentioned, the composite windings and cores have anisotropic structures that can significantly influence the MFT behavior. The same is true when it comes to the thermal properties. While the thermal conductivity along the core laminations or copper foils and Litz wire strands is relatively high - governed by the thermal conductivity of these materials; the thermal conductivity in the normal or radial direction is significantly lower - governed by the equivalent thermal conductivity of the alternating layers of the core or winding material and their internal insulation characterized by very low conductivity, as displayed in **Figs. 2.6(b)** and **2.6(c)**.

This is why special attention should be paid to the thermal coordination - taking into account all of these effects as precisely as possible and aligning them in such a fashion that minimizes the overall

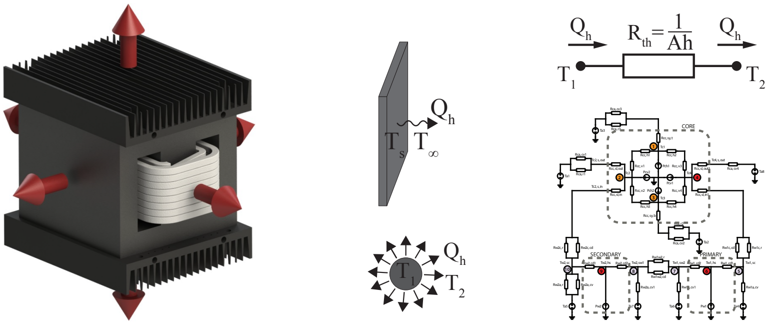

(a) (b) (c)

Fig. 2.5 Sketch of the heat exchange principle between the MFT and the environment: (a) A generic shell type MFT example, with denoted outer cooling surfaces; (b) The convective (top) and radiation (bottom) heat transfer mechanisms that occur at the outer surfaces (and free inner surfaces in case of convection) of the transformer; (c) Equivalent thermal resistance of the transformer hot-spots towards the ambient - reverse proportional to the equivalent transformer cooling surface.

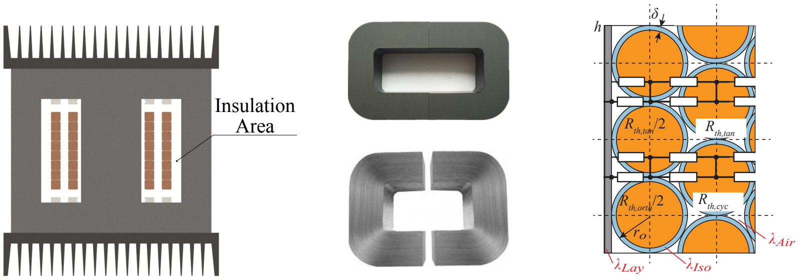

(a) (b) (c)

Fig. 2.6 (a) An MFT cross-section. (b) An example of an isotropic (ferrite) and anisotropic wound-tape (nanocrystalline) core with two different equivalent heat conductivities, in directions parallel and normal to the tape. (c) Cross-section detail of a round magnet (enameled) wire winding [33] showing the thermal resistance in the directions radial to the wires.

thermal impedance between the hot-spots and the ambient.

2.3.4 Accurate Electric Parameter Design

In contrast to LFTs, normally directly connected to the grid, MFTs operate within the power electronics converter. The two typical galvanicaly isolated DC-DC converter topologies used as SST building blocks are presented in **Fig. 2.7**. A correct design of the MFT electric parameters is essential for the proper operation of any of these converters.

In case of a dual active bridge (DAB), as given in **Fig. 2.7(a)**, the series inductance, the transformer leakage inductance, has to be designed to be above a certain value to ascertain that the converter power flow control is not overly sensitive to the slight changes of the reference phase shift of the pulses

$$L_{\sigma.min} = \frac{V_{DC1} V_{DC2} \varphi_{min} (\pi - \varphi_{min})}{2 P_n \pi^2 f_{sw} n} \tag{2.11}$$

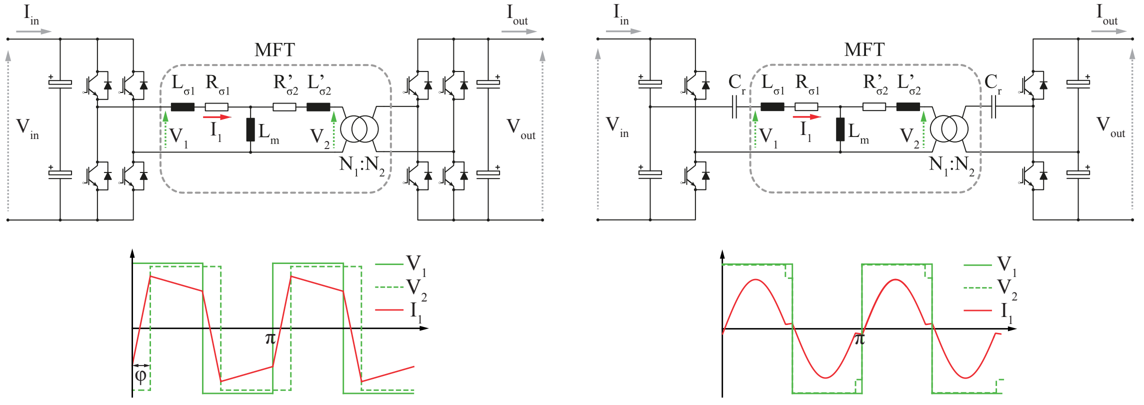

(a)

(b)

Fig. 2.7 Typical galvanicaly isolated DC-DC converter topologies used as SST building blocks: (a) A dual active bridge converter and its voltage and current waveforms in case of a typical operation, (b) A series resonant converter with distributed capacitor bank and integrated resonant tank within the MFT and its voltage and current waveforms in case of the typical sub-resonant operation that ensures soft switching.

where V_{DC1} and V_{DC2} are the primary and secondary side DC bus voltages, P_n is the nominal power, f_{sw} is the switching frequency, n is the transformer ratio and φ_{min} is the minimum upper bound of the φ range that maps into the full power range. φ_{min} is usually selected as high as possible to ensure that the power flow control is as robust as possible to the phase shift reference signal (φ_{ref}) imperfections, yet well below $\pi/2$ which is the stability limit.

The magnetization inductance L_m on the other hand is typically designed to be as high as possible. Depending on the converter specifications, the reference series inductance of a DAB can be quite high. Note that additional (external) inductors can be added in cases where the required series inductance is impractically high to be integrated within the MFT by means of design adjustment.

Precise leakage inductance design is even more essential in case of the SRC, where the MFT is a part of the resonant circuit, thus having a direct impact on the resonant frequency, as shown in **Fig. 2.7(b)**.

$$L_{\sigma.ref} = \frac{1}{\omega_0^2 C_r} \tag{2.12}$$

Depending on the nominal voltage and current levels, SRCs for high power applications usually require a very low leakage inductance. In that respect a low relative design error is even harder to match. In that respect, the utilized models and mechanical assembly have to be very precise.

Moreover, the magnetizing inductance is normally high, i.e. designed to limit the magnetization current magnitude to the reference $I_{m.ref}$.

$$L_m = \frac{nV_{DC2}}{4f_s I_{m.ref}} \tag{2.13}$$

In this way, the switch-off current and the associated switching losses can be controlled. However, depending on the minimum feasible dead time and resonant current magnitude, $I_{m.ref}$ needs to be sufficiently high to maintain the zero voltage switching (ZVS).

As can be seen, a proper design of the MFT electric parameters is one of the key design tasks on the converter level.

2.3.5 Non-Sinusoidal Excitation

As aforementioned, unlike the traditional LFTs operating at low grid-frequencies with sinusoidal excitation, MFTs operate within the power electronic converters with square voltage and in general non-sinusoidal current waveforms at elevated frequencies, typical for the given converter topologies. This has an impact on the transformer losses and insulation coordination.

Traditionally, the losses of the different core materials are characterized from the manufacturer side using sinusoidal excitation, as illustrated in **Fig. 2.8(a)**. Some methodology is therefore necessary for generalization of these results to different types of square voltage excitation that the core experiences within a converter. Alternatively, custom characterization can be performed, but this requires already having the representative samples and is more complex and expensive - usually performed in later iterations of the design process.

As can be seen in **Fig. 2.7**, the MFT current is in general non-sinusoidal - piece-wise linear and pseudo-sinusoidal in case of the DAB and SRC, respectivelly. This has an impact on the winding losses. While in the case of a SRC, the current can be considered to be practically sinusoidal, in case of a DAB, it may contain a significant amount of higher order harmonics, as illustrated in **Fig. 2.8(b)**. As already discussed in **Sec. 2.3.1**, the conduction losses are frequency dependent. In that respect, taking into account the linearity of the material, the total conduction losses can be obtained in a harmonic manner - as a sum of all the individual harmonic conduction losses.

As can be seen, the specific non-sinusoidal waveforms of the given converter have to be taken into account at the design stage in order to ensure a proper MFT behavior.

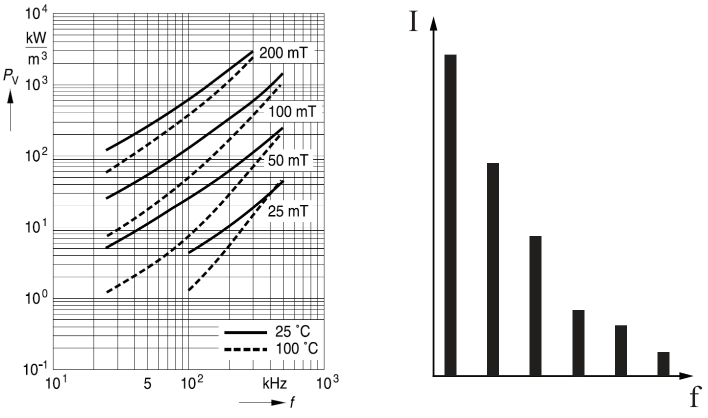

(a)

(b)

Fig. 2.8 (a) An example of the core-loss data-sheet information [34] - core losses for sinusoidal excitation within the relevant range of frequencies and peak magnetic induction. (b) An example of the non-sinusoidal current harmonic spectrum.

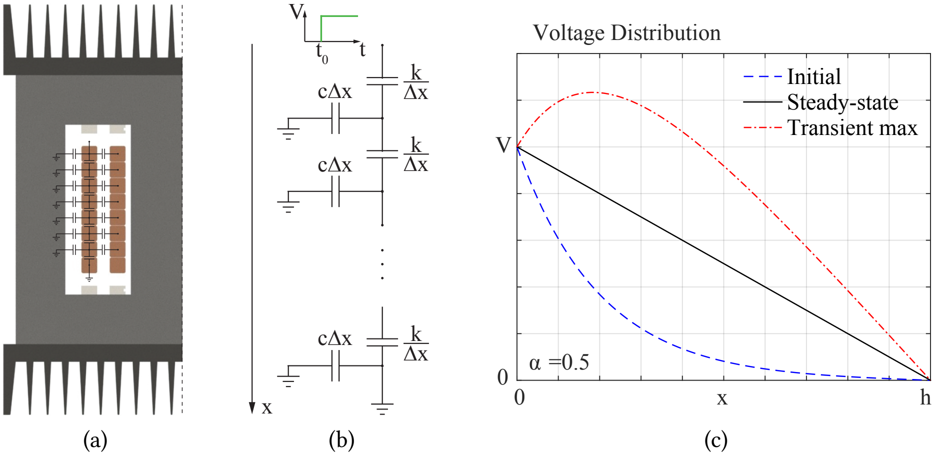

(a) (b) (c)

Fig. 2.9 a) An MFT cross-section detail showing the turn-to-turn and turn-to-ground parasitic capacitances. (b) A simplified HF winding model for the estimation of the initial winding voltage distribution. (c) Plots of the initial winding voltage distribution, envelope of the maximum turn voltages during the HF ringing transient and in the steady state after the transient.

2.3.6 Insulation Coordination

Besides the insulation requirement of each winding or terminal, high dV/dt characteristic for the square voltage waveforms of the fast switching power semiconductor modules can result in high turn-to-turn and turn-to-ground over-voltages, as illustrated in **Fig. 2.9**. At high frequencies, contained in the voltage pulse edges, the turn-to-turn and turn-to-ground parasitic capacitances of the winding cannot be neglected. These cause an uneven initial voltage distribution over the winding turns, thus significantly stressing the turn-to-turn insulation at certain places, as shown in **Fig. 2.9(c)**. Together with the turn inductances, this leads to a so called high frequency ringing transient. As can be seen in **Fig. 2.9(c)**, the outer winding insulation can experience significant (turn-to-ground) over-voltages during this transient.

These effects need to be taken into account at the design stage for any application where the transformer experiences the high dV/dt either during its normal operation (the fast switching of the power semiconductors, especially the emerging wide-band-gap SiC and GaN) or in case of the occasional over-voltage waves such as the basic lightning impulse (BIL).

2.4 State of the Art

The research effort in the area has significantly increased in the past couple of years both in the industry and academia, resulting in many different MFT prototypes, as summarized in **Fig. 2.10** and **Tab. 2.2**. Depending on the required specifications, different materials, technologies and design choices in general are combined to best cope with the aforementioned challenges. As can be seen, there are many possible alternatives for the technology coordination. Each design choice is coupled with several multi-physical characteristics, thus making the navigation through this design space rather complex.

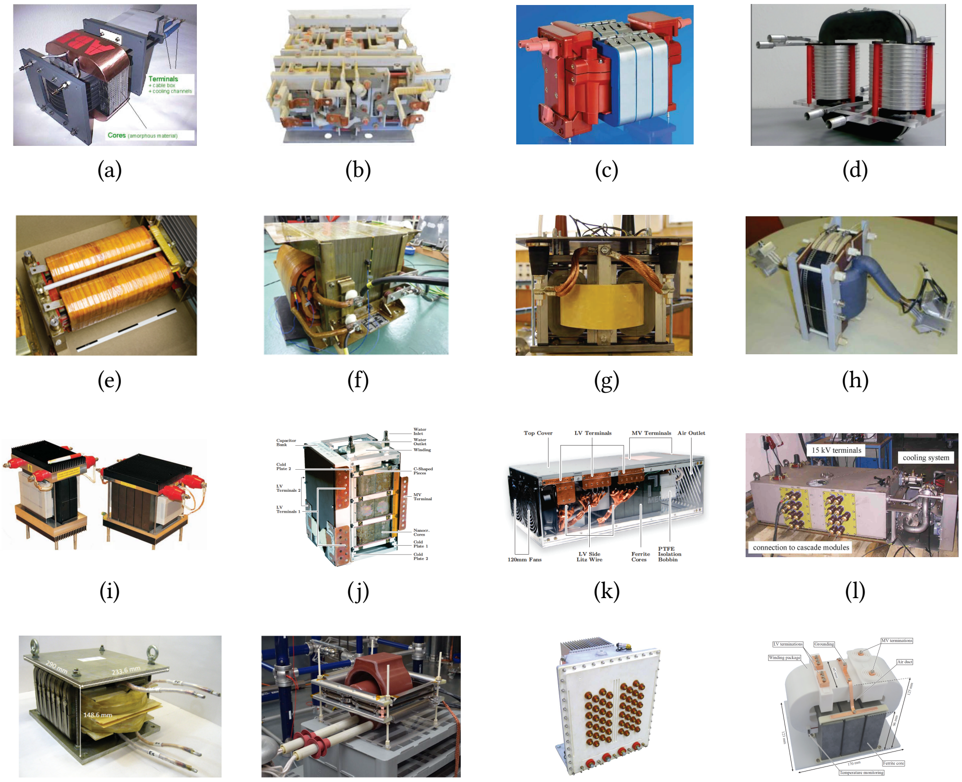

(a) (b) (c) (d)

(e) (f) (g) (h)

(i) (j) (k) (l)

(m) (n) (o) (p)

Fig. 2.10 Documented MFT prototypes from the literature: (a) ABB: 350kW, 10kHz [35]; (b) ABB: 3 × 150kW, 1.8kHz [14], [15]; (c) STS: 450kW, 8kHz [36]; (d) FAU-EN: 450kW, 5.6kHz [37]–[39]; (e) IKERLAN: 400kW, 6kHz [40]; (f) IKERLAN: 400kW, 0.6kHz [40]; (g) KTH: 170kW, 4kHz; (h) BOMBARDIER: 350kW, 8kHz [41]; (i) CHALMERS: 50kW, 5kHz [42]; (j) ETHz: 166kW, 20kHz [43]–[45]; (k) ETHz: 166kW, 20kHz [43]; (l) ALSTOM: 1500kW, 5kHz [16], [17]; (m) EPFL: 300kW, 2kHz [31]; (n) ABB: 240kW, 10kHz [46]; (o) ABB CERN: 100kW, 15 – 22kHz [47]; (p) ETHz: 25kW, 48kHz [48];

Moreover, unlike LFTs operating with sinusoidal excitation at few standardized voltage levels, the specifications of the MFTs depend on the converter topology, resulting in custom excitation waveforms, voltage levels, and insulation requirements. In addition to this, depending on the specific application, some design choices may be prohibited. In that respect, it is hard to make any type of standardization or fairly compare the given MFT prototypes as they are all specially designed and optimized for the given custom operation. Moreover, with few exceptions, there is often very little or no information about any type of insulation testing such as PD or BIL.

This need for customization has compelled the research in the direction of flexible design methodologies and advanced modeling that covers wider ranges of the associated phenomena resulting in several proposed MFT design optimization examples [31], [42], [43], [48]. Similar to these, this thesis focuses on improved modeling and design optimization strategies for the MFTs that facilitate simple and intuitive navigation through the, otherwise very complex and convoluted, set of possible design alternatives.

While it is hard to standardize the MFTs or provide some general design guidelines, some outlines of

Tab. 2.2 Detailed specifications of several representative MFT prototypes from the literature, as given in **Fig. 2.10**.

Design Parameters	**(a)** [35]	**(l)** [16], [17]	**(n)** [46]	**(c)** [36]	**(d)** [37]–[39]	**(h)** [41]	**(j)** [43]–[45]	**(p)** [48]
Construction Type	shell	multi win.	shell	shell	Core	core	shell	shell
P_n [kW]	350	1500	240	450	450	350	166	25
f [kHz]	10	5	10	8	5.6	8	20	48
V_1 [kV]	3	1.8	0.6	1.8	3.6	1	1	7
V_2 [kV]	3	1.65	0.9	1.8	3.6	1	0.4	0.4
Core Material	nano	ferrite	nano	nano	nano	nano	nano	ferrite
Conductor Type	coaxial	Litz wire	Litz wire	Litz wire	hollow tube	hollow tube	Litz wire	Litz wire
Conductor Material	(Al-in, Cu-out)	Cu	Cu	Cu	Al	/	Cu	Cu
Cooling	WF & A	OF	AF	OF & A	O	WF	WF	AF
Insulation	solid	oil	solid epoxy	solid & oil	oil	solid	solid tape	solid epoxy
Density [kW/l]	9.5	2.1	3.6	/	/	/	≈ 32.7	7.4
Density [kW/kg]	7	< 1.5	5.7	9	11.8 – 18.8	7	≈ 16.6	4
PD Test [kV]	38	/	53	37	/	33	/	/
BIL Test kV	95	/	150	/	/	100	/	/

Where: W, A and O stand for water air and oil cooling, respectivelly; F stands for forced cooling; nano is short from nanocrystalline;

the dominant technologies and materials can be established, thus defining the design space of interest, as will be discussed in detail in the following chapter. Employing advanced modeling, as will be described in **Chaps. 4** and **5**, the full potential of this design space can be explored allowing a simple identification of the best performing alternatives in respect to the specific desired MFT features (e.g. volume, mass, efficiency, maximum hot-spot temperatures, etc.), as given in **Chap. 6**.

2.5 Summary

According to the scaling laws, there is a great potential for the reduction of the MFT size and relative cost with the increase of the operating frequency. However, this frequency scaling is tied to several challenges. From the electromagnetic aspect, the operation at elevated frequencies leads to additional losses and high dV/dt, characteristic for the operation within power electronic converters, results in increased dielectric stress. Non-sinusoidal current waveform, containing higher order harmonics, leads to further increase of the frequency dependent winding losses.

Moreover, the size decrease on its own implies decreased cooling surfaces resulting in higher thermal impedance towards the ambient and higher hot-spot temperature gradients. Therefore, the thermal equilibrium is disturbed from both sides, due to the increased losses and the weakened cooling. In addition to this, the high frequency core and winding structures feature electromagnetic anisotropy for mitigation of the frequency related losses. This anisotropy also translates to their thermal properties, making the thermal coordination even more complicated and coupled with the electromagnetic features. In addition to this, with respect to the variety of the applications and depending on the converter topology, MFT specifications can vary drastically from one application to another.

Therefore, the design of the MFTs is a complex task, featuring nonlinear coupled multi-physics. The need for design customization within the wide range of specifications, required in various power electronic applications, while taking into account a relatively large number of design choices, can only be served with a well established design optimization framework, powered by advanced models featuring a wide application range.

3

Design Optimization Process

This chapter provides a high-level description of the entire MFT design process - from desired features and specifications to the selection of the optimal design. Different inputs and processes are classified and their inter-relations analyzed considering performance, cost and complexity. This qualitative description defines the requirements for each section of the aforementioned process, thus setting the basis for the remainder of this thesis.

3.1 A High-Level Description

At the highest level, any design process starts with a set of specifications and desired features and should end with a design that yields these requirements, as depicted in **Sec. 3.1**. Naturally, there is a multitude of different ways how this can be accomplished. In that respect, the considered design space has to be defined, consisting of preferred or prohibited construction types, design choices, materials etc. Finally, some sort of design optimization is deployed to identify the optimal MFT design, within the considered design space.

This chapter is organized as follows. A detailed description of the features of interest is provided

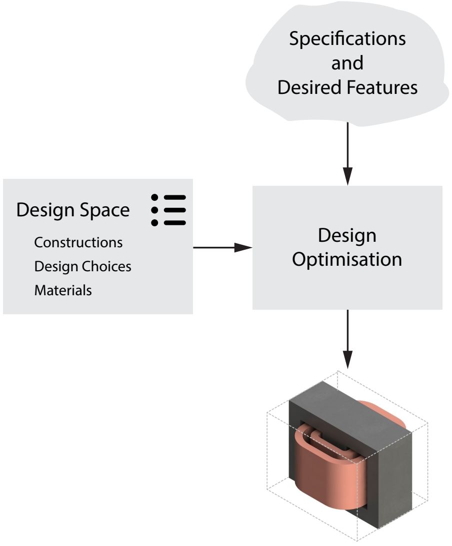

Fig. 3.1 (a) A high-level overview of the entire design optimization process - from desired features and specifications to the optimal design.

in **Sec. 3.2**. An analysis and classification of the design space is given in **Sec. 3.3**, while the exact treatment of these inputs, the design process itself, representing the core of this thesis, is described in detail in **Chaps. 4** to **6**.

3.2 Relevant Features and Specifications

The starting point of any design is a defined set of specifications and desired features. While industrial specifications normally contain an extensive list of features and required standars, covering all sorts of effects such as ageing, pollution, smoke and chemical content emission in case of fire etc., this thesis takes into account only a reduced set of these parameters that are directly tied to the performed study.

3.2.1 MFT Features and Specifications

The set of the most relevant MFT features for this study can be classified into four groups:

1. **Electric parameters:**
    - P_n - Nominal power
    - V_1,V_2 - Primary and secondary winding input voltage maximum
    - D - Duty cycle
    - η - Efficiency
    - f_{sw} - Operating frequency
    - I_i - Current Fourier series coefficients
    - L_σ - Total leakage inductance
    - L_m - Magnetizing inductance
2. **Dielectric parameters:**
    - dV/dt - Excitation voltage slope
    - V_{ins1},V_{ins2} - Rated primary and secondary winding insulation
3. **Thermal parameters:**
    - T_∞ - Temperature of the surrounding fluid
    - Cooling type - Forced or natural convection
    - Available convection surfaces
    - Any possible fluid flow impediments due to integration

4. **Mechanical parameters:**[1]
    - W_t, L_t, H_t - Total width, length and height, respectively
    - V_t - Total volume
    - M_t - Total mass

All of the electric and dielectric parameters are directly governed by the converter requirements. While most of these are self explanatory, others require some additional discussion. Under the assumption of the MFT operation within either an SRC or DAB converter, the voltage waveform is a simple square waveform fully defined via the maximum value and the duty cycle of the signal. In case of a more complex waveform, which cannot be considered quasi sinusoidal or square, the whole waveform would have to be specified and directly taken into account. Moreover, as mentioned in **Sec. 2.3.5**, depending on the converter topology, the MFT current may include a significant higher order harmonic content, such as the case with a DAB. Due to the frequency dependency of the winding losses (skin and proximity effects), the entire current harmonic content (portion carrying non-negligible power) should be taken into account.

As discussed in **Sec. 2.3.4**, the leakage and magnetizing inductance both represent important design parameters on the converter level. Therefore, unlike in the case of LFTs, their accurate design also falls under the category of desired features. Moreover, maximum V_{ins} and dV/dt of each winding in a normal operation should be defined as they reflect on the overall and turn-to-turn insulation level, respectively. Especially nowadays, with the proliferation of wide band gap devices such as SiC and GaN, dV/dt may be disruptively high and call for special design considerations [50].

On the other hand, depending on the environment and integration, the specific cooling conditions need to be defined and taken into account. Special attention should be given to making sure that the assumed cooling conditions at the design stage are matching as well as possible the real cooling conditions, after the MFT integration into the system. Finally, custom integration may imply specific restrictions on one or more transformer dimensions, volume or wight.

3.2.2 Additional Features

Besides the desired features of the MFT, the complexity and cost of the design are also very important figures of merit. These are mainly affected by:

- Selected design choices
- Selected materials
- Standard vs. custom components

Design complexity refers to the manufacturability. Within the design optimization, the designs utilizing techniques or components that are difficult to manufacture or assemble can be penalized or completely excluded. Similarly, if not predefined, the overall coordination of the design choices may have a detrimental impact on the resulting cost and time delays. As an example, epoxy casting of the windings is far more complex, expensive and time consuming compared to simple air insulation. Any

---

[1] All of the mechanical dimensions refer only to the active part of the transformer - virtual box that can be fitted around the active part (see **Sec. 3.1**), as recommended in [49] as the representative criteria for design comparison.

possible workaround that still meets the specifications may prove optimal in that respect. Selected materials on the other hand will mostly have an impact on the the total cost.

Another important factor is the standardization of the components. Custom made components are always tied to increased lead time and usually not available or quite expensive in small series. In other words, being able to find fitting design alternatives, utilizing the standard off-the-shelf components, is an interesting functionality.

Depending on the initial specifications, all of these features and any others that can be modeled/quantified can be taken into account at the design optimization stage, as will be described in detail in the following chapters.

3.3 Design Space

While the aforementioned set of features describes the goals and constraints, the design space defines all of the possible design alternatives: MFT construction types, design choices and materials.

3.3.1 Construction Types

There are several dominant MFT construction types, as summarized in **Fig. 3.2**. Each construction type has specific strengths and weaknesses. In case of a shell construction, depending on the proportions, a large portion of the windings is inherently shielded by the core resulting in less EMI compared to the core and C-type. While this allows for a good integration, it also implies that the cooling surfaces of the windings are less accessible to the cooling media, resulting in harder thermal coordination. From the aspect of volume and mass, for the same transformer (same core and winding cross-sections), the shell type transformer is slightly better due to the shorter equivalent magnetic path through the core.

Another interesting alternative is the planar construction [51]–[54]. Compared to the three aforementioned construction types, it yields higher volume and mass for the same core and winding cross-sections due to the higher winding MLT. However, it features much larger surfaces per same volume due to the flat shape that imply both more efficient convection cooling and shorter heat conduction paths from hot-spots to the nearest cooling surfaces. Moreover, due to the disk winding construction, the cooling media has a good access to the thermally most critical winding and inner core surfaces - long uninterrupted channels for either natural or forced fluid convection in-between the windings and the core.

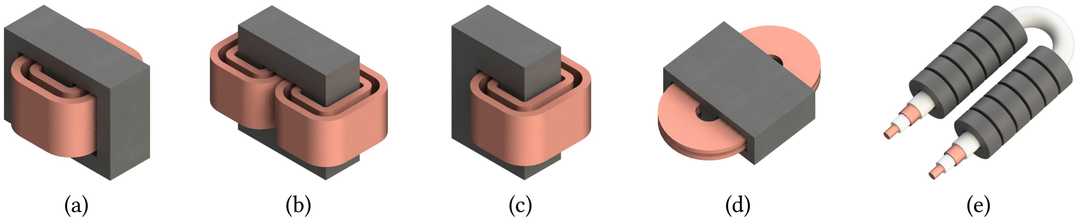
(a) (b) (c) (d) (e)

Fig. 3.2 MFT construction types: (a) shell type, (b) core type, (d) C-type, (d) Planar/Disk type, (e) coaxial type.

Finally, coaxial transformers represent a special construction type that inherently offer full shielding. Moreover, they feature a symmetric electromagnetic field distribution which can be analytically modeled with relatively trivial formulas. In addition to this, the application of any dielectric standard is relatively simple due to the relatively constant electric fields - there are no edges and corresponding local electric field maximums. However, only $1 : 1$ transformation ratio is possible in its simplest version with a standard coaxial cable, as shown in **Fig. 3.2(e)**. An arbitrary transformation ratio can also be achieved but with more complicated constructions, such as described in [55].

3.3.2 Design Choices

3.3.2.1 Conductor Types

There are several widely used MFT transformer conductor technologies, as given in **Fig. 3.3**. Frequency dependent conduction losses, due to the skin and proximity effect, are one of the main parameters governing the choice of winding conductor technology. Due to the relatively low cost and good mechanical and thermal properties, foil and bar conductors are usually preferred at moderate frequencies up to several kHz. Nevertheless, the minimum foil or bar thickness is limited, and depending on the winding construction, these may experience significant additional loses due to the edge effect - especially in case of foil windings at higher frequencies.

Therefore, at higher frequencies above 5kHz, fine-stranded Litz wire represents a dominant technology of choice. It comes in various shapes and sizes: flat, round, square, with cooling duct in the middle, etc. Due to the very small diameter of the isolated strands, skin and proximity effects are greatly mitigated. Moreover, the edge effect is practically canceled due to the isotropic skin and proximity mitigating properties, from any radial direction.

While solid hollow conductors can offer good mechanical and very good thermal properties, depending on the construction and operating frequency two out of four of its conductive sides will suffer from very strong frequency dependent eddy current losses. This effect becomes more pronounced with the increase of frequency, potentially having a major impact on efficiency and necessary heat exchange effort. In other words, this type of technology is more interesting for lower frequency high-power (high current density) designs.

Coaxial cables on the other hand are used as a part of the special coaxial transformer design. The analysis of this type of transformer is quite different compared to the others, and as such is outside of the scope of this thesis.

(a) (b) (c) (d) (e)

Fig. 3.3 Conductor types: (a) foil, (b) bar, (c) Litz wire, (d) hollow conductor (solid or Litz), (e) coaxial cable.

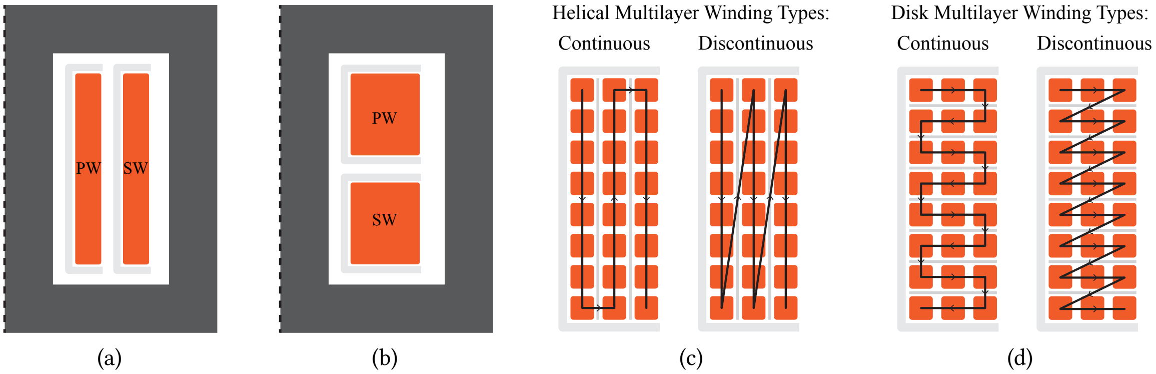

Fig. 3.4 Winding arrangement: (a) Cylindrical and (b) Disc. Multilayer winding types: (c) Helical and (d) Disc.

3.3.2.2 Winding Arrangements

Another important design choice is the arrangement of the windings and conductors within them, as given in **Fig. 3.4**. There are two main winding arrangements, cylindrical and discs. The cylindrical windings are concentrically stacked, whereas the disc windings are stacked axially, one on top of another, as shown in **Figs. 3.4(a)** and **3.4(b)**. This has implications on the electric, dielectric and mechanical properties.

Depending on the specific geometry ratios, the cylindrical winding construction will result in a lower leakage flux density and the corresponding leakage inductance, compared to the disc arrangement with the same number of turns. Moreover, higher leakage flux density in disk windings results in a more pronounced proximity effect and the increase of the frequency dependent AC resistance. Nevertheless, it is usually easier to implement good inter-winding insulation in case of the disk windings, as they are inherently better separated.

Note that the aforementioned conclusions do not hold for the planar transformer construction, as a special case of the disk winding transformer with extreme ratios - very low profiled windings. From the 2D electromagnetic point of view, the planar transformer construction can be seen as equivalent to the cylindrical, as shown in **Fig. 3.4(a)**, just rotated for 90°.

Interleaving of the windings is another interesting possibility, but rather avoided in MV rated designs. While this is a very powerful technique for reducing the leakage inductance and AC resistance of the LV transformers operating on high frequencies, the added volume, necessary to facilitate MV inter-winding insulation between each of the interleaved layers, is usually prohibitive.

The insulation problem also extends within the winding, particularly in case of multi-layer construction. Two main conductor winding/stacking techniques are described in **Figs. 3.4(c)** and **3.4(d)**. As can be seen, in case of a continuous winding, the potential difference of the two neighboring conductors in successive layers is two times higher compared to the discontinuous case. Nevertheless, the discontinuous winding requires a return conductor after each layer, thus complicating the design and increasing the length of the conductor and the resulting DC resistance. The choice of the appropriate alternative boils down to the trade-off between the complexity of adding the return conductor versus reinforcing the inter layer insulation.

3.3.2.3 Thermal Coordination

Regardless of the design, all of the generated heat needs to be exchanged with the surrounding fluid at some point. Depending on the fluid used as a cooling media, there are three dominant convection cooling concepts.

- Air
- Oil
- Water

In the case of the first two, windings or windings and the core, are usually completely surrounded with the given fluid, allowing both natural and forced convection. On the other hand, in the case of water, its access is usually restricted to the circulation through the cooling channels, thus requiring a forced flow.

Due to the fluid properties, the oil offers a much stronger convective cooling compared to air. However, oil designs tend to be heavier, due to the oil volume, surrounding case and the radiators and in general more complex. Water cooling is combined with either air or oil to enhance the cooling effort. In first case, various strategic surfaces of the transformer are equipped with aluminum coolers with water channels. In the second, water to oil heat exchanges are utilized.

The selected cooling concept will mostly depend on the integration. For example, in case the MFT is operating within a water cooled converter, this may be an interesting option as it requires minimal additional elements. Otherwise, the added volume and cost of installing the water cooling system just for a transformer is usually prohibitive. Similarly, oil is usually avoided for applications in fire-hazardous or pollution-sensitive environments such as food industry etc.

3.3.2.4 Insulation Coordination

Ensuring electric insulation of all the components within the transformer that are on different potentials is paramount. Unfortunately, on a basic electro-chemistry level the dielectric properties of any material are reverse proportional to its thermal conductivity. In that respect, insulation coordination is always strongly tied to the thermal coordination. The three main insulation concepts can be classified into three groups:

- Air
- Solid
- Oil

Air insulation assumes conductors, bare or with some sort of dielectric coating (e.g. enamel), suspended in the air on some sort of solid supporting structure made out of a dielectric material - coil former. This concept features a good access of the cooling fluid to the winding hot-spots, thus allowing for effective cooling.

Solid insulation on the other hand offers a drastic decrease of the necessary dielectric distances due to the excellent dielectric properties of the cast epoxy resin (≈ 45kV[46]) compared to air (≈ 3kV[56]). Depending on the required insulation level, it may allow a significant increase in power density.

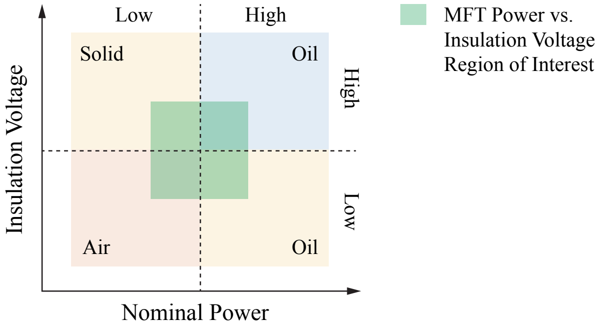

Fig. 3.5 A qualitative map of the preferred insulation concepts in the nominal power versus the required insulation voltage axis.

Nevertheless, the access of the convection cooling is blocked for the inner parts of the winding, relying only on the heat conduction through the resin and conductors. This usually results in harder cooling conditions due to the low thermal conductivity of the cast epoxy.

Finally, the case of the oil design is very similar to the air design, except that the oil has an order of magnitude better dielectric properties (≈ 50kV[57]) compared to air. Moreover, different materials are used for local conductor coating (special paper), coil former construction and the widths and construction of the cooling channels/gaps is different - designed to maximize the convective cooling with respect to very different fluid properties of the air and oil.

Qualitative conclusions about the preferred insulation concepts in respect to nominal power and required insulation level are summarized in **Fig. 3.7**. While it is relatively easy to identify the dominant technologies in extreme cases, the optimal choice at the considered power and insulation levels for MFTs is not straight forward. Depending on the specific requirements the optimal design may fall into any of these four quadrants.

Finally, similar to the choice of the cooling concept, the insulation options may be restricted depending on the integration and the additional application-specific environmental constraints.

3.3.2.5 Auxiliary Elements

Besides the main active parts, the core and the windings, and the necessary insulation, any transformer consists of many other auxiliary elements:

- Core clamp
- Winding support
- Air gap
- Interfacing material
- Termination

In case of laminated, cut, or simply stacked cores, some sort of core clamp needs to be employed to mechanically support the whole structure. This clamping structure is usually made of metal because of its mechanical strength. From electrical aspect, if not properly designed, conductive material may be introduced into areas with high magnetic fields thus generating additional eddy current losses and heat. Moreover, in case of HV designs, special design or shielding is required to avoid PD [46], [48].

It is important to properly take into account the surfaces available for convection cooling at the design stage. In that respect the structure of the coil formers and other supporting elements should be defined and its effect on the cooling conditions accounted for - excluding the convection cooling surfaces of the windings and the core that are covered by supporting elements, if significant in size.

Cut cores are often used in order to linearize the operating B-H characteristic of the core, control the equivalent magnetic permeability or simply to facilitate a fast and easy assembly - independent manufacturing of the windings and assembly with the core. Depending on the air gap length some amount of flux fringing occurs. Large air gaps that generate a strong fringing flux can result in additional losses and very high local core temperature, particularly in case of anisotropic cores where the eddy current canceling properties are not the same in all directions. In these cases, the air gap should be distributed into several smaller ones - small enough to mitigate this effect to a reasonable level. Moreover, fringing flux may also generate additional loses in windings or any other surrounding conductive elements in close vicinity. This consideration should be taken into account at the design stage and mitigated as much as possible by proper positioning of different elements and the air gap. Distributing the air gap can also help in this case to decrease the affected area around the air gaps, but this again introduces additional cost and complexity.

In case of larger MFTs, two or more cores are often stacked together to achieve the desired core dimensions. Interfacing the surface of the core with any other solid surface, another part of the core or the clamping structure, should not be done directly, particularly in case of very brittle materials such as ferrites. Clamping them together requires some interfacing material that is elastic enough to mechanically amortize the slight differences in dimensions that are always present due to the manufacturing tolerances. Note that this does not represent an issue when it comes to small single core magnetic components such as the ones on PCBs.

Depending on the used materials termination of the transformer conductor may not be trivial - e.g. joining the aluminum foil and a copper terminal or terminating a large cross section Litz wire. Finally, from the integration point of view it is important to know the desired position of the terminals and whether they are supposed to mechanically support other construction elements etc.

3.3.3 Materials

3.3.3.1 Core Materials

At the basic level, the characteristics of the transformer are governed by the characteristics of the utilized materials. Taking into account a broad definition of the medium frequency range from 0.5 to 50kHz, there are several dominant core materials:

- Grain oriented electrical steel
- Metglas
- Nanocrystalline
- Ferrites

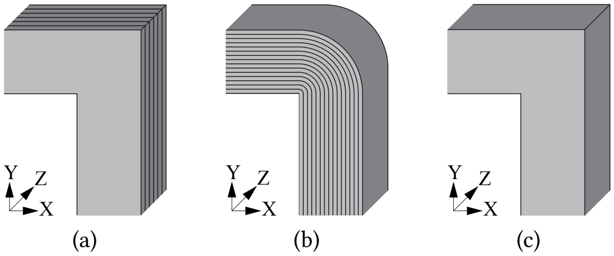

Fig. 3.6 Considered core structures: (a) axial lamination (in Z axis); (b) radial lamination; (c) isotropic;

These can be classified based on their construction in three groups, as given in **Fig. 5.17**. Low frequency iron alloy based cores used in the traditional LF transformers are usually made out of axially stacked lamination sheets, as shown in **Fig. 5.17(b)**. The same approach is used with their more sophisticated successor, the grain oriented electrical steel (GOES), with improved core loss characteristic. The lamination thickness of the lamination goes down to 180μm offering relatively acceptable eddy current loss suppression at frequencies up to 1 – 2kHz [58]. Due to the high saturation induction (up to 2T), excellent mechanical robustness and resilience to very high temperatures (up to 400°C), this material represents a very interesting alternative for MFTs designed for operation in hard conditions at modest frequencies.

At higher frequencies, eddy current and excess losses of the GOES materials are usually prohibitive. Another type of laminated cores are the radially laminated wound strip core materials (**Fig. 5.17(c)**) such as metglas and nanocrystalline, with very thin strip width 18μm allowing to keep the eddy current losses at a reasonable level at elevated frequencies, roughly up to 50kHz [59]. These materials however feature lower saturation inductions 1.56T and 1.23T, respectively, and maximum operating temperature of 155°C. Moreover due to the very low thickness and material properties the strips are relatively brittle. While metglas features a higher saturation induction compared to nanocrystalline, its losses are roughly 3 – 5 times higher within the frequency range from 1 to 50kHz.

Finally, at high frequencies, above 50kHz, isotropic ferrite cores are usually used, as displayed in **Fig. 5.17(a)**. Ferrites are non-conductive ceramic materials with still good ferromagnetic properties, made by mixing large proportions of iron oxide with small proportions of one or more additional metallic elements, such as barium, manganese, nickel, and zinc [60]. Due to the very low conductivity of the material the eddy current portion of the losses is practically negligible, thus allowing relatively efficient operation even at very high frequencies. However, regarding the ferromagnetic properties, their relative magnetic permeability is an order of magnitude lower compared to the aforementioned laminated materials, generating the so called distributed air-gap effect. They also feature a relatively low saturation induction of around 0.3 – 0.4T. Moreover, ferrite cores are mechanically brittle due to the ceramic structure. This poses restrictions on the core size and proportions and ultimately the application area.

It can be seen that similar to the trade-off in insulation materials (dielectric versus thermal properties), in the case of core materials the main trade-off lays between the electric conductivity and magnetic properties, relative permeability and saturation induction. Moreover, it is important to mention the influence of the core construction on the thermal conductivity. Same as for the electromagnetic properties, laminated cores feature an anisotropic thermal conductivity: (i) relatively high along the lamination plane, defined by the strip material properties; (ii) relatively low in direction normal to

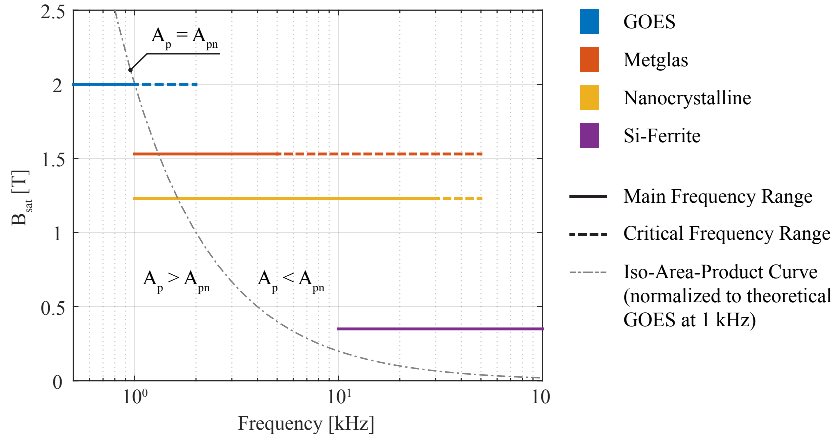

Fig. 3.7 A qualitative map of the core materials in the saturation induction versus the operating frequency axis.

the lamination, affected by the low conductivity of the necessary inter-strip insulation. This should be taken into account at the design stage in order to achieve the optimal thermal coordination.

A chart of the theoretical magnetic saturation of the available core materials, in respect to the operating frequency is given in **Fig. 3.7**. The rough estimation of the critical frequency range where the core losses become thermally prohibitive is depicted with dashed lines. An iso-area-product curve, normalized to the theoretical area product of the MFT made with GOES and operating at 1kHz is constructed to illustrate the influence of the frequency and the core material on the the transformer size. As generally known, it can be seen that the materials with higher B_{sat} yield a more compact design for a given frequency. Moreover, it can be seen that even though the core materials for higher frequencies have a lower B_{sat}, they will still yield higher power density ($A_p < A_{pn}$) at elevated frequencies. This is an important qualitative conclusion as it shows that the inherent technological curve of the core materials does not bound potential for the MFT size reduction with the increase of the operating frequency.

3.3.3.2 Conductor Materials

A large portion of the significant effects on the conduction loses and thermal management of the windings are a result of the selected conductor type, as discussed in **Sec. 3.3.2.1**. Nevertheless, at the basic level, there are two main conductor materials governing the MFT behavior:

- Copper
- Aluminum

Relevant properties of these materials are summarized in **Tab. 3.1**. Copper, with its excellent electric conductivity, features lower DC resistance of the windings compared to aluminum. At high frequencies however, as discussed in **Sec. 2.3.1**, the copper conductors are more prone to the additional skin and proximity losses. Moreover, as can be seen in **Tab. 3.1**, aluminum has a significantly lower relative wight compared to copper. This makes aluminum an interesting design alternative for MFTs, especially for applications where high gravimetric power density is required.

Tab. 3.1 Conductor material characteristics at 20°C [61], [62]

Conductor Material	$\rho_e[\Omega\,\mathrm{m}]$	$\alpha_e[1/^\circ\mathrm{C}]$	$\rho[\mathrm{kg/m^3}]$	$\alpha_l[1/^\circ\mathrm{C}]$
Copper	$1.68 \cdot 10^{-8}$	$3.862 \cdot 10^{-3}$	8940	$17 \cdot 10^{-6}$
Aluminum	$2.82 \cdot 10^{-8}$	$3.9 \cdot 10^{-3}$	2712	$23.1 \cdot 10^{-6}$

where ρ_e and α_e are the electric resistivity and temperature coefficient, while ρ and α_l are the density of the material and the coefficient of the linear thermal expansion, respectivelly.

3.4 Summary

A high-level description of the design optimization process and its necessary inputs has been provided. The desired features, specifications and available technologies and materials and their implications on the MFR design are discussed in a qualitative manner. As already mentioned in **Chap. 2**, it can be seen that there exists a wide variety of different design choices, all having coupled effects on several MFT characteristic. This makes the identification of the optimal design and technology combinations very complicated.

To that end, a design-optimization framework, capable of taking into account all of these technologies and their effects is needed to exhaustively explore all of the feasible design alternatives and help to identify the optimum. This is described in detail in the following chapters. A detailed description of the related advanced modeling techniques the design optimization process are provided in **Chaps. 4** and **5** and **Chap. 6**, respectively.

4

Analytical Modeling

This chapter provides a detailed overview of the available analytical models, covering all the relevant phenomena governing the electrical and thermal behavior of the MFT and limiting its operation range. These are analyzed, compared and optimized in terms of accuracy and execution speed, both paramount figures of merit for any type of design optimization application. Several modifications are proposed, improving both the estimation accuracy and extending the validity range of the given models.

4.1 Introduction

Any design optimization relies on some form of mathematical description of the relevant underlying physics. The quality of the whole process boils down to the right trade-off between accuracy and execution speed of the utilized models. A qualitative analysis of different classes of models in this respect is given in **Fig. 5.1**. While FEM could be used to provide a detailed and very precise modeling framework, its computational cost is often too high and numeric convergence issues may occur when dealing with complex geometries featuring coupled multiphysics. Thus, analytical models, offering a good trade-off between accuracy and computational cost, are preferred when it comes to the overall optimization of a complex system, as displayed in **Fig. 4.1(a)**.

In that respect, some of the oldest analytic models, developed well before computational power allowed

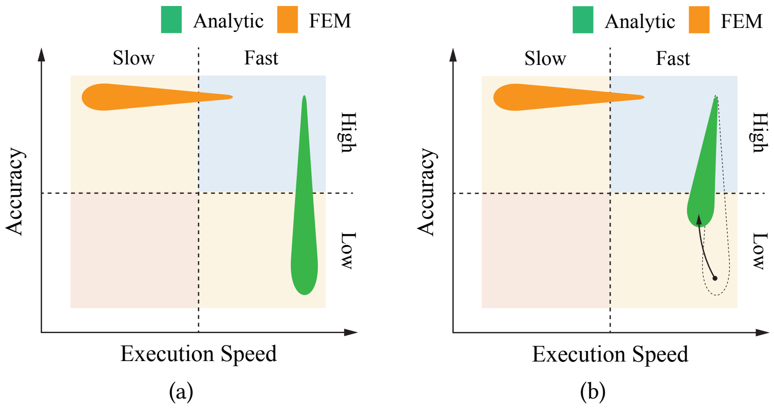

Fig. 4.1 Qualitative analysis of the properties of various classes of models: (a) Analytic and FEM; (b) Inclusion of various correction factors into analytic models to compensate for simplifications and approximations and improve the estimation accuracy for a number of isolated cases.

the numeric solution of partial differential equations via FEM, are now experiencing a renaissance within design optimization applications. Computationally light analytic models perform extremely well as long as the necessary approximations/assumptions hold within reasonable accuracy limits.

Unfortunately, both electromagnetic and heat transfer equations in 3D have an exact closed-form analytic description only for a very limited class of special problems, featuring either full concentric symmetry or extreme relative ratios of certain dimensions that can be considered infinite and edge effects neglected in the averaging. In order to extend the validity range, any other more complex geometry of interest is interpreted as a reduced and approximated equivalent which fulfills one of the two aforementioned properties. However, depending on the strength of the involved assumptions, the estimation errors introduced as a side-effect of this reduction are often a limiting factor.

Therefore, a great deal of scientific effort has been directed into improving many of the aforementioned inherited legacy models - a significant number of corrections (e.g. correction factors) has been developed over the years to compensate for these errors and improve the accuracy of the specific, especially important models, as can be seen in **Fig. 4.1(b)**. The ones relevant for the MFT design optimization are described in this section. Moreover, several modifications, both improving the estimation accuracy and extending the validity range, are proposed and described in detail.

4.2 Core Losses

While the best practice is to characterize the core losses under the exact given operating conditions, this is often not an available alternative at the design stage. Some sort of modeling is therefore required in order to provide a reasonable estimation.

4.2.1 Literature Review

Depending on the application, there are several different approaches to core loss estimation, as summarized in [31]. These can be classified in the next four categories:

1. Based on characterization of magnetic hysteresis [63]–[65]
2. Based on loss separation [66]
3. Time domain core loss models [67]
4. Based on Steinmetz equation [67]–[69]

Due to its simplicity and more importantly the well established convention, the most relevant class of models for transformer design recurring in the literature is based on the original Steinmetz equation (4.1) [68], [69]

$$P_c = K f^{\alpha} B_m^{\beta} \tag{4.1}$$

where K, α and β are the Steinmetz loss coefficients, f is the excitation frequency and B_m the magnetic induction amplitude.

When it comes to sinusoidal excitation, the original Steinmetz equation (4.1) has been traditionally used in the LFT design and has become a golden standard [30], [70]. Respective Steinmetz parameters

(K, α and β) fitted to the loss measurements on core samples excited with sinusoidal excitation are usually provided by manufacturers for different materials as a standard format, facilitating simple loss estimation and comparison.

Depending on the core construction and material, other types of models may offer a more accurate estimation within a wider range of operation [66]. For example, models based on loss separation

$$P_c = \underbrace{K_h f B_m^{\beta}}_{\text{Hysteresis loss}} + \underbrace{K_e (f B_m)^2}_{\text{Eddy current loss}} + \underbrace{K_a (f B_m)^{1.5} f^{1.5}}_{\text{Anomalous loss}} \tag{4.2}$$

are a natural choice for laminated cores such as silicon steal, metglass, nanocrystalline, etc.

While these models work well with sinusoidal excitation, they cannot directly be applied to an arbitrary square wave, typical for power electronic applications, as given in **Fig. 4.2**. Given the wide variety of power electronic applications and different operating conditions experienced by the magnetic core, comprehensive characterization from the manufacturer side, as in case of the sinusoidal excitation, is impractical. Therefore, some sort of generalization is necessary to facilitate appropriate estimation of core losses for an arbitrary excitation waveform, yet based only on the known properties characterized at standard test conditions - sinusoidal or some other defined standard excitation waveform.

The time domain core loss model derived in [67] uses the loss separation principle to derive the time domain expressions for core loss due to eddy currents, hysteresis and excess anomalous loss which can then be applied to an arbitrary waveform. Similar to this idea, all of the models based on generalization of Steinmetz equation [68], [69] and [67] derive the time domain loss expression from the original Steinmetz equation that can be applied to the given arbitrary waveform in order to find the time-average loss density in a general case. The main difference between these models is in the assumptions and form in which they define these time domain loss expressions. According to the error comparison performed in [31], the IGSE provides the best estimation accuracy.

Some more recent research on the topic [71] offers even further generalization of the IGSE that takes into account the so called magnetic relaxation, specific for ferrite materials operated at high frequencies (greater than 25kHz) with non-negligible zero voltage excitation periods [72]. However, this improved estimation comes at a cost of introducing five more parameters which are not normally provided by the supplier and have to be empirically defined through characterization.

4.2.2 Application of the IGSE

For the purposes of multiphysical optimization of the MV MFT, the IGSE is chosen as the most optimal and comprehensive method for the estimation of the core losses. The main benefits of this method are:

- High accuracy within the operation range of interest
- Requires only standard data-sheet information
- Simple algorithm for evaluating the losses

The practical application of the IGSE starts from the original Steinmetz equation for calculation of average loss density in the magnetic material for sinusoidal excitation, as given in (4.1). As already

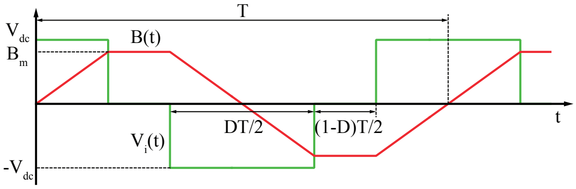

Fig. 4.2 Characteristic flux density waveform caused by a generic three-level converter voltage waveform.

mentioned, the standard Steinmetz coefficients (K, α and β) used in this equation are usually either directly provided by the supplier or can easily be inferred from the given core loss curves.

The IGSE (4.3) generalizes the Steinmetz equation (4.1) in order to extend the validity of its loss estimation to any arbitrary non-sinusoidal waveform. This is done under the assumption that the instantaneous core losses are a function of the peak-to-peak magnetic induction value and its instantaneous rate of change

$$P_c = \frac{1}{T}\int_0^T k_i \left|\frac{\mathrm{d}B(t)}{\mathrm{d}t}\right|^{\alpha} (\Delta B)^{\beta-\alpha}\mathrm{d}t \tag{4.3}$$

where T is the electric period and ΔB is the peak-to-peak magnetic induction. The coefficient k_i is given in (4.4). It is derived by evaluating the IGSE (4.3) for a sinusoidal magnetic induction waveform and respecting the equivalence to the result of the original Steinmetz equation (4.1).

$$k_i = \frac{K}{(2\pi)^{\alpha-1}\int_0^{2\pi}|cos(\theta)|^{\alpha}2^{\beta-\alpha}\mathrm{d}\theta} \tag{4.4}$$

The denominator in (4.4) contains a numeric integral. In order to avoid the computationally costly numeric integral in the model expression, a numeric integration of this integral within a relevant range of α values (from 0.5 to 3) and curve fitting of these results have been performed in [68]. As a result a closed form solution has been derived in form of equation (4.5) with less than 0.15% error in the entire α range.

$$\int_0^{\pi/2}|cos(\theta)|^{\alpha}\mathrm{d}\theta = \left(0.2761 + \frac{1.7061}{\alpha + 1.354}\right) \tag{4.5}$$

Substitution of (4.5) in (4.4) leads to a trivial analytic expression

$$k_i = \frac{K}{2^{\beta-1}\pi^{\alpha-1}\left(0.2761 + \frac{1.7061}{\alpha+1.354}\right)}. \tag{4.6}$$

On the other hand, the arbitrarily modulated square voltage waveform of interest and the resulting magnetic induction, covering applications such as DAB and SRC, are shown in **Fig. 4.2**. The absolute value of the instantaneous magnetic induction rate of change can be expressed as a function of the excitation voltage duty-cycle

$$\left|\frac{\mathrm{d}B(t)}{\mathrm{d}t}\right| = \begin{cases} 0 & \text{for } (1-D)T \\ \dfrac{2\Delta B}{DT} & \text{for } DT \end{cases} \tag{4.7}$$

where D is the duty-cycle, T is the electric period and ΔB is the peak-to-peak magnetic induction. Substitution of (4.7) in (4.3) and solution of the integral leads to the closed form expression for the core loss density

$$P_s = 2^{\alpha+\beta} k_i f^{\alpha} B_m^{\beta} D^{1-\alpha} \tag{4.8}$$

where $B_m = \Delta B/2$ is the magnetic induction peak-to-peak amplitude.

Finally, a simple analytical, computationally non-intensive, core loss density model is defined with (4.6) and (4.8), for the waveform family of interest, allowing fast execution while only using the available data sheet information.

4.3 Winding Losses Modelling

Beside the core losses, winding losses are the second major contributor to the total MFT losses, directly responsible for the hot-spot temperature gradients and resulting efficiency. In that respect, their accurate estimation is paramount, both from performance and safety point of view.

4.3.1 Literature Review

Similar to the core loss estimation, several different analytic winding loss models have been developed over the years, covering the most relevant geometries and applications. An extensive review and comparison of these can be found in [31], [73]. Accuracy of various mathematical expressions are compared with the detailed winding FEM simulation results in [31] providing good insight into their validity range. On the other hand, a handbook-like description of best practices, consisting of many different models and specific correction factors, covering a wide spectrum of applications can be found in [73].

4.3.2 Dowell's Model

One of the oldest and most relevant modeling frameworks is the Dowell's model [74] that provides a frequency dependent expression for winding losses based on the solution of electromagnetic equations in 2D. It was initially developed for foil transformer windings, but as will be described in detail, its validity extends to a variety of different winding constructions.

Dowell's methodology is based on two very important assumptions that allow the solution of the 3D electromagnetic fields:

- Difference in the field distributions of the portions of the windings inside and outside of the core window area is neglected. In other words, it is considered that the per-length characteristics (e.g. magnetic energy, Ohmic losses, etc.) that are extracted by solving a 2D detail that represents the portion of the winding within the core window area, are representative for the entire MLT of the winding. This allows the reduction of the 3D geometry to a one 2D geometry detail, as shown in **Fig. 4.3(b)**.

- There exists only y-axis H field component within the aforementioned 2D geometry detail of the windings. This is of course only true in case that the heights of the foil windings are the same as the core window height, as shown in **Fig. 4.3(b)**. This assumption allows for the analytic solution of the 2D fields.

While these assumptions are practically almost never fully true, they still allow a relatively good representation of the system for the most frequent winding structures and applications (e.g. low voltage applications).

Given the ideal 2D geometry detail, as displayed in **Fig. 4.3(b)**, the electromagnetic fields within the representative copper foil layer, as given in **Fig. 4.3(c)**, can be expressed as

$$H_y = H_{y.ext}\frac{\sinh(\alpha x)}{\sinh\left(\alpha d_{eq}\right)} - H_{y.int}\frac{\sinh\left(\alpha(x - d_{eq})\right)}{\sinh\left(\alpha d_{eq}\right)} \tag{4.9}$$

$$J_z = \alpha H_{y.ext}\frac{\cosh(\alpha x)}{\sinh\left(\alpha d_{eq}\right)} - \alpha H_{y.int}\frac{\cosh\left(\alpha(x - d_{eq})\right)}{\sinh\left(\alpha d_{eq}\right)} \tag{4.10}$$

where α is the propagation constant

$$\alpha = \frac{1 + j}{\delta} \tag{4.11}$$

and δ is the skin depth

$$\delta = \sqrt{\frac{1}{\pi \mu_0 \sigma f}} \tag{4.12}$$

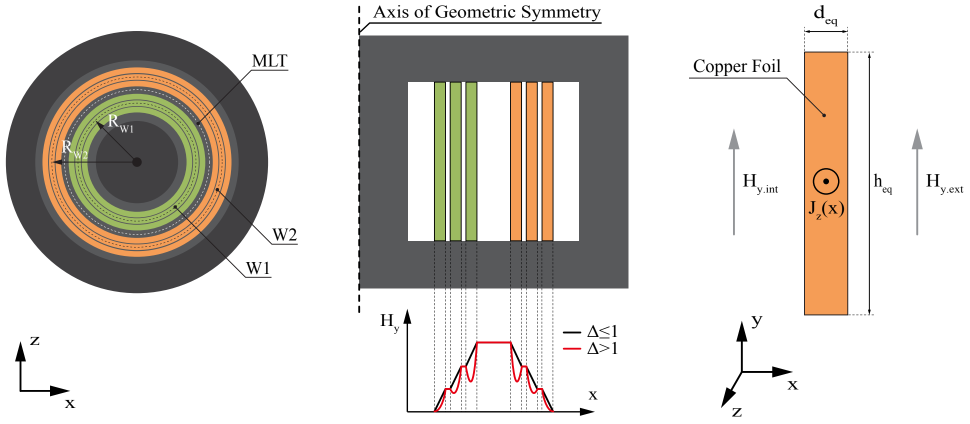

(a) (b) (c)

Fig. 4.3 (a) Ideal, axially symmetrical MFT. (b) Ideal foil winding - filling the entire height of the core window area. (c) A single foil conductor within a core window with corresponding ideal magnetic (*H*) and current density (*J*) fields.

where σ is the conductivity and μ is the permeability of the conductor material. The boundary magnetic field conditions from internal ($H_{y.int}$) and external ($H_{y.ext}$) side of the given (k-th) foil winding layer can be expressed as

$$H_{y.int} = (k-1)\frac{I}{h_{eq}} \tag{4.13}$$

$$H_{y.ext} = k\frac{I}{h_{eq}} \tag{4.14}$$

where I is the transformer input current.

The total per-length Ohmic loses within the k-th foil winding layer are obtained by means of integration of the corresponding loss density within the conductor surface of the foil layer

$$P'_{k.\sigma} = \frac{1}{\sigma}\int JJ^{*}\,dv. \tag{4.15}$$

After some algebraic developments in complex domain, this leads to

$$P'_{k.\sigma} = \frac{H_w}{2\delta\sigma}\left[(H_{y.ext} - H_{y.int})^2\varsigma_1 + 2H_{y.ext}H_{y.int}\varsigma_2\right]. \tag{4.16}$$

where skin and proximity factors are defined with (4.17) and (4.18), respectively

$$\varsigma_1 = \frac{\sinh(2\Delta) + \sin(2\Delta)}{\cosh(2\Delta) - \cos(2\Delta)} \tag{4.17}$$

$$\varsigma_2 = \frac{\sinh(\Delta) - \sin(\Delta)}{\cosh(\Delta) + \cos(\Delta)} \tag{4.18}$$

and the penetration ratio (Δ) is defined as

$$\Delta = \frac{d_{eq}}{\delta}. \tag{4.19}$$

Substitution of (4.13) and (4.14) in (4.16) and a simple summation over the full number of winding layers (1 to m) leads to the total winding per-length Ohmic loss expression

$$P'_{wi.\sigma} = I^2\frac{1}{\delta\sigma H_w}m\left[\varsigma_1 + \frac{2}{3}(m^2-1)\varsigma_2\right]. \tag{4.20}$$

Finally, the total conduction losses of i-th winding can be calculated based on its equivalent mean length turn (MLT_{wi})

$$P_{wi.\sigma} = (MLT_{wi})P'_{wi.\sigma}. \tag{4.21}$$

Note that in case the winding widths (d_{wi}) are non-negligible compared to their equivalent radius (R_{wi}), a more accurate expression can be obtained by direct summation of the product of the conduction losses of each winding layer $P'_{k.\sigma}$ from (4.16) and its corresponding ($MLT_{wi.k}$)

$$P_{wi.\sigma} = \sum_{k=1}^{m}(MLT_{wi.k})P'_{k.\sigma}. \tag{4.22}$$

While these expressions are fully mathematically true only for the ideal foil winding transformers, fulfilling the aforementioned assumptions, as given in **Fig. 4.3**, its validity range can be extend to other winding geometries by means of transformation, as displayed in **Fig. 4.4**.

4.3.3 Practical Application of Dowell's Model

As an illustrative example, in case of a square Litz-wire winding such as shown in **Fig. 4.4(a)**, the circular strands can be substituted with square strands, as shown in **Fig. 4.4(b)** with equivalent width according to (4.23).

$$d_{eq} = d\sqrt{\frac{\pi}{4}} \tag{4.23}$$

According to Dowell, the winding with square strands from **Fig. 4.4(b)** can further be transformed into an equivalent foil winding whose width is equal to the equivalent square strand width and whose height is the same as the height of the core window area, as shown in **Fig. 4.4(c)**. This last equivalence changes the winding copper cross section area and an equivalent porosity factor must be taken into account to ensure the same overall winding DC conductivity according to (4.24).

$$\sigma' = \sigma\eta \tag{4.24}$$

where the porosity factor is calculated as given in (4.25).

$$\eta = \frac{N_{sv} d_{eq}}{H_w} \tag{4.25}$$

As described in [31], the validity of this correction has been further analyzed and confirmed in [75]–[78].

However, the cross-section of any real litz wire does not form a matrix with perfectly aligned strands, as shown in **Fig. 4.4(a)**. The positioning of the strands is rather chaotic and non-constant along the

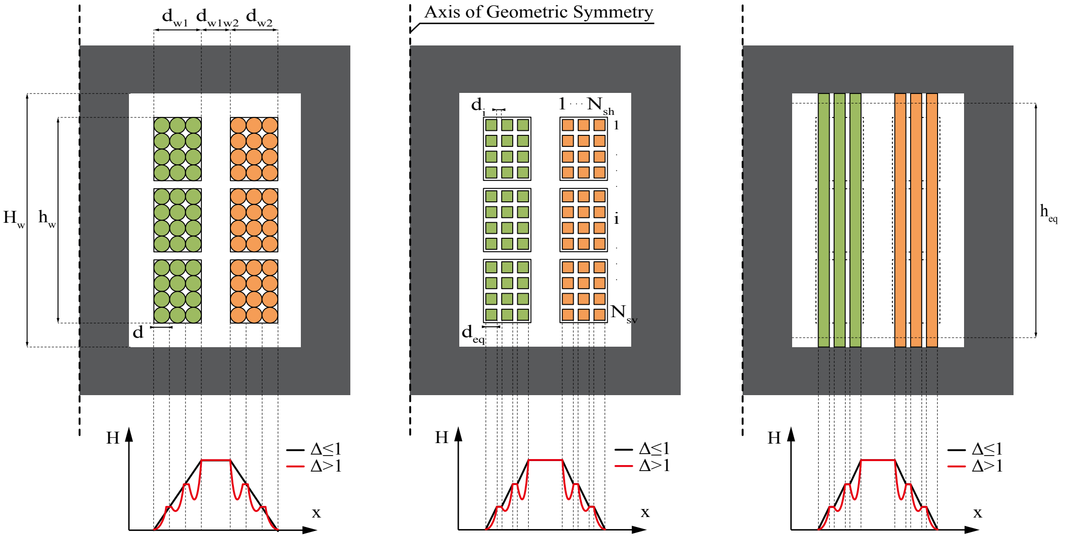

(a) (b) (c)

Fig. 4.4 Winding equivalence for winding losses and leakage inductance estimation with corresponding estimated leakage magnetic field distribution: (a) Original square-profile Litz wire winding, (b) Equivalent square-profile litz wire winding with square strands, (c) Equivalent foil winding.

wire length due to the necessary transpositions and twisting of the Litz strands and groups of strands. This is especially true for square Litz-wires, featuring a high number of very thin strands, as they undergo an additional pressing process in order to shape them into their final rectangular profile.

Therefore, determining the number of litz layers within the windings in horizontal (N_{sh}) and vertical (N_{sv}) direction is not straightforward. However, for the purposes of this model, the equivalent numbers of strands can be generated using an assumption that they have to follow the same geometric proportion as that of the total winding cross-section profile,

$$K_w = \frac{h_w}{d_w}. \tag{4.26}$$

With this assumption, the equivalent numbers of strands of a perfectly aligned and spatially distributed litz wire winding equivalence, as displayed in **Fig. 4.4(a)**, in horizontal and vertical direction, can be calculated as shown in (4.27) and (4.28), respectively.

$$N_{sh} = \sqrt{\frac{N_s}{K_w}} \tag{4.27}$$

$$N_{sv} = \sqrt{K_w N_s} \tag{4.28}$$

This equivalence provides the necessary parameters of the equivalent foil winding, as given in **Fig. 4.4(c)**, for implementation of Dowell's frequency dependent winding loss model, described by (4.20). Finally, the application of the Dowell's model on the square Litz-wire winding from **Fig. 4.4(a)** boils down to substituting σ with σ' in (4.12) and reevaluating (4.19), (4.17), (4.18) and (4.20) where the number of equivalent foil winding layers (m) is equal to the equivalent numbers of strands in horizontal direction,

$$m = N_{sh}. \tag{4.29}$$

It is intuitively obvious that a similar equivalence can as well be applied to tightly packed solid bar, round Litz or non ideal foil windings, thus covering most of the frequently encountered design alternatives.

This equivalence however neglects some effects that may be significant in certain constructions. As already discussed in **Sec. 2.3.2**, in case of the non-ideal foil windings, where $h_w < H_w$, the H field component in the x-axis (H_x perpendicular to the foil) is non-zero in the vicinity of the foil tips, as illustrated in figure **Fig. 2.4(b)**. Depending on the distance between the foil tips and the core, this may cause significant currents and additional localized losses within the foil conductor tips. According to [73], for small distances, the per-length additional localized losses on the one side of the foil winding can be expressed as

$$P'_{tip.1} = \frac{m d_{eq} H_x^2}{\sigma \delta} \tag{4.30}$$

where d_{eq} is the width of the foil conductor, m is the number of foil conductor layers within the winding and H_x can be calculated as

$$H_x = \frac{I(H_w - h_w)}{2d_{eq}H_w} \tag{4.31}$$

where, I is the transformer excitation current. It is interesting to mention that these additional losses can be significantly diminished by interleaving, effectively decreasing m in (4.30), if the requirements for insulation and parasitic capacitance coupling between the primary and secondary winding allow it.

Note that these additional losses can be neglected in case of the Litz wire winding construction where the winding has the isotropic eddy-current-mitigating properties irrespective of the direction of the resulting H field vector within xy-plane. Since the amplitude of H_x is usually orders of magnitude smaller than H_y, this effect can be neglected in most cases.

Finally, besides the described modeling framework, in case of sparse round solid or Litz wire windings where the local H field distribution is significantly influenced, the expressions based on the orthogonality of skin and proximity effects proposed in [75] and [79], [80], respectively, may yield a more accurate estimation of the conductive losses.

4.4 Leakage Inductance Modelling

Accurate design of the MFT leakage inductance is important for the proper converter operation. Especially, when it comes to SRC based topologies, the transformer is a part of the resonant circuit, thus governing the resonant tank frequency with its leakage inductance.

4.4.1 Literature Review

Most of the effort focused on analytical modeling of the leakage inductance documented in the literature is based on the integration of the magnetic energy resulting from the leakage magnetic field within the core window area [31], [42], [70] according to (4.32).

$$W_m = \frac{L_\sigma I^2}{2} = \frac{1}{2}\mu_0 \int_V |H|^2 dV \tag{4.32}$$

Most of this work resides on an assumption that the effect of the radial magnetic field on the energy density within the window area and therefore the leakage inductance is negligible. In other words, the magnetic field within the window area is assumed only to have the axial component. This is a sufficiently accurate approximation for most of the simple winding constructions such as one shown in **Fig. 4.4(a)**. The traditional analytical leakage estimation techniques developed for LFTs [70] mostly focus on capturing the winding geometry effect on the leakage. On the other hand, in case of power electronic aplications, the operating frequencies are typically high and therefore the effect of the frequency on the leakage inductance has to be accurately modeled as well. The majority of the developed frequency dependent leakage models that can be found in the literature [31], [42], [73] are based on the Dowell's frequency dependent leakage inductance model for foil windings [74] and its generalization via the porosity factor, as described in **Sec. 4.3.3**.

4.4.2 Dowell's Model

Employing the same assumptions as for Dowell's frequency dependent core losses derivation described in **Sec. 4.3.2**, the frequency dependent leakage modeling starts with the integration of the total magnetic energy within the core window area, as given in (4.32). Assuming the infinite permeability of the core ferromagnetic material ($\mu \gg \mu_0$), the H field and the resulting magnetic energy W are concentrated only within the core window area - winding conductors and the surrounding dielectric. Considering the ideal dielectric properties of the insulation material, the H field and corresponding magnetic energy W distribution outside of the winding conductors is frequency independent. On the other hand, depending on the frequency and electric properties (e.g. σ), the magnetic energy will be inhibited within the volume of the winding conductors due to the induced eddy currents - skin and proximity effects. Consequently, the total leakage inductance will consist of two parts - frequency independent and dependent part.

Obtaining the H field density distribution outside of the winding conductors is relatively trivial under the given assumptions. According to the ideal foil winding transformer, as given in **Fig. 4.3(b)**, the magnetic energy exists within the winding inter-layer and inter-winding dielectric spacings. Taking into account that the $H_{y.ext}$ field is constant within each of the $(m-1)$ inter-layer spacings of the winding, their total per-length magnetic energy contribution can be expressed as their sum

$$W'_{wi} = \frac{1}{2}\mu_0 \sum_{k=1}^{m-1} \int_0^{d_i} H_{y.ext}^2(k) H_w dx = \mu_0 \frac{I^2}{2H_w} d_i \sum_{k=1}^{m-1} k^2 \tag{4.33}$$

where d_i and $H_{y.ext}$ are the inter-layer spacing and magnetic field according to (4.14), respectively. Applying the closed form solution for the above quadratic sum yields

$$W'_{wi} = \mu_0 \frac{(mI)^2}{2H_w} d_i \frac{(m-1)(2m-1)}{6m}. \tag{4.34}$$

In a similar fashion, taking into account that the $H_{y.ext}$ field is constant within the inter-winding spacing, its total per-length magnetic energy contribution can be expressed as

$$W'_{w1w2} = \frac{1}{2}\mu_0 \int_0^{d_{w1w2}} H_{y.ext}^2(m) H_w dx = \mu_0 \frac{(mI)^2}{2H_w} d_{w1w2} \tag{4.35}$$

where d_{w1w2} is the inter winding dielectric spacing. The frequency independent part of the magnetic energy is expressed in closed form with (4.34) and (4.35).

On the other hand, obtaining the H field density distribution inside of the winding conductors is not so straight forward. Substitution of (4.9) in (4.32) and some algebraic developments in complex domain lead to the total per length magnetic field energy within k-th winding layer

$$W'_{wc.k} = \mu_0 \frac{H_w \delta}{4} \left[(H_{y.ext} + H_{y.int})^2 \varphi_1 - 2H_{y.ext} H_{y.int} \varphi_2 \right]. \tag{4.36}$$

where

$$\varphi_1 = \frac{\sinh(2\Delta) - \sin(2\Delta)}{\cosh(2\Delta) - \cos(2\Delta)} \tag{4.37}$$

and

$$\varphi_2 = \frac{\sinh(\Delta) - \sin(\Delta)}{\cosh(\Delta) - \cos(\Delta)}. \tag{4.38}$$

The substitution of (4.13) and (4.14) in (4.36) and summation of the magnetic energy within all of the m winding layers leads to an expression for frequency-dependent per-length magnetic energy within the winding conductors.

$$W'_{wc} = \mu_0 \frac{(mI)^2}{2H_w} \frac{md_{eq}}{3} \frac{1}{2m^2\Delta} \left[(4m^2 - 1)\varphi_1 - 2(m^2 - 1)\varphi_2\right]. \tag{4.39}$$

The substitution of (4.34), (4.35) and (4.39) into (4.32) results in a closed form analytical expression for the full per-length frequency-dependent leakage inductance estimation referred to the primary side

$$\begin{aligned} L'_\sigma = N_1^2 \mu_0 \frac{1}{H_w} \Bigg[& \underbrace{\frac{d_{w1eq} m_{w1}}{3} F_{w1} + \frac{d_{w2eq} m_{w2}}{3} F_{w2}}_{\substack{\text{Frequency dependent portion due to the magnetic} \\ \text{energy within the copper volume of the windings}}} \\ + & \underbrace{d_d}_{\substack{\text{Portion due to magnetic energy within} \\ \text{the inter-winding dielectric volume}}} \\ + & \underbrace{d_{w1i} \frac{(m_{w1} - 1)(2m_{w1} - 1)}{6m_{w1}}}_{\substack{\text{Portion due to magnetic energy within the} \\ \text{inter-layer dielectric of the primary winding}}} \\ + & \underbrace{d_{w2i} \frac{(m_{w2} - 1)(2m_{w2} - 1)}{6m_{w2}}}_{\substack{\text{Portion due to magnetic energy within the} \\ \text{inter-layer dielectric of the secondary winding}}} \Bigg] \end{aligned} \tag{4.40}$$

The frequency dependent portion of the leakage magnetic field, within the copper volume of the primary and secondary winding, is taken into account via Dowell's frequency dependent factor

$$F_w = \frac{1}{2m^2\Delta} \left[(4m^2 - 1)\varphi_1 - 2(m^2 - 1)\varphi_2\right] \tag{4.41}$$

Finally, the total leakage inductance is obtained by multiplication of the per-length value with the equivalent inter-winding MLT

$$L_\sigma = (MLT) L'_\sigma. \tag{4.42}$$

Note that, similar to the winding losses calculation, of course a more accurate expression is obtained by multiplying each of the energies within different layers with their corresponding mean length turns. However, for the sake of simplicity this reduced expression is used for the analysis.

4.4.3 Practical Application of the Dowell's Model

The same transformation procedure and winding equivalence can be used, as described in detail in **Sec. 4.3.3**. The only missing parameters of the equivalent foil windings required in (4.40) are the inter layer dielectric spacings d_i. Based on the equivalent number of strands in the horizontal direction (N_{sh}) and the geometric width of the winding (d_w) and the equivalent strand conductor width (d_{eq}), as given in **Fig. 4.4**, (4.27) and (4.23), these can be calculated as

$$d_i = \frac{d_w - N_{sh} d_{eq}}{N_{sh} - 1}. \tag{4.43}$$

This, together with the equivalent parameters derived in **Sec. 4.3.3**, fully defines the equivalent foil winding for the implementation of the Dowell's frequency dependent leakage inductance model, as given in (4.40).

From the applicability point of view, the same conclusions hold, as discussed in **Sec. 4.3.3**. However, depending on the actual geometry, as a result of the winding transformation, as shown in **Fig. 4.4**, the height of the equivalent foil winding (H_w) may be radically higher compared to the original (h_w). While h_w/H_w ratio is close to one in LV applications, the dielectric distances necessary to facilitate MV insulation may yield much lower h_w/H_w, resulting in a significant change relative to the initial geometry.

Historically speaking, high frequency semiconductors have first been developed for low powers and low voltages. On the other hand, this type of complex frequency dependent leakage inductance model is not needed for line frequency transformers operating at $50/60Hz$. Therefore, it found its use in low-power low voltage applications where the transformer window utilization is very high and these assumptions are therefore reasonably close to reality. However, this is not necessarily the case when it comes to the aimed high-power MV applications, enabled by the contemporary high-power semiconductors.

4.4.4 FEM Analysis

To test the validity of the Dowell's equivalence and the accuracy of the estimation, magnetostatic 2D FEM simulations are performed on a typical transformer cross-section geometry as a DC boundary condition, as displayed in **Fig. 4.5**. As the only parameter that changes with this equivalence is the winding height (h_w) or, in other words, the proportion between the winding height and core window height (h_w/H_w), a parametric sweep is performed, varying the winding height in range from 40% to 100% of the core window height. These results are compared with the leakage inductance estimation of the Dowell's model at zero frequency (DC) and shown in **Fig. 4.6**.

One can notice that the estimation error increases substantially with the decrease of the mentioned proportion. This result is intuitively clear as the change of the geometry introduced by Dowell's equivalence is higher as the proportion of the winding height compared to core window height is smaller. Thus, the estimation of Dowell's model has a reasonable accuracy only for geometries where the winding to core window height proportion is close to 100%.

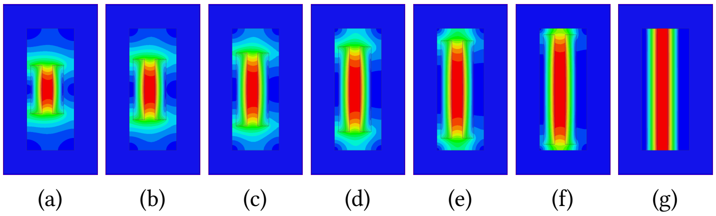

Fig. 4.5 2D magnetostatic FEM simulations of the H field within the cross-section of the core window area for different winding heights in range from 40% (a) to 100% (g) of core window height, illustrating spacing requirements due to insulation coordination.

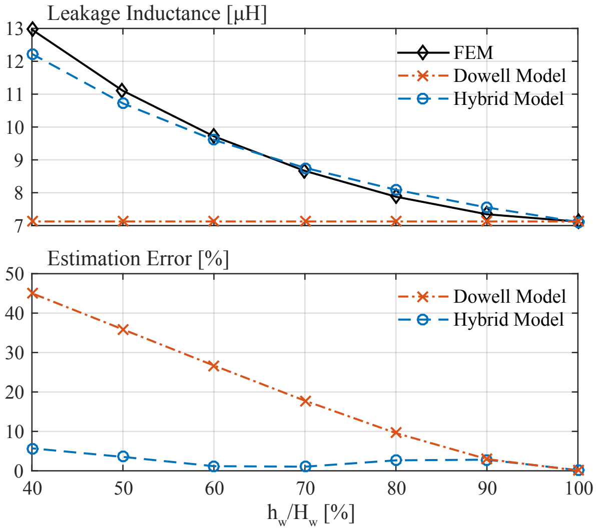

Fig. 4.6 Top plot: Magnetostatic FEM simulation leakage inductance estimation (black), estimation with hybrid model at zero frequency (blue dashed line), estimation with Dowell model at zero frequency (red dash-dot line). Bottom plot: DC leakage inductance estimation error of the Hybrid (blue dashed line) and Dowell (red dash-dot line) model, referred to the FEM results.

4.4.5 Hybrid Leakage Inductance Model

In traditional LFT design, the effect of winding geometry on the transformer leakage inductance is taken into account via a correction factor, Rogowski factor [70], that takes into account the uneven geometric magnetic field distribution by correcting the equivalent length (winding height) of the magnetic flux path through the air.

The main idea of the proposed hybrid model is to use this corrected equivalent magnetic field path length for winding equivalence in Dowell's frequency dependent model instead of the total core window height, thus including the geometry implications into the described framework. This equivalent winding height can be calculated from the original winding height as

$$h_{eq} = \frac{h_w}{K_R} \tag{4.44}$$

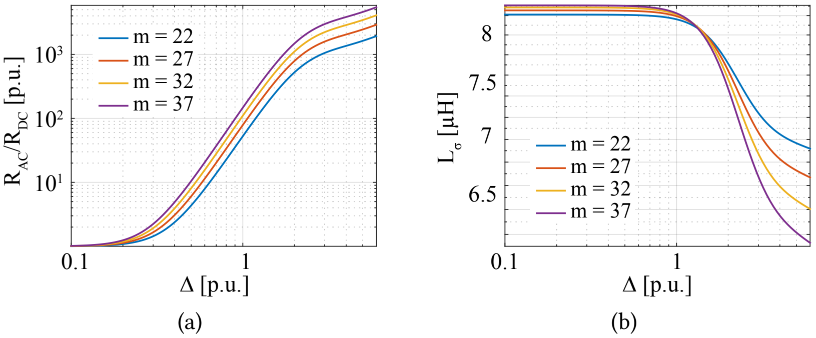

(a) (b)

Fig. 4.7 Plots of the frequency dependency of the AC resistance (a) and leakage inductance (b) of an example square Litz wire winding, as described in **Fig. 4.4** for several different equivalent layer numbers m.

where

$$K_R = 1 - \frac{1 - e^{-\pi h_w/(d_{w1}+d_d+d_{w2})}}{\pi h_w/(d_{w1}+d_d+d_{w2})}. \tag{4.45}$$

The correction of the model is applied by simple substitution of H_w with the equivalent height h_{eq} from (4.44) in (4.24) and (4.40), thus generating a hybrid leakage inductance model that accurately captures both the frequency and geometry effects.

The leakage inductance estimations of the developed hybrid model, for various winding to core window height ratios (h_{eq}/H_w) at zero frequency (DC), are compared with the FEM simulations and Dowell's model in **Fig. 4.6**. It can be seen that the hybrid model estimation is very well correlated with FEM simulation results, with maximum relative error within 6% in the entire given geometric proportion range, from 40% to 100%. These results confirm the capability of the developed model to accurately account for the effect of the MFT geometry in a much wider range compared to original Dowell's model.

Plots of the frequency dependency of the series AC resistance and leakage inductance of an example square Litz wire winding, as shown in **Fig. 4.4**, are displayed in **Fig. 4.7**. It can be seen that m influences the critical penetration Δ ratio where R_{AC} starts to increase significantly. On the other hand this is not the case with the leakage inductance, where the critical Δ practically remains the same irrespective of m. Moreover, it can be seen that for a typical Litz wire winding, where equivalent m is typically high, the critical Δ for the R_{AC} is significantly lower (around 0.2 – 0.3) than that of the L_σ (1 – 1.2). In other words, if the transformer is operating within a Δ region where the frequency effect on the leakage inductance is significant (Δ > 1), it would suffer immense resistive losses due to extremely high R_{AC}, up to three orders of magnitude higher than R_{DC}.

Therefore the nominal Δ is usually upper bound in the design procedure by the acceptable winding losses at values much lower than those where the frequency effect on the leakage inductance starts to occur. This result only further emphasizes the importance of the accurate DC leakage inductance estimation, taking properly into account the winding geometry, rather than the frequency influence which is usually never reached in case of good high-efficiency designs.

4.5 Magnetizing Inductance

Similar to the leakage inductance, magnetizing inductance of the MFT plays a major role in the converter operation. Its accurate design is especially important when it comes to SRC based topologies where it is a part of a resonant tank and more importantly dictates the turn-off current of the resonant converter and the resulting switching losses. For the given applications, in SRC and DAB, the air gap is typically very small as the required magnetizing inductance is usually high.

A standard core reluctance model based on a magnetic circuit, as displayed in **Fig. 4.8(a)** can be used to obtain the ideal magnetizing inductance

$$L_m = \frac{\mu_0 N_1^2 A_c}{\dfrac{l_m}{\mu_r} + d_{ag}}. \tag{4.46}$$

As the expected air-gap (d_{ag}) is very small, the effect of the air-gap fringing flux is taken into account via a simple empirical model [49], sufficiently accurate for small air-gaps. This leads to the corrected magnetizing inductance expression

$$L_m' = L_m F_{FR} \tag{4.47}$$

where

$$F_{FR} = 1 + \frac{d_{ag}}{\sqrt{A_c}} ln\left(\frac{2H_w}{d_{ag}}\right) \tag{4.48}$$

is the fringing flux factor. The effects of various core geometry parameters on this factor are shown in **Figs. 4.8(b)** and **4.8(c)**. It can be seen that the relative increase of the core cross-section results in decrease of the fringing flux, whereas the opposite is true for the core window height.

Taking into account the variations of the core characteristics due to the manufacturing imperfections, together with the limited accuracy of the transformer assembly process, implementation of a more accurate and accordingly more complicated model was considered as unnecessary for design optimization.

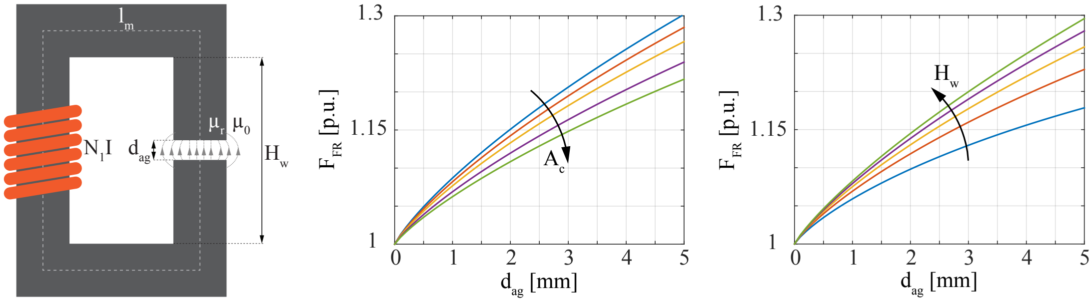

(a) (b) (c)

Fig. 4.8 (a) Simple magnetic circuit for the derivation of the core magnetic reluctance model. (b) Plot of a family of curves showing the influence of the core cross-section (A_c) on the flux fringing factor. (c) Plot of a family of curves showing the influence of the core window height (H_w) on the flux fringing factor.

4.6 Thermal Modeling

A proper thermal coordination is one of the most important tasks from the safety point of view. The reduction of the MFT size, as a result of operation at elevated frequencies, directly affects the cooling conditions due to the decreased cooling surface, as illustrated in **Fig. 4.9**. Decreased cooling surface implies increased thermal resistances towards the ambient (cooling media) which result in higher temperature gradients. Therefore, accurate thermal modeling, that allows for adequate MFT thermal coordination at the design stage, plays an essential role in the search for the overall optimal design [31], [42], [43], [73], [81].

This section provides a detailed FEM thermal analysis and derivation of a comprehensive analytical thermal network model, based on the conduction, convection and radiation thermal resistances, capable of accurately estimating the temperature rise at the hot-spots within the windings and the core in the steady state. Compared to the aforementioned state of the art, the model captures a very detailed picture of the 3D transformer geometry, thus allowing a precise temperature estimation and analysis of various, otherwise non-modeled, effects. Moreover, the thermal network is designed to have a generic structure that can facilitate the modeling of any of the possible MFT constructions (e.g. shell, core, etc.) via simple modification of the corresponding thermal resistances.

4.6.1 Thermal Network Model Based on the 3D Transformer Geometry

Estimation of the MFT hot-spot temperatures is a complex 3D heat transfer problem, as displayed in **Fig. 4.9**, which includes all three types of heat transfer mechanisms: conduction, convection and radiation. However, taking into account the symmetry of the MFT geometry, as illustrated in **Fig. 4.10(a)**, it is possible to reduce the 3D heat transfer model to two 2D geometry details, as shown in **Figs. 4.10(b)** and **4.10(c)**, characterizing the different cooling conditions of the winding portions, inside and outside of the core window.

In addition to this, it is possible to further reduce this model to a single 2D geometry detail, as displayed in **Fig. 4.11(a)** without neglecting the effects of the part of the winding that is outside of the shell core window using an assumption that there is no temperature gradient within the winding

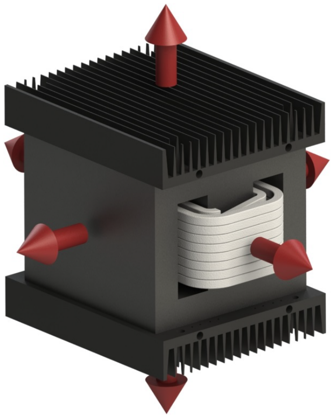

Fig. 4.9 Shell MFT geometry - outer cooling surfaces.

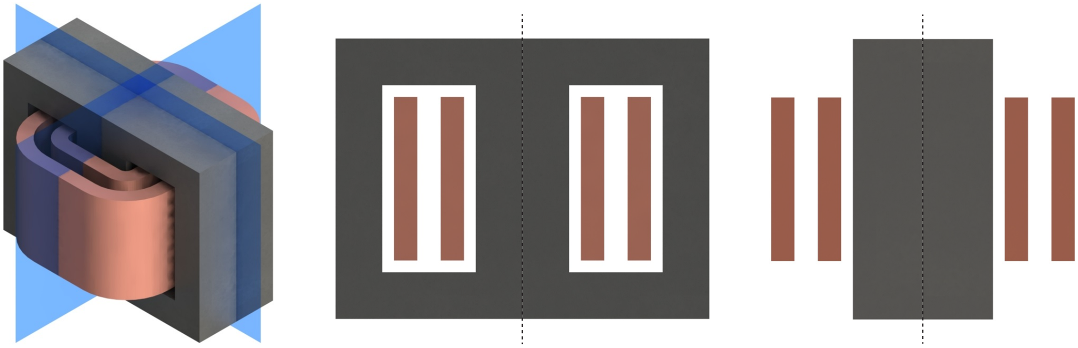
(a) (b) (c)

Fig. 4.10 (a) 3D MFT structure with highlighted thermal planes of symmetry. (b) 2D symmetry detail capturing the geometry within the core window. (c) 2D symmetry detail capturing the geometry outside of the core window.

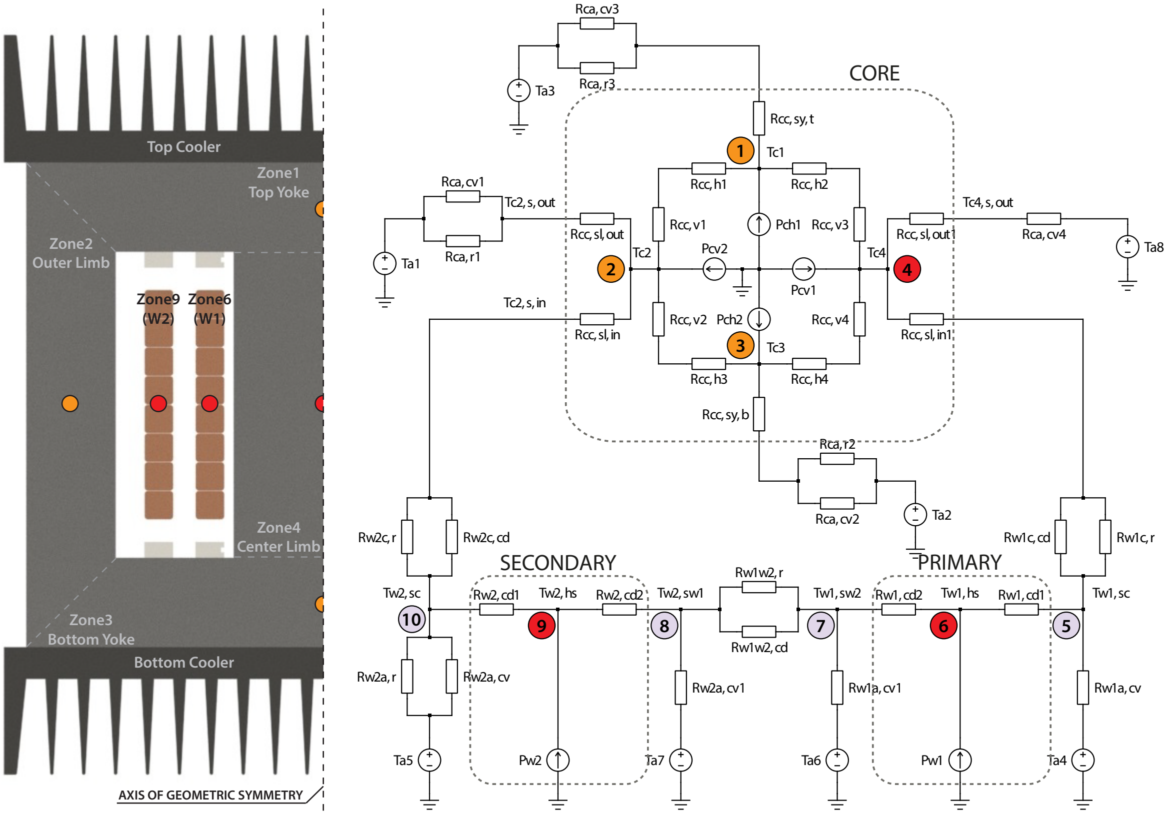

(a) (b)

Fig. 4.11 (a) Partitioning of the MFT into zones for thermal modeling with respect to geometric symmetry. (b) Detailed static thermal network model of the MFT based on conduction, convection and radiation thermal resistances (nodes without heat injection - gray, expected hot-spot nodes for the given design - red).

in the tangential direction of the wire. This is a reasonable assumption which is very close to reality, due to the high temperature conductance of copper compared to the enamel insulation, which allows

Tab. 4.1 Empirical heat-transfer formulas for conduction, convection and radiation [73], [82], [83]

Conduction	$Q_h = kA\frac{\Delta T}{L}$			
Natural Convection over a Hot-Plate	$Q_h = hA(T_s - T_\infty)$	Top:	$h = \frac{k(0.65+0.36R_{a_L}^{1/6})^2}{L}$	$L = \frac{\text{Area}}{\text{Perimeter}}$
		Side:	$h = \frac{k}{L}\left(0.825 + \frac{0.387R_{a_L}^{1/6}}{\left(1+(0.492/P_r)^{9/16}\right)^{8/27}}\right)^2$	$L =$ Height
		Bottom:	$h = \frac{k0.27R_{a_L}^{1/4}}{L}$	$L = \frac{\text{Area}}{\text{Perimeter}}$
Radiation	$Q_h = hA(T_1 - T_2)$		$h = \epsilon\sigma\frac{(T_1+273.15)^4-(T_2+273.15)^4}{(T_1-T_2)}$	

where: R_{a_L} - Rayleigh number, P_r - Prandtl number, ϵ - Emissivity, σ - Stefan–Boltzmann constant

to indirectly include the effect of the different cooling conditions of both winding portions, inside and outside of the core window, on the winding hot-spot temperature in a simple manner, by putting in parallel their corresponding heat transfer resistances.

A detailed thermal network consisting of conduction, convection and radiation thermal resistances, as illustrated in **Fig. 4.11(b)** and described by **Tab. 4.1**, is generated based on the derived 2D representation, shown in **Fig. 4.11(a)**. This 2D MFT geometry detail can be partitioned into different zones with respect to the occurring physical phenomena - heat transfer and distributed heat injection within the core and winding volume caused by the corresponding losses, as described in **Secs. 4.2** and **4.3**, respectively.

The core area is divided into four zones corresponding to the center and outer limb and top and bottom yoke, as illustrated in **Fig. 4.11(a)**. It is assumed that the core losses are evenly distributed within the core volume. Therefore, the injected heat in each core zone is proportional to its volume in respect to the total core losses. Primary and secondary windings are represented with the two corresponding zones. Finally, the thermal network is constructed by taking into account all of the thermal couplings between all of the zones and surrounding air at ambient temperature via conduction, convection and radiation, as shown in **Fig. 4.11(b)** and **Tab. 4.1**.

The admittance matrix of this network is derived and used for efficient calculation of the temperatures at all nodes, according to the injected power of losses in the windings and the core. For the given network, as displayed in **Fig. 4.11(b)**, the calculation of the temperatures in all nodes corresponds to the inversion of a (10x10) matrix

$$\mathbf{Q}_{(n)} = \mathbf{Y}_{th_{(n_x n)}} \Delta\mathbf{T}_{(n)} \tag{4.49}$$

where **Q** is a vector of the injected power of losses in all nodes, $\mathbf{Y}_{th_{(n_x n)}}$ is a full admittance matrix of the thermal network and $\Delta\mathbf{T}_{(n)}$ is a vector of the temperature increase in respect to the ambient of all nodes.

Even though this operation requires a relatively low computational effort, when it comes to optimization, as will be presented in **Chap. 6**, with polynomial complexity, decreasing the weight of the function primitives, containing the models, becomes paramount in order to enable the largest possible set of design variables and design range with reasonable discretization. In that respect, it is possible to rearrange the set of thermal equations displayed in (4.49), by bisecting the set of nodes to those that have non-zero heat power injection (A index) and those that have zero heat power injection (B index), as shown in (4.50).

$$\begin{bmatrix} \mathbf{Q}_{A_{(m)}} \\ \mathbf{0}_{(p)} \end{bmatrix} = \begin{bmatrix} \mathbf{Y}_{thAA_{(m_xm)}} & \mathbf{Y}_{thAB_{(m_xp)}} \\ \mathbf{Y}_{thBA_{(p_xm)}} & \mathbf{Y}_{thBB_{(p_xp)}} \end{bmatrix} \begin{bmatrix} \Delta\mathbf{T}_{A_{(m)}} \\ \Delta\mathbf{T}_{B_{(p)}} \end{bmatrix} \tag{4.50}$$

It is possible to apply the Kron reduction [84] to (4.50), as shown in (4.51), thus reducing the matrix dimension to the number of nodes with heat injection. The result of this reduction is a reduced size Kron matrix, as given in (4.51), which allows the calculation of temperatures at the expected hot-spot points (e.g. center of the windings and cores) according to the injected power of losses in the windings and the core.

$$\Delta\mathbf{T}_{A_{(m)}} = \left(\mathbf{Y}_{thAA_{(m_xm)}} - \mathbf{Y}_{thAB_{(m_xp)}}\mathbf{Y}^{-1}_{thBB_{(p_xp)}}\mathbf{Y}_{thBA_{(p_xm)}}\right)^{-1}\mathbf{Q}_{A_{(m)}} = \mathbf{Y}^{-1}_{Kron_{(m_xm)}}\mathbf{Q}_{A_{(m)}} \tag{4.51}$$

4.6.2 Thermal FEM Analysis

A detailed 2D and 3D FEM analysis is performed on the realized MFT prototype geometry, as will be described in **Chap. 7**, in order to verify the validity of the assumptions made while deriving the analytical model and its hot-spot temperature estimations, as shown in **Fig. 4.12**. The FEM and derived analytical thermal-network model hot-spot temperature estimations within the core and windings are summarized in **Tab. 4.2**. The two 2D simulations, displayed in **Figs. 4.12(a)** and **4.12(b)**, show the impact of the different cooling conditions on the temperature distribution and hot-spot magnitude of the two cross-section details with windings outside and inside of the core window area, respectively. The results of the full MFT 3D simulation, taking into account the anisotropic thermal conductance of the windings (Litz wire), are illustrated in **Fig. 4.12(c)**.

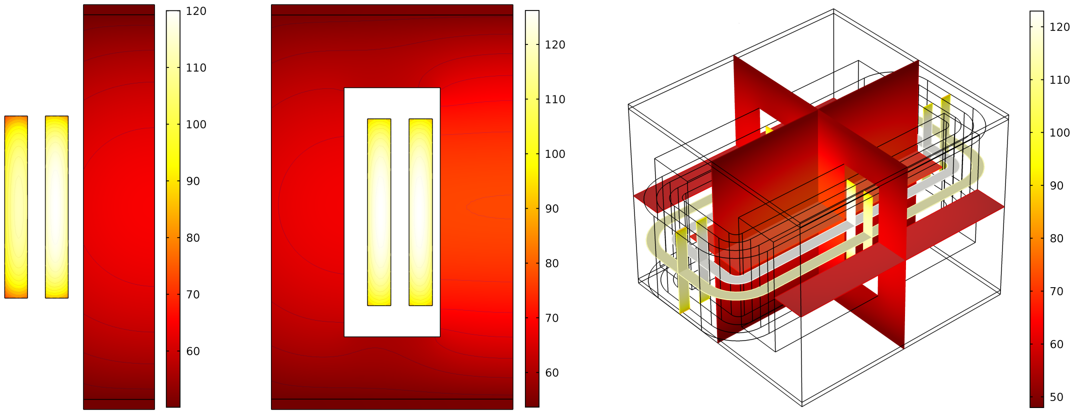

(a) (b) (c)

Fig. 4.12 Thermal FEM analysis of the MFT: (a) 2D symmetry detail outside of the window area, (b) 2D symmetry detail inside of the window area, (c) Full 3D model.

Tab. 4.2 Hot-spot temperature estimations

Hot-spot nodes	T_4 [°C]	T_6 [°C]	T_9 [°C]
FEM 2D detail 1	70	120	106
FEM 3D detail 2	76	127	125
FEM 3D full	75	122	113
Analytical	73.75	124.6	116.3

Despite the obvious maximum hot-spot temperature difference between the two 2D symmetry details, due to the very high relative thermal conductivity of the Litz wire along its path (through copper) compared to the radial direction (through layers of copper and enamel coating, three orders of magnitude less than pure copper), the temperature distribution along the winding turn path is practically constant in the 3D simulation and the hot-spot magnitude is between the two 2D extreme values. This result confirms the validity of the assumption that both cooling conditions, inside and outside of the core window area, can be taken into account analytically by putting their corresponding thermal resistances in parallel.

Finally, as can be seen in **Tab. 4.2**, the analytically calculated hot-spot temperatures of the core and two windings ($74^\circ C$, $125^\circ C$ and 116, respectivelly) are very well correlated with the full 3D MFT model FEM simulation results, as given in **Fig. 4.12(c)**.

It is important to mention that the proposed generic thermal network structure facilitates the direct application of the developed methodology to any other different MFT design by simple adjustment of the appropriate thermal coupling resistances. For example, in case of a cooler attached to the top and bottom of the core, $R_{cc.h1}$, $R_{cc.h2}$, $R_{cc.h3}$, $R_{cc.h4}$, as given in **Fig. 4.11(b)**, can be set to zero. Due to the thick aluminum plate of the cooler with very high thermal conductivity, it can be assumed that the temperature is constant within the entire top and bottom yoke. In case the inner or outer surface of the primary winding has no access to the surrounding fluid, the corresponding convection thermal resistance, $R_{w1.cd1}$ or $R_{w1.cd2}$, respectively, should be set to infinite. In this fashion, any construction type and design choice combination can be taken into account.

With the described generic thermal network and its admittance matrix representation, a sufficiently accurate and detailed thermal model is constructed, with acceptable computational cost for design optimization purposes.

4.7 Conclusion

Appropriate MFT modeling for design optimization is not straightforward. Besides the accuracy requirements, facilitating any optimization scheme implies hard constraints in terms of computational cost, thus in general excluding the possibility of direct application of very sophisticated numeric tools such as FEM. That is where the light weight analytical models perform extremely well as long as the necessary approximations/assumptions hold within reasonable accuracy limits. Finally, while these models can solve a significant part of the problem, still many phenomena cannot be described sufficiently accurate in that way.

5

Statistical Data-Driven Modeling

This chapter proposes a new class of neural-network inspired data-driven models, especially derived for design optimization purposes. These models allow for an efficient (3 – 5 orders of magnitude faster compared to FEM), yet sufficiently accurate (within 5 – 10% error relative to FEM) and numerically stable estimation of the complex effects, with otherwise impractically high computational cost and/or convergence issues.

5.1 Introduction

While it is the best when a certain model has an analytical closed form solution, there are still problems that cannot be analytically approximated within reasonable accuracy limits, as shown in **Fig. 5.1(a)**. In these cases FEM is normally used. In general, due to high computational cost and problems with numeric stability, these models are usually used for final design verification and its correction through several last iterations outside of the main design optimization loop. A new class of models is proposed in this chapter, FEM based statistical data driven models (SDDM), inherently featuring the high precision of FEM (within < 5% error compared to FEM) yet with execution speed comparable to analytic models (3 – 5 orders of magnitude faster than FEM), as displayed in **Fig. 5.1(b)**. With this type of modeling framework it is now possible to include very complex and sophisticated

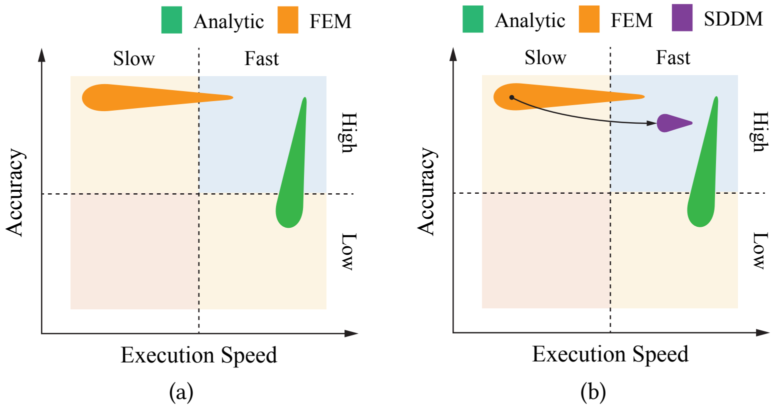

Fig. 5.1 Qualitative analysis of the properties of various classes of models: (a) Analytic and FEM; (b) Inclusion of the proposed FEM-based statistical data-driven models (SDDM) allows modeling complex phenomena with inherent accuracy almost as good as FEM (within < 5% error) yet with execution speed comparable to analytic models (3 – 5 orders of magnitude faster than FEM).

simulations, otherwise impractically slow or numerically unstable, into the main optimization loop.

Inspired by neural networks, this methodology uses regression to train the models based on the results of the extensive FEM simulations of the representative generalized geometry details. Models are expressed as multi-variable polynomials, providing a powerful generalized modeling format for a wide spectrum of phenomena with low computational cost.

For the sake of illustration, the approach can be compared to early analytical empirical models, such as Steinmetz equation and many others, with the two key differences: (i) The format of the model is standardized, yet very flexible thus providing a very efficient modeling framework that is applicable to a very wide range of models. (ii) The data gathering cost is very low. Relevant data can be obtained through excessive FEM simulations, verified with only a few experimental results, in contrast to series of real experiments.

Three application examples of the proposed SDDM modeling framework, on the phenomena that cannot be properly analytically modeled, are provided in the following.

5.2 Leakage Inductance Modelling Of Asymmetric Winding Structures

As discussed in **Sec. 4.4**, a proper design of the MFT electric parameters, especially the MFT leakage inductance, is important for the proper converter operation. This section describes the technical challenges of the leakage inductance estimation of the asymmetric multi-winding MFTs for design optimization purposes.

While it is possible to quite accurately model the leakage inductance of the typical symmetric 2-winding transformer geometries, using light-weight analytical models, as described in **Sec. 4.4**, in

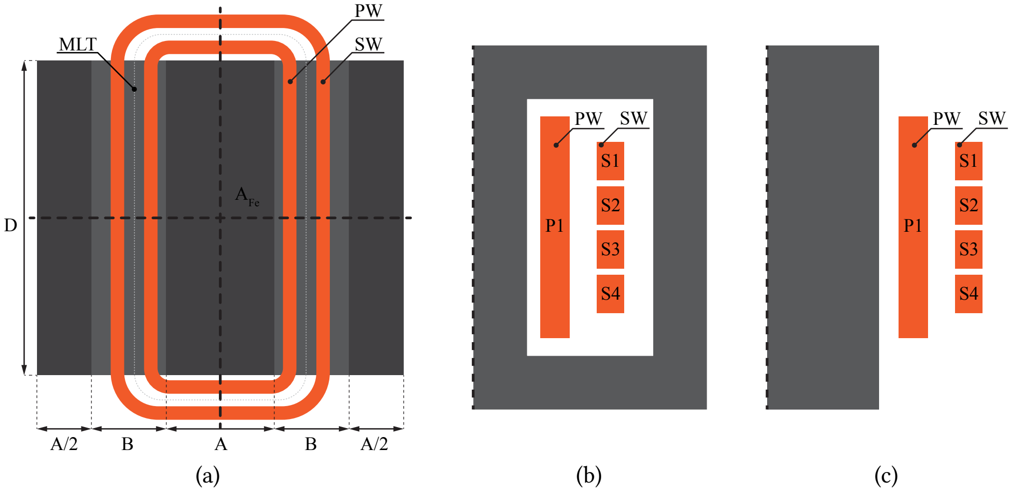

(a) (b) (c)

Fig. 5.2 Considered multi-winding transformer with asymmetric winding structure. (a) Horizontal cross-section showing two axis of MFT geometric symmetry. MFT geometric symmetry detail inside (b) and outside (c) of the core window area.

case of frequently encountered asymmetric multi-winding structures [47], [85], such as shown in **Fig. 5.2**, all of the available methods (e.g. FEM, Roth [86] etc.) resort to some type of computationally intensive numeric techniques. These methods offer a good accuracy, but their execution time and numeric stability are often limiting factors when it comes to overall multi-variable optimization. To that end, this section proposes a computationally efficient leakage inductance model for multi-winding transformers, developed to yield very fast execution.

This section proposes a computationally efficient model that allows for a very fast DC leakage inductance estimation of multi-winding transformers. It is based on multi-variable polynomial fitting of the results of the FEM analysis generated on the two representative generalized winding geometry primitives, as given in **Fig. 5.3**. Thus the proposed model keeps the inherent precision of the FEM as the most precise modeling approach, whereas its execution boils down to several low order matrix multiplications, as one of the most primitive computation functions, resulting in very fast execution.

5.2.1 Proposed Modeling Method

The first phase of modeling is the magnetostatic FEM analysis, allowing to identify the effect of various geometric parameters on the transformer DC leakage inductance. As shown in [87], the total (3D) leakage inductance of the transformer can be very well estimated using two 2D models, representing the magnetic field energy inside and outside of the core widow area, as depicted in **Fig. 5.2**. Therefore, the estimation of the total (3D) leakage, boils down to the ability to accurately estimate the magnetic energy in these two 2D geometries.

The two representative 2D generalized geometry primitives are defined and parametrised, as described in **Fig. 5.3**, and normalized, as shown in **Tabs. 5.1** and **5.2**. As can be seen, they are fully defined with eight and seven normalized parameters, respectively. Due to the largely linear effect on the leakage inductance, relative winding widths can be considered as constant. Based on the preservation of the total magnetic energy (S_W), a winding geometry equivalence with infinitely thin windings can

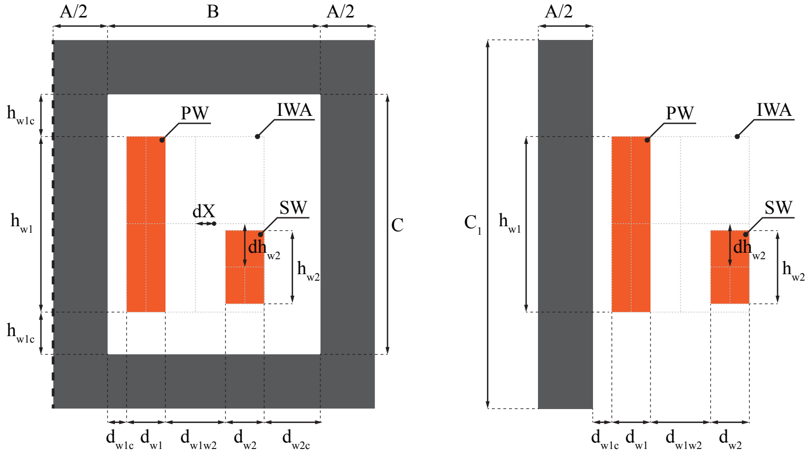

(a) (b)

Fig. 5.3 Two generalized geometry details describing the magnetic energy of the winding cross-section inside (a) and outside (b) of the core window area.

Tab. 5.1 Definition of the normalized variables based on the generalized winding geometry detail, as shown in **Fig. 5.3(a)**

Variable	/	/	x_1	x_2	x_3	x_4	x_5	x_6
Definition	$\frac{d_{w1}}{h_{w1}}$	$\frac{d_{w2}}{h_{w1}}$	$\frac{d_{w1w2}}{h_{w1}}$	$\frac{h_{w2}}{h_{w1}}$	$\frac{2dh_{w2}}{h_{w1}-h_{w2}}$	$\frac{B}{d_{w1}+d_{w1w2}+d_{w2}}$	$\frac{C}{h_{w1}}$	$\frac{2dX}{B-d_{w1}-d_{w1w2}-d_{w2}}$
Range	0.1	0.1	0 – 0.7	0.2 – 1	0 – 1	1 – 2	1 – 2	−1 – 1

Note that h_{w1} is taken as a reference when defining the geometry ratios. Winding widths (d_{w1} and d_{w2}) are fixed as their effect on the leakage is quite linear and can be taken into account through a correction of d_{w1w2}.

Tab. 5.2 Definition of the normalized variables based on the generalized winding geometry detail, as shown in **Fig. 5.3(b)**

Variable	/	/	x_1	x_2	x_3	x_4	x_5
Definition	$\frac{d_{w1}}{h_{w1}}$	$\frac{d_{w2}}{h_{w1}}$	$\frac{d_{w1w2}}{h_{w1}}$	$\frac{h_{w2}}{h_{w1}}$	$\frac{2dh_{w2}}{h_{w1}-h_{w2}}$	$\frac{d_{w1c}}{d_{w1}+d_{w1w2}+d_{w2}}$	$\frac{C}{h_{w1}}$
Range	0.1	0.1	0 – 0.7	0.2 – 1	0 – 1	0 – 1	1 – 2

Note that compared to the geometry detail inside the core window area (**Fig. 5.3(a)**), the leakage inductance is in this case fully defined by five normalized variables. Instead of x_4 and x_6 from **Tab. 5.1**, it is enough to define x_4 as given in **Tab. 5.2**.

be derived, as given in **Fig. 5.4**. The effect of the winding (d_{w1} and d_{w2}) and inter-winding (d_{w1w2}) widths on the leakage inductance can be merged into an equivalent inter-winding distance (5.1).

$$d_{w1w2.eq} = d_{w1w2} + \frac{1}{3}(d_{w1} + d_{w2}) \tag{5.1}$$

Using this equivalence, any winding width configuration can be transformed into any other, while preserving the total magnetic energy and consequently the resulting leakage inductance. Of course, in case of the discussed asymmetric winding arrangement, this equivalence is an approximation. However, this is a very good approximation that yields a very accurate result within a large range of different winding widths - covering most of the practical designs.

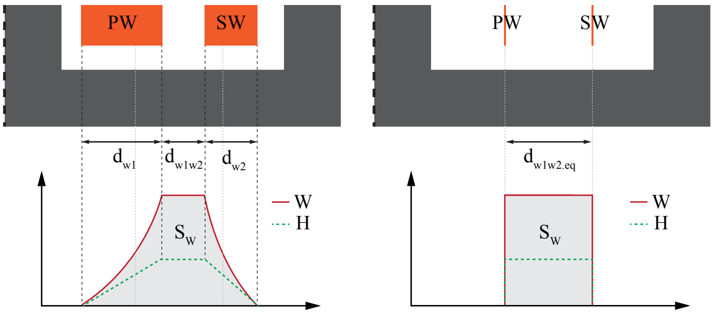

(a) (b)

Fig. 5.4 Winding geometry equivalence in respect to total magnetic energy (S_W) preservation: (a) Standard 2-winding example (b) Theoretical equivalence with infinitely thin windings.

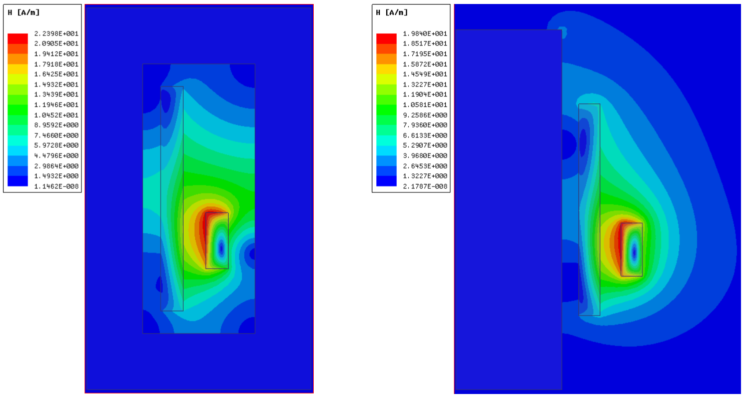

(a) (b)

Fig. 5.5 An example of the 2D magnetostatic FEM simulation of the magnetic field inside (a) and outside (b) of the core window area.

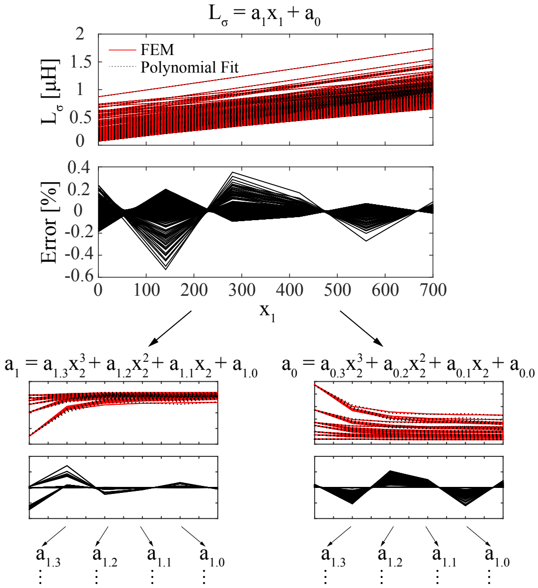

Fig. 5.6 Multi-variable polynomial fitting of the MFT leakage inductance to the results of the 2D FEM sweep (approximately 50'000 simulations).

A 2D magnetostatic FEM parametric sweep has been performed, generating the set of leakage inductance estimations (approximately 50'000 simulations) within the geometry range of interest according to **Tabs. 5.1** and **5.2**, covering all of the practically relevant geometry ratios, as displayed in **Figs. 5.5(a)** and **5.5(b)**.

Based on these results, and taking into account the minimum vector of influential variables (**x**), as summarized in **Tabs. 5.1** and **5.2**, a multi-variable polynomial fitting is done variable by variable, as shown in **Fig. 8.6**, allowing to always choose the minimum adequate polynomial order while inherently ensuring convergence. The final result of this fitting is a multi-dimensional array of polynomial parameters. For the sake of illustration, an example of the described model, for a two variable case is shown in (5.26).

$$L'_{\sigma.fit} = \begin{bmatrix} x_1 \\ 1 \end{bmatrix}^T \begin{bmatrix} a_{1.3} & a_{1.2} & a_{1.1} & a_{1.0} \\ a_{0.3} & a_{0.2} & a_{0.1} & a_{0.0} \end{bmatrix} \begin{bmatrix} x_2^3 \\ x_2^2 \\ x_2 \\ 1 \end{bmatrix} \tag{5.2}$$

As can be seen, the evaluation of the model boils down to simple low order matrix multiplication. While this operation executes very fast on the processor, depending on how many variables (N) are involved, and what are the orders of the polynomial fittings (n_i), there is $\prod_{i=1}^{N} n_i$ polynomials to be solved. Although this model is still executing very fast for the case of 6-variables, described by **Fig. 5.3** and **Tabs. 5.1** and **5.2** (three orders of magnitude faster compared to FEM), it is possible to further optimize the model. Rearranging the order in which the polynomial is executed based on the algorithm allows for a part of the multi-variable polynomial, involving variables that have been defined, to be pre-calculated and only execute the part of the model dealing with optimization variables within the optimization loop. Doing this, in case that not all of the variables ($\mathbf{x}$) are being actively changed in the most nested optimization loop, it is possible to even further improve the overall execution time.

The resulting multi-variable polynomial models of the two geometric primitives from **Fig. 5.3** have been compared to the results of the FEM sweep, as displayed in **Fig. 5.7**. As can be seen, the errors are very low (below 4% for any practical design), confirming the good precision of the model.

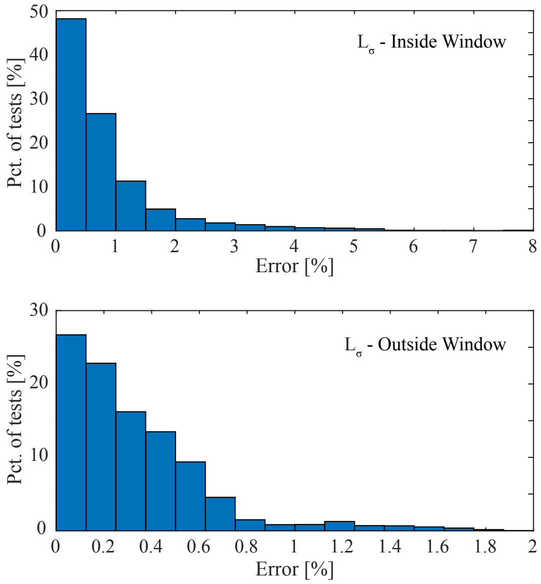

Fig. 5.7 Histograms of the relative leakage inductance estimation error, referred to the FEM results (approximately 50'000 test samples).

5.2.2 Application of the Model

Calculation of the total 3D leakage inductance boils down to a few simple steps. First, the dimensions of the two geometric profiles of the MFT, as seen in **Fig. 5.3**, need to be identified and transformed using (5.1) according to **Tabs. 5.1** and **5.2**. This leads to

$$d_{w1w2.eq01} = d_{w1w2} + \frac{1}{3}(d_{w1} + d_{w2} - \frac{2}{3}0.1h_w) \tag{5.3}$$

where $d_{w1w2.eq01}$ is the equivalent inter-winding dielectric distance of the generalized geometry primitive with selected constant normalized winding widths ($0.1h_w$).

Taking into account (5.3), the two multi-variable polynomial models (f_1 and f_2), describing the magnetic energy inside and outside of the core window area are evaluated leading to per-length leakage inductances

$$L'_{\sigma.in} = f_1(\mathbf{x}_1) \tag{5.4}$$

$$L'_{\sigma.out} = f_2(\mathbf{x}_2) \tag{5.5}$$

where $\mathbf{x}_1$ and $\mathbf{x}_2$ are the normalized variable vectors from **Tabs. 5.1** and **5.2**, respectively. Weighted sum of these two values in respect to the portions of the MLT inside and outside of the core window area (see **Fig. 5.2(a)**) leads to the equivalent per-length leakage inductance

$$L'_{\sigma.eq} = \frac{1}{A + D}(DL'_{\sigma.in} + AL'_{\sigma.out}) \tag{5.6}$$

An example of these values for a nine-secondary multi-winding transformer prototype, as displayed in **Fig. 5.9**, with a geometry profile, as shown in **Fig. 5.2**, is given in **Fig. 5.8**.

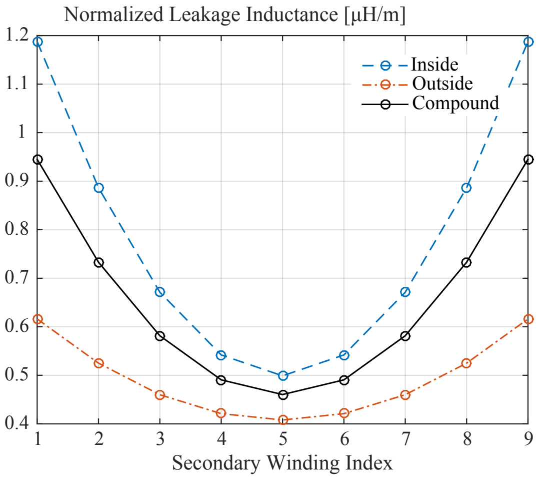

Fig. 5.8 An example of the per-length primary to i-th secondary winding leakage inductance calculation of a multi-winding transformer with a geometry profile, as shown in **Fig. 5.2**, in case of nine secondary windings, according to the prototype, as given in **Fig. 5.9**.

Finally, the total leakage inductance referred to the primary winding of the transformer can be calculated, as shown in (5.7).

$$L_{\sigma.total} = N_1^2(MLT)L'_{\sigma.eq} \tag{5.7}$$

Depending on the design task, beside the direct estimation, this fast executing model also facilitates simple and numerically efficient inverse calculation of any single or arbitrary combination of geometric dimensions $\mathbf{x}$ (e.g. d_{w1}, d_{w1}, d_{w1w2}) in order to match the reference leakage inductance.

5.2.3 Experimental Verification

The presented modeling is verified with a full 3D FEM model and measurement on a muti-winding transformer prototype [88], as displayed in **Fig. 5.9**, with geometry profile, as shown in **Fig. 5.2**, with nine secondary windings. All of the geometric dimensions, construction details and leakage inductance measurement between each secondary and primary winding can be found in [88].

Plots of the measured and estimated total leakage inductance between the primary and each of the secondary windings and relative estimation errors are displayed in **Fig. 5.10**. Estimation is done both with proposed statistical data-driven model (SDDM) and full 3D FEM for comparison purposes. A slight under estimation of the total leakage can be observed for both models. This is most likely due to a small additional leakage inductance of the extended termination of the windings and connection cables. As expected the proposed SDDM performs within the 5% error compared to FEM, achieving good accuracy with less than 9% error compared to the measurement even in case of such extreme geometry ratios.

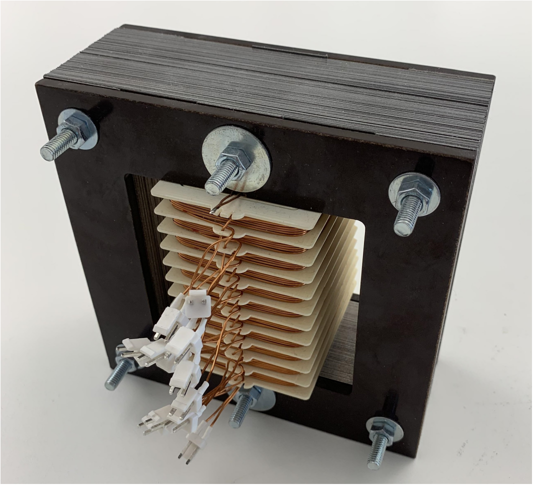

Fig. 5.9 A multi-winding transformer prototype for experimental verification [88].

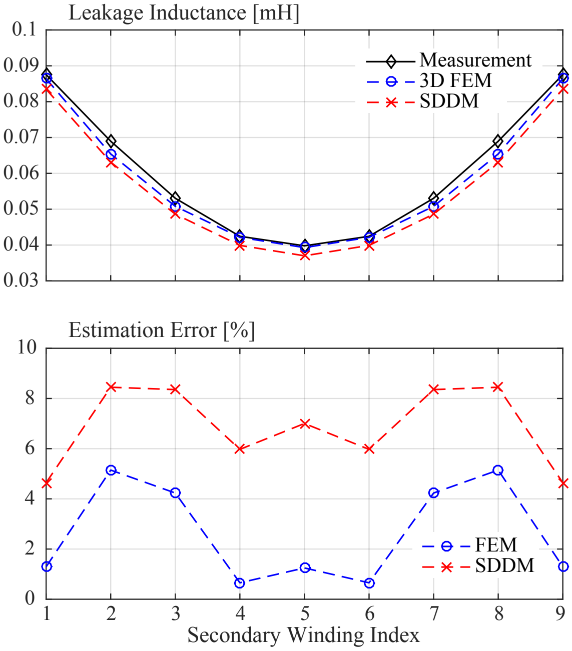

Fig. 5.10 Top: plots of the measured and estimated (both with the 3D FEM and the proposed SDDM) total primary to i-th secondary winding leakage inductance of the multi-winding transformer prototype from **Fig. 5.9** referred to each secondary winding. Bottom: Plots of the relative estimation errors of the 3D FEM and the proposed SDDM referred to the measurements.

5.3 Local Electric Field Modeling Within MFT Insulation

While it is possible to very accurately model the electric field distribution via some computationally intensive numerical method, such as finite elements method (FEM), the execution time and numerical stability are often limiting factors when it comes to a multi-variable optimization. To that end, this section proposes a suficiently-accurate (error $<$ 5% referred to FEM) modeling methodology for parasitic capacitance and local E-field maximum estimation, specially designed for very fast execution - more than four orders of magnitude faster compared to FEM.

Insulation coordination is an essential step in the design process of any medium (MV) or high (HV) voltage power transformer that ensures its proper and safe operation. This task is especially challenging in case of medium (MF) and high (HF) frequency transformers operating within power electronics converters - increasingly popular solid state transformer (SST) concept [46]. Whether it is a fast rising front of the basic lightning impulse (BIL) test waveform, as shown in **Fig. 5.11(a)**, or very fast switching of the new generation SiC semiconductors, parasitic capacitances of the transformer windings will affect the voltage and electric (E)-field distribution over the winding turns during these fast transients, as displayed in **Figs. 5.11(b)** and **5.12**, and therefore cannot be neglected [89], [90].

However, due to high complexity, computational cost and need for customization of FEM models, very precise models such as described in [89], [90] are not suitable for overall multi-variable design optimization, but rather for final design verification and its correction through several final iterations [27], [28], [43], [46]. This section proposes a very-fast and numerically-stable estimation methodology that allows a proper inclusion of the insulation coordination considerations within the design optimization process.

For the purposes of design optimization, the BIL is approximated with a Heaviside step function as a worst case scenario, as displayed in **Fig. 5.11(a)**. This approximation allows the reduction of the complex HF winding model, to a network of parasitic capacitances, as shown in **Fig. 5.13(a)**, which can be analytically solved in closed form, as given in

$$V(i) = V\frac{\sinh(\alpha i)}{\sinh(\alpha N)} \quad \text{where} \quad \alpha = \sqrt{\frac{C_{t2c}}{C_{t2t}}} \tag{5.8}$$

where i is the winding turn index, N is the total number of turns and C_{t2c} and C_{t2t} are the turn-to-core and turn-to-turn parasitic capacitances, respectivelly.

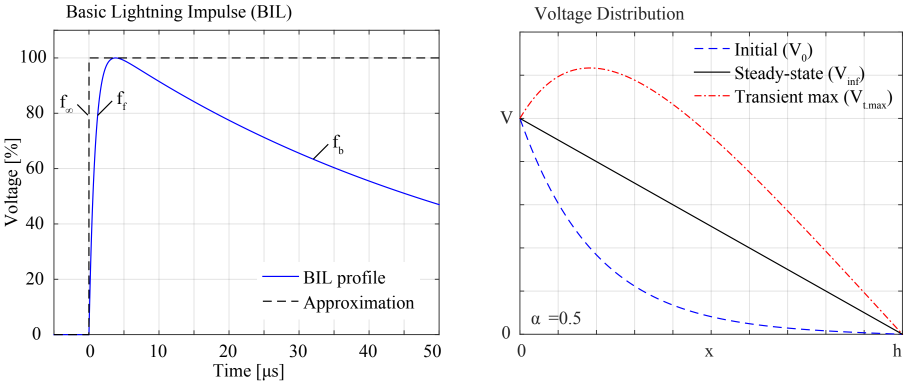

(a) (b)

Fig. 5.11 (a) Standard 1.2/50 µs full-wave lightning impulse profile, according to IEEE Std 4-1995 and IEEE Std C57.98-1993 (equivalent frequencies of the fast rising front and slow descending back are f_f = 200 kHz and f_b = 5 kHz, respectively). (b) Example of the theoretical envelope of the voltage distribution over the transformer winding turns during fast "ringing" transients where: V_0 is the initial voltage distribution at $t = 0$; V_{tm} is the maximum theoretical turn voltages during subsequent "ringing" transient; V_{inf} is the voltage distribution after the fast transient response has transpired.

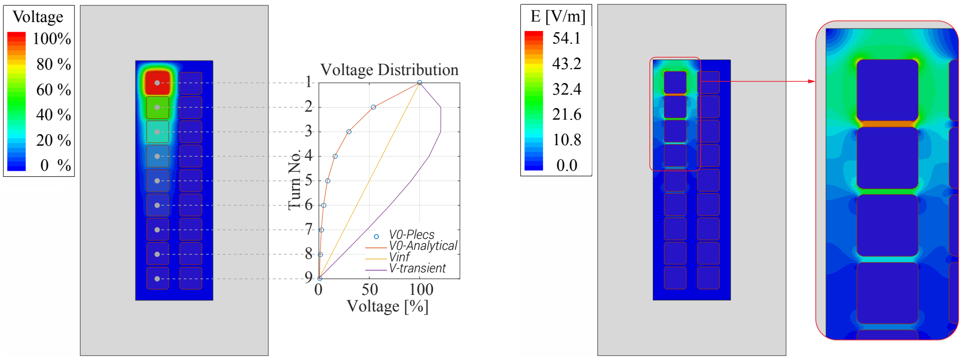

(a) (b)

Fig. 5.12 2D electrostatic FEM simulation of a representative MFT cross-section example, excited with a theoretical BIL approximation (Heaviside step function) at the moment of incidence ($t = 0$): (a) voltage distribution and (b) E-field distribution.

The voltage and E-field distribution over the transformer winding excited with Heaviside step function, at the moment of the pulse incidence ($t = 0$), are shown in **Figs. 5.12(a)** and **5.12(b)**, respectively. It can be seen that the initial voltage distribution over the winding turns (V_0) is uneven - the first turns are experiencing turn-to-turn voltages drastically above the nominal value. Moreover, some turns experience high, above-nominal, absolute voltage levels during the fast transient on natural frequency of the winding (V_{tm}). This causes high local E-field magnitude-peaks that may lead to gradual (or in extreme cases instant) annihilation of the insulation material if not properly accounted for. Good understanding of the main parameters governing this phenomena is necessary for the proper insulation coordination. From a design point of view, reliable modeling is paramount in order to avoid massive and costly over-sizing.

5.3.1 Proposed Modeling

A detailed electrostatic finite elements method (FEM) analysis is performed to identify the critical regions, where the insulation material is experiencing the highest dielectric stress. As can be seen in **Fig. 5.12(b)**, the maximum local E-field magnitude peaks are occurring somewhere along the conductor edge. These local E-field maximums are a function of the geometry and voltage distribution. On the other hand, assuming the Heaviside step excitation, the voltage distribution is purely a function of turn-to-core and turn-to-turn parasitic capacitances, which again depend only on the geometry. Therefore, in order to predict the maximum local E field peaks, it is necessary to:

(i) Model the parasitic capacitances, based on the known design geometry

(ii) Solve the parasitic capacitance network to obtain the voltage distribution

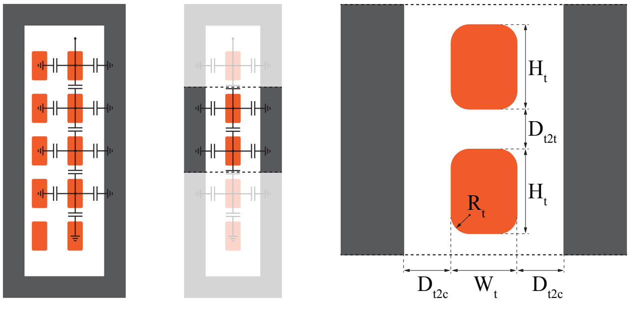

(a) (b) (c)

Fig. 5.13 (a) Full parasitic capacitance model of a generalized MFT geometry cross-section. (b) Simplified geometry equivalence. (c) Minimal generalized geometry detail.

Tab. 5.3 Definition and range of the normalized parameters, according to **Fig. 5.13(c)**

Norm. Vars.	x_1	x_2	x_3	x_4	x_5
Definition	$\frac{H_t}{W_t}$	$\frac{D_{t2t}}{W_t}$	$\frac{D_{t2c}}{H_t}$	$\frac{R_t}{\min(H_t, W_t)}$	$\frac{U_{t2t}}{U_{t2c}}$
Range	0.25 – 4	0.01 – 4	0.01 – 4	0.02 – 0.5	0 – 1

Note that these are very extensive ranges, covering most of designs

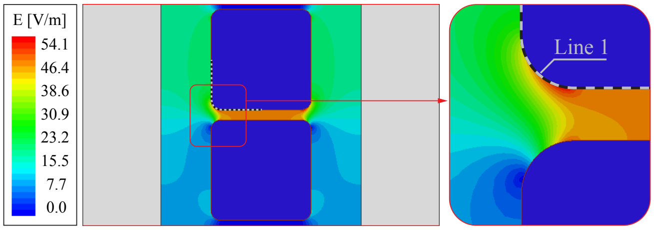

Fig. 5.14 2D electrostatic FEM simulation of the minimal generalized geometry detail.

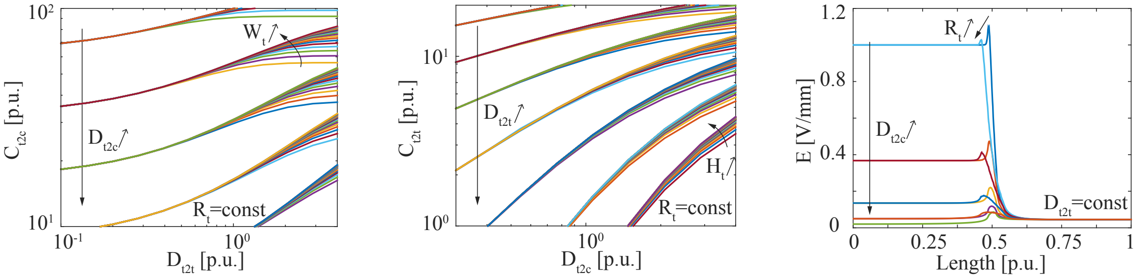

(a) (b) (c)

Fig. 5.15 Plots of families of curves, exposing the effects of various parameters, as given in **Tab. 5.3**, on: (a) turn-to-core $C_{t2c} = f_1(x_1, x_2, x_3, x_4)$, (b) turn-to-turn $C_{t2t} = f_2(x_1, x_2, x_3, x_4)$ parasitic capacitances and (c) the local E-field magnitude peak along the edge of the turn conductor $E_{max} = f_3(x_2, x_3, x_4, x_5)$, as highlighted with Line 1 in **Fig. 5.14**.

(iii) Model the local E-field maximum, based on the known geometry and voltage distribution

While (ii) boils down to a simple evaluation of (5.8) in case of Heaviside step-function excitation, (i) and (iii) remain numerically challenging. The remainder of this section, describes in detail the proposed methodology for very fast estimation of these values - data-driven statistical models derived based on extensive FEM simulation.

A full parasitic capacitance network can be seen in **Fig. 5.13(a)**. Taking into account that both the core and secondary winding are at the ground potential, the secondary winding can also be seen as a straight wall boundary at the ground potential, as shown in **Fig. 5.13(b)**. Note that, all conductive parts of the transformer, including any other winding except the one being excited by the test pulse, are grounded at all terminals during the BIL test, as recommended by IEEE Std 4-1995 and IEEE Std C57.98-1993. Finally, based on the geometric symmetry and periodic structure of the winding, a minimal generalized geometry detail, capable of capturing all of the phenomena of interest, is identified and parametrised, as given in **Fig. 5.13(c)** and **Tab. 5.3**.

A 2D FEM parametric sweep is performed on the generalized geometry detail (**Fig. 5.14**), as defined in **Tab. 5.3**, extracting the turn-to-core and turn-to-turn parasitic capacitances and maximum local E-field peaks within the parameter ranges of interest. Sample plots of this data, illustrating the effects of various parameters on the modeled values are shown in **Fig. 5.15**. Taking into account the minimum vector of influential variables (**x**), as summarized in **Tab. 5.3**, a multi-variable polynomial fitting is performed on these data sets in the same fashion, as described in **Sec. 5.2**, thus generating the corresponding data-driven statistical models

$$C_{t2c} = f_1(x_1, x_2, x_3, x_4) \tag{5.9}$$

$$C_{t2t} = f_2(x_1, x_2, x_3, x_4) \tag{5.10}$$

$$E_{max} = f_3(x_2, x_3, x_4, x_5) \tag{5.11}$$

with inherent high accuracy of FEM simulations and very low computational cost, characteristic for simple arithmetic operations (matrix multiplications) needed for evaluation of polynomials.

As described in **Sec. 5.2**, the evaluation of these models boils down to simple low order matrix multiplications which execute very fast on the processor. In case of 4-variables, as described by **Fig. 5.13(c)**, **Tab. 5.3**, and **Fig. 5.15**, these models execute more than four orders of magnitude faster than FEM.

All three models ((5.9), (5.10) and (5.11)) are derived under assumption of surrounding vacuum. A different insulation material can easily be taken into account with a simple multiplication/division with its relative permittivity ε_r. Moreover, note that the formula for local E-field maximum is a function of the voltage distribution and therefore covers all relevant voltage distributions that may be encountered during normal (V_{inf}) or transient operation (V_0 and V_{tm}).

5.3.2 Simulation Results

Relative estimation errors of the three earlier mentioned multi-variable polynomial models referred to the FEM simulation results are given in **Fig. 5.16**. It can be seen that a very good accuracy can be achieved, with errors practically below 5%, while decreasing the execution time four orders of magnitude compared to FEM.(5.8)-(5.11) together formulate a framework for a computationally efficient estimation of the local E-field maximums allowing the study of separate influences on insulation coordination and overall design optimization.

Even beyond this specific study, this new class of models, optimized for the best trade-off between accuracy and execution speed will enable further inclusion of very sophisticated simulations, with otherwise impractically high computational cost, into design optimization process, resulting in cutting edge performance.

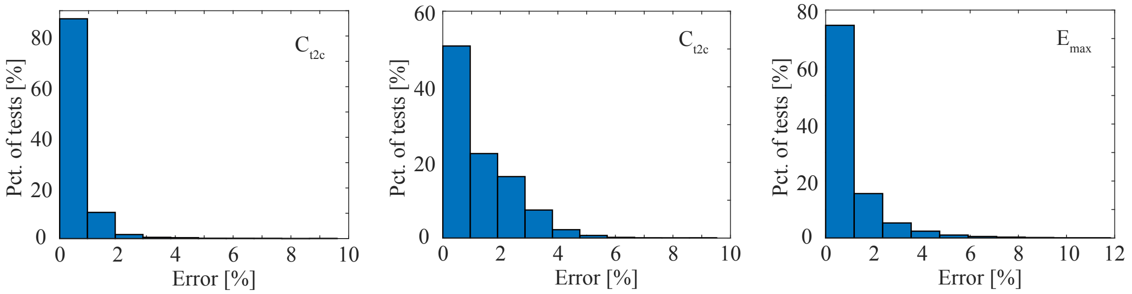

(a) (b) (c)

Fig. 5.16 Relative estimation error histograms of the proposed data-driven statistical models for computation of: (a) turn-to-core parasitic capacitance, (b) turn-to-turn parasitic capacitance and (c) maximum local E-field magnitude peak.

5.4 Geometry Dependent Core Loss Modeling

This section addresses the technical challenges of ferromagnetic core loss estimation for medium frequency transformers. While the core losses are usually characterized from the manufacturer side for a given ferromagnetic material on a toroidal sample with sinusoidal excitation, these results are not necessarily directly transferable to typical conditions encountered within power electronic converters. Moreover, the presence of core cuts and its rectangular geometry with sharp corners have a significant influence on magnetic field distribution and therefore the localized loss density. A detailed analysis and modeling of the mentioned effects is presented in this section together with experimental characterization of various core samples of interest considering both sinusoidal and square voltage excitation within the relevant frequency range. Derived models allow to generalize the core loss estimation based on characterization of one core sample to any different core shape and size made of the same material and same technology.

Regardless of the power or voltage range, magnetic components are a necessary part of any power electronic converter, having a significant impact on its efficiency and power density. Two main types of losses occur in magnetic components: core and winding losses. While for some components, such as DC filter inductors, core losses can be neglected, for others, such as transformers and AC inductors, they represent a significant portion of total losses and need to be properly addressed [91].

It is a common design approach to assume homogeneous magnetic induction field distribution within the transformer core volume. This allows for very simple core loss estimation and characterization. Core loss density distribution, as a direct function of the magnetic induction field, becomes uniform regardless of the core shape and size, thus neglecting the geometry effects on the total core loss. In other words, it is assumed that a toroidal and a rectangular core, as displayed in **Tab. 5.4**, with same cross section ($A_t = A_r$) and magnetic path length ($l_{mt} = l_{mr}$), with same excitation, would have the same total losses. This allows to directly transfer the conclusions, based on measurements on a small toroidal core sample, to any core shape and size with the given material.

Nevertheless, depending on the core shape and structure, this assumption does not hold in general. There have been some efforts to analyze the effect of geometry on various core properties: measurements in [92] experimentally quantify the influence of the core geometry on no-load loses on industrial distribution transformers in the [16 – 20]MVA power range. The work presented in [93] identifies and experimentally verifies the influence of various geometry ratios on total losses of toroidal cores. [94] offers an analytic formulation and approximations of the partial differential

Tab. 5.4 Two most common core geometries, toroidal and rectangular, and their equivalent magnetic length.

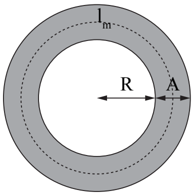	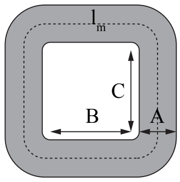
$l_m = 2(R + \frac{1}{2}A)\pi$	$l_m = 2(\frac{\pi}{2}A + B + C)$

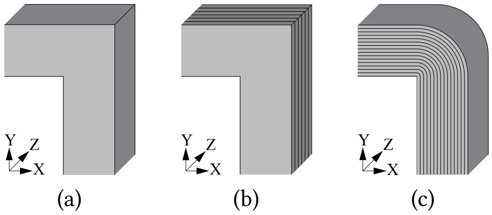

Fig. 5.17 Considered core structures: (a) isotropic; (b) axial lamination (in Z axis); (c) radial lamination.

equations used in FEM to estimate the fields and the loss distributions within the rectangular and toroidal cores with or without cuts. In [95], FEM is utilized to analyze the the effect of higher order excitation harmonics. Analysis of the possible accuracy improvement of electric simulations by including geometry based implications is described in [96].

This section analyzes in detail the core structures of interest, as shown in **Fig. 5.17**, identifying and modeling the geometry related effects on magnetic field distribution and resulting core losses. Compared to the mentioned state of the art, radially laminated cores, typical for increasingly popular nanocrystalline and metglas materials, are included in the study. Moreover, the models derived in this work can offer a direct relation between the core loss measurements on any specific core geometry sample to any different core geometry, made of the same material and with same technology, up to some degree of accuracy.

5.4.1 FEM Analysis

In order to identify the main effects of the core geometry, a detailed electromagnetic FEM analysis is performed on equivalent ($A_t = A_r, l_{mt} = l_{mr}$) parametrized rectangular and toroidal core models, as displayed in **Fig. 5.18**. Two intrinsically different core structures are considered: xy-isotropic (isotropic or axial laminated) and xy-anisotropic (radial laminated). It can be seen that the radial lamination has a significant influence on the magnetic induction field distribution. In contrast to

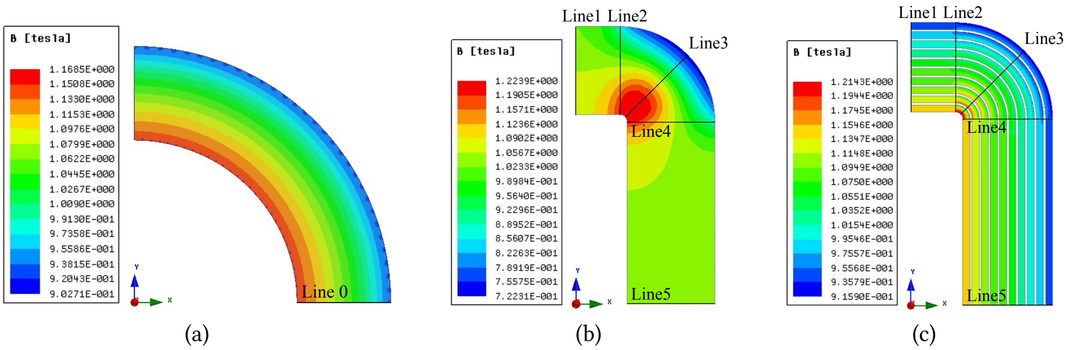

Fig. 5.18 Example of magnetic induction field distribution (B) within equivalent: (a) toroidal core, (b) rectangular xy-isotropic core (isotropic or laminated in Z axis) and (c) rectangular xy-anisotropic core (radial lamination; scaled down model to 10 sheets while maintaining the proportions), excited close to saturation (B_{sat}).

xy-isotropic cores where magnetic reluctance is equal in all directions of the xy-plane, insulation (adhesive) gaps between the radially stacked ferromagnetic sheets represent a high reluctance path ("barrier") for the magnetic flux. Consequently, the average flux density is conserved along each ferromagnetic sheet path.

Plots of the magnetic induction field magnitude along a couple of radial lines, representative of the varying conditions within the given core sections are presented in **Fig. 5.19**. It can be seen that the field density distributions within the corner and straight regions of an xy-isotropic core are very different, whereas the average flux density within each sheet of a radially laminated core remains the same regardless of the region. Note that the variations from this average values in the corner regions are significantly smaller (negligible) in reality, as the lamination is roughly two orders of magnitude thinner compared to the ten-sheet downscaled model used in this study.

Comparing the average field densities within the lamination layers and the toroidal core, it can be concluded that a radially laminated rectangular core behaves exactly the same as its equivalent toroid core. On the other hand, it can be approximated that a rectangular xy-isotropic core behaves like a toroid with inner radius tending to zero in the corer regions, whereas the field density is uniformly distributed within its straight portions.

Moreover, it can be seen that the flux density has an effect on the field distribution. Magnetic reluctance of the material changes with the field density due to the nonlinear B-H characteristic (saturation), thus causing the flux density redistribution.

Finally, the air-gap has practically no effect on the flux distribution within xy-isotropic cores, whereas it causes the average field densities within the radial lamination layers of the xy-anisotropic cores to equalize, as shown in **Fig. 5.19(c)**. Depending on the size of the air-gap, a relatively large reluctance is added in series to the magnetic reluctance of each lamination path, thus rendering the reluctance difference of each path proportionally smaller. Consequently, the larger the air-gap, the more equal the flux distribution.

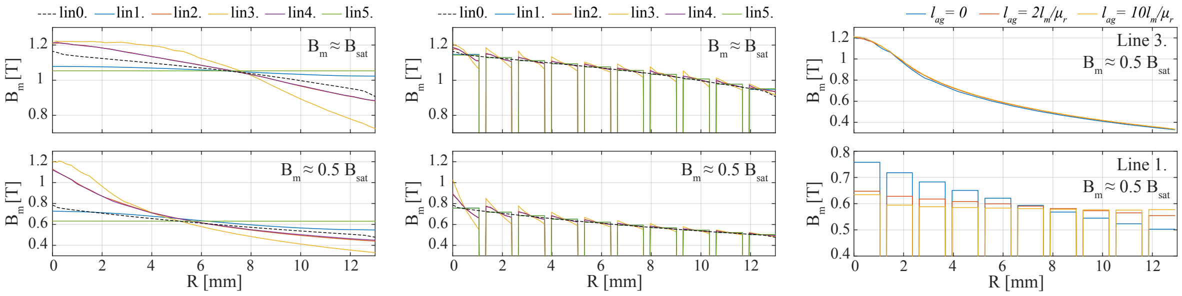

(a) (b) (c)

Fig. 5.19 Plots of the flux density magnitude along a couple of representative lines, as shown in **Fig. 5.18**, exposing the different field distribution in different core regions for: (a) toroid and xy-isotropic (isotropic or laminated in Z axis) rectangular core at 100% (top) and 50% (bottom) of the saturation induction (B_{sat}); (b) toroid and xy-anisotropic (radial laminated) rectangular core at 100% (top) and 50% (bottom) of B_{sat}; (c) rectangular xy-isotropic (top) and xy-anisotropic (bottom) cores with the presence of air-gap (l_{ag}) at 50% of B_{sat}.

5.4.2 Proposed Modeling Approach

Based on the previous analysis, the proposed geometry dependent modeling of the field distribution within both the xy-isotropic and xy-anisotropic cores boils down to proper modeling of toroidal cores with various $K_t = A/R_m$ proportions at different flux density levels.

A generalized toroid core geometry detail is shown in **Fig. 5.20**. Starting from the analytic expression for the magnetic field within the infinitesimally narrow layer along the equi-magnetic-field intensity line of the toroid core

$$H_m(r) = \frac{NI_m}{2\pi r} \tag{5.12}$$

and taking into account the non-linear B-H curve of the magnetic material, it is possible to reproduce the magnetic induction field density distribution within the generalized toroid core

$$B_m(r) = B_m(H_m(r))H_m(r) \tag{5.13}$$

where $B_m(H_m)$ represents the exact characteristic B-H curve of the given material. This curve can either be obtained by means of characterization and directly sampled using interpolation, as shown in **Fig. 5.21**, or alternatively some B-H curve model can be employed, such as described in [96], [97]. Moreover, it is assumed that the B-H curve is frequency-independent within the normal operating frequency range for the given core. This assumption is typically true as the operation at frequencies high enough for μ_r to start to decrease is tied to a dramatic (usually unacceptable) increase of losses.

In order to enable the modeling using only the available manufacturer data-sheet data, an arctan based B-H curve model is derived, similar to the procedure described in [97]. The form of the model is given in as

$$B_m(H_m) = C_1 \arctan(C_2 H_m) + \mu_0 H_m \tag{5.14}$$

where the constants C_1 and C_2 can be obtained from the two boundary conditions:

(i) Asymptotic convergence at high H_m

$$B_m(H_m \longrightarrow \infty) = B_{sat} + \mu_0 H_m \tag{5.15}$$

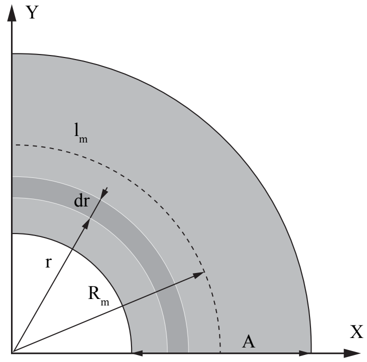

Fig. 5.20 Geometry detail of a generalized toroid core

Taking into account $\lim_{x\to\infty}\arctan(x) = \pi/2$, the first coefficient can be expressed as

$$C_1 = \frac{2B_{sat}}{\pi} \tag{5.16}$$

(ii) According to the definition of $\mu_r = B_{sat}/(\mu_0 H_{sat})$, H_{sat} is defined as a value of magnetic field where saturation level reaches 90%

$$B_m(H_{sat}) = 0.9B_{sat} \tag{5.17}$$

Substitution of (5.14) and (5.16) in (5.17) leads to

$$C_2 = \frac{\mu_0\mu_r}{B_{sat}}\tan\left(\frac{0.9\pi}{2}\right) \tag{5.18}$$

As can be seen in **Fig. 5.21**, (5.14),(5.16) and (5.18) offer a sufficiently accurate B-H curve model that utilizes only the available data-sheet information, i.e. μ_r and B_{sat}, that is used in the rest of the analysis in this section.

According to original Steinmetz equation, the average core loss density within the entire core volume can be expressed as a function of frequency and flux density magnitude

$$p_{\sigma.avg} = Kf^{\alpha}B_{m.avg}^{\beta}. \tag{5.19}$$

This leads to the geometry independent total per-length core losses

$$P'_{\sigma.tot} = p_{\sigma.avg}2\pi R_m A. \tag{5.20}$$

Note that a different core loss density model can be used as well - e.g. improved generalized Steinmetz equation (IGSE) [68] for non-sinusoidal excitation waveforms. For the sake of simplicity, the derivation in this section is done with the original Steinmetz equation.

However, application of the Steinmetz, or some other selected equation on the flux density distribution function from (5.13) generates the geometry dependent core loss distribution

$$p_{\sigma}(r) = Kf^{\alpha}B_m^{\beta}(r). \tag{5.21}$$

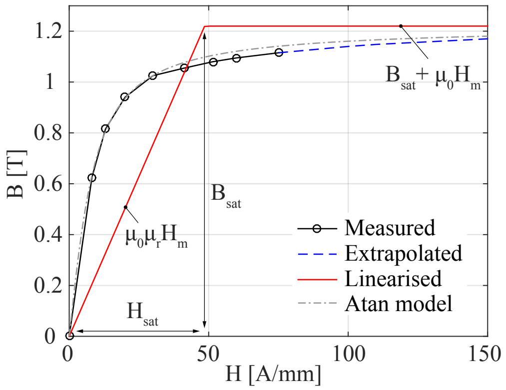

Fig. 5.21 B-H curve of nanocrystalline - Finemet

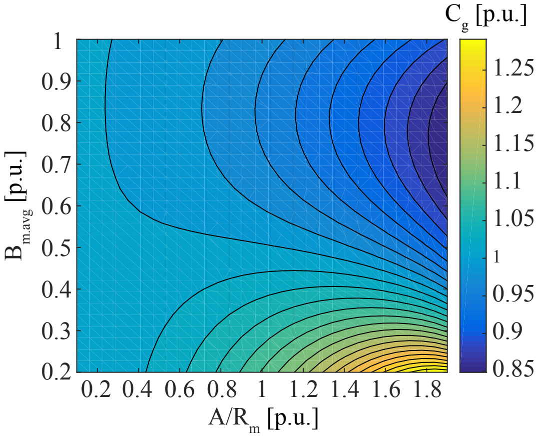

Fig. 5.22 Map of the core loss geometry coefficient for the measured B-H curve, as displayed in **Fig. 5.21** and β = 2.1.

A surface integral of this function leads to the total geometry-dependent per-length core losses

$$P'_{\sigma.tot.g} = \int_S p_\sigma ds = \int_{R_m - A/2}^{R_m + A/2} p_\sigma(r)\, 2\pi r\, dr. \tag{5.22}$$

The geometry related effects on the core losses can be expressed with a geometry factor

$$C_g = \frac{P'_{\sigma.tot.g}}{P'_{\sigma.tot}}. \tag{5.23}$$

Finally, substitution of (5.19), (5.20), (5.21) and (5.22) in (5.24) leads to

$$C_g = \frac{1}{R_m A B^{\beta}_{m.avg}} \int_{R_m - A/2}^{R_m + A/2} B^{\beta}_m(r) r\, dr. \tag{5.24}$$

This integral requires numeric integration as $B^{\beta}_m(r)$ is a non-linear function whose integral cannot be analytically expressed. Numeric integration of (5.24) is performed with respect to (5.12) and (5.13) for all variations of $B_{m.avg}$ and A/R_m in their corresponding ranges of interest, from 0.2 to 1T and from 0.1 to 1.9p u , respectively, thus generating a map of the geometric core loss coefficient, as displayed in **Fig. 5.22**.

It can be seen that the total losses may vary roughly within the range of −20% to +10% compared to the averaged estimation, as given in (5.20). Moreover it is interesting to notice that the core losses increase with the increase of A/R_m at the light saturation ($B_{m.avg}$ in range 0.2 to 0.4T) whereas the opposite is true at high saturation($B_{m.avg}$ in range 0.6 to 0.1T). This is an expected result as the relative value of μ_r is very high at low $B_{m.avg}$, thus causing a significant increase of the local B_m as a result of the increased H_m in the inner regions of the core ($r < R_m$). This increase in B_m directly affects the local core loss density according to (5.21).

On the other hand, at high $B_{m.avg}$, μ_r is substantially lower, thus the local B_m increase within the inner regions of the core compared to $B_{m.avg}$ is not so pronounced. This effect can clearly be observed in **Fig. 5.19(a)**. Moreover, the local B_m in the outer core regions ($r > R_m$) decreases as a result of the

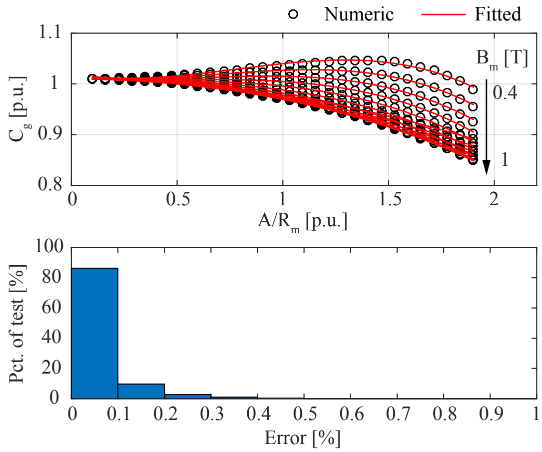

Fig. 5.23 Multi-variable polynomial fitting of the geometry coefficient from **Fig. 5.22** within the most important range, B_m from 0.4 to 1T and A/R_m from 0.1 to 1.9p u (a) Plots of the numeric calculation and polynomial fit of a representative family of curves within the described range. (b) Error histogram of the polynomial fit estimation referred to the numeric solution for a set of 100'000 points within the described range.

decrease of H_m with higher μ_r, characteristic for decreased H_m. Qualitatively, this effect causes the local losses in the outer core region to decrease more than the ones in the inner core region increase compared to the averaged ones, thus resulting in a decrease of the total core losses. Therefore, the A/R_m influence on the losses is the most pronounced within the $B_{m.avg}$ region where relative change of the μ_r is the highest, between 0.8 and 0.9T, as can be seen in **Fig. 5.21**.

In order to achieve good utilization of the ferromagnetic material and the magnetizing characteristic as linear as possible, the preferred B_m operation is usually slightly below the knee of the B-H curve, between 0.5 and 0.9T for the the given material, as displayed in **Fig. 5.21**. In order to facilitate a very fast model execution, required in design optimization applications [28], a third-order multi-variable polynomial fitting of the geometric core loss coefficient, such as described in detail in [98], is performed on the results of the numeric calculation of 100'000 test points within the $B_{m.avg}$ range between 0.4 to 1T, as displayed in **Fig. 5.23**. It can be seen that a very accurate fit can be achieved within 0.5% error compared to the numeric solution.

The derived multi-variable polynomial model has the next form

$$C_g = \begin{bmatrix} B_m^3 \\ B_m^2 \\ B_m \\ 1 \end{bmatrix}^T \begin{bmatrix} A_m \end{bmatrix} \begin{bmatrix} (A/R_m)^3 \\ (A/R_m)^2 \\ (A/R_m) \\ 1 \end{bmatrix} \tag{5.25}$$

where

$$A_m = \begin{bmatrix} 0.043 & -0.476 & 0.481 & -0.077 \\ -0.309 & 1.852 & -1.305 & 0.204 \\ 0.476 & -2.160 & 1.195 & -0.183 \\ -0.210 & 0.755 & -0.370 & 1.065 \end{bmatrix}. \tag{5.26}$$

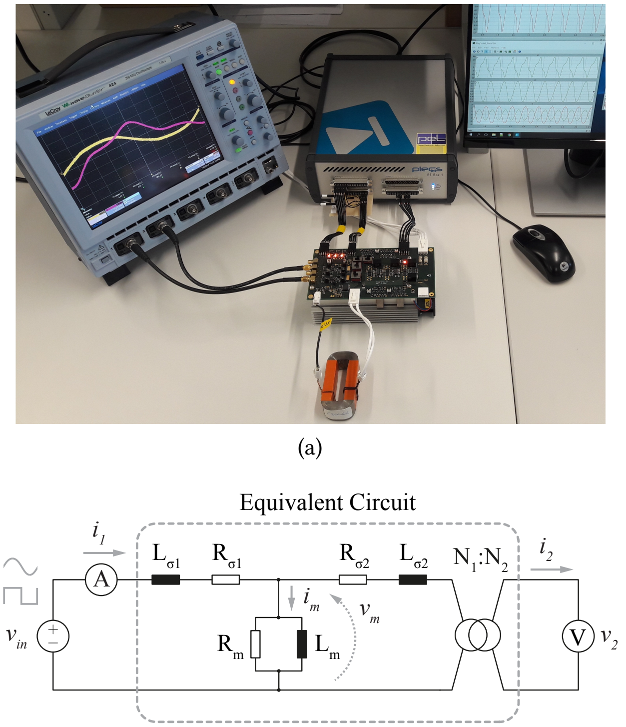

(a)

(b)

Fig. 5.24 Custom made core loss characterization setup capable of generating both sinusoidal and square voltage excitation in the frequency range of interest [99]: (a) Setup and (b) Measurement scheme.

Fig. 5.25 Custom made core samples for experimental verification. First two columns: toroidal core samples that cover a wide A/R_m geometry range. Last column: cut and uncut U cores with identical size and their equivalent toroidal core.

Models for the xy-anisotropic rectangular cores are derived by a simple application of the developed model on the equivalent toroidal core. On the other hand, modeling of rectangular xy-isotropic cores requires a breakdown into four straight segments with uniform flux density B_{avg}, and an equivalent toroid modeling the four corner elements.

Tab. 5.5 Geometric specifications of the custom made core samples

Type	A[mm]	R[mm]	B[mm]	C[mm]	l_m[mm]	A/R_m
Toroid	5	50	/	/	330	0.095
Equivalent Toroid	13	24.4	/	/	194	0.421
Toroid	13.1	7.5	/	/	88	0.935
Toroid	25.4	7.5	/	/	127	1.256
Rectangular	13	/	15	56	194	/

Equivalent Toroid is the equivalet toroidal core to the rectangular one in the last row of the table. A, R, B, C, l_m are the core dimensions, as defined in **Tab. 5.4**.

5.4.3 Experimental Verification

Experimental verification is performed to support the conclusions of the analysis and to verify the derived models. Core losses are measured using a custom made core loss characterization setup [99], as displayed in **Fig. 5.24**, on various core samples, as shown in **Fig. 5.25** and **Tab. 5.5**. The measurement principle is depicted in **Fig. 5.24(b)**. Each of the core samples is equipped with two windings, comprising a transformer. Primary winding is excited with the controllable voltage source of the characterization setup, capable of generating both sinusoidal and custom square waveforms. The secondary side is in open circuit operation ($i_2 = 0$A) - only the high-impedance voltage measurement interface is connected. Voltage measurement is therefore not sensitive to voltage drops on the winding resistance ($v_2 = v_m$). Current measurement on the other hand is performed via a shunt resistor on the primary side, thus ensuring the that there is no phase delay between the current ($i_1 = i_m$) and voltage (v_m) measurements, as given in **Fig. 5.26**.

A series of nanocrystalline toroidal and rectangular cut and uncut core samples, as given in **Fig. 5.25**, have been procured for the verification purposes of this study. This allows to make a proper breakdown of the influence of the core geometry. Identical toroidal cores featuring different A/R_m ratios, in range between 0.1 to 1.5 have been tested with sinusoidal excitation at 1kHz, as displayed in **Fig. 5.27**. All of the core loses are represented in p.u. relative to the core losses measured on the sample with extremely

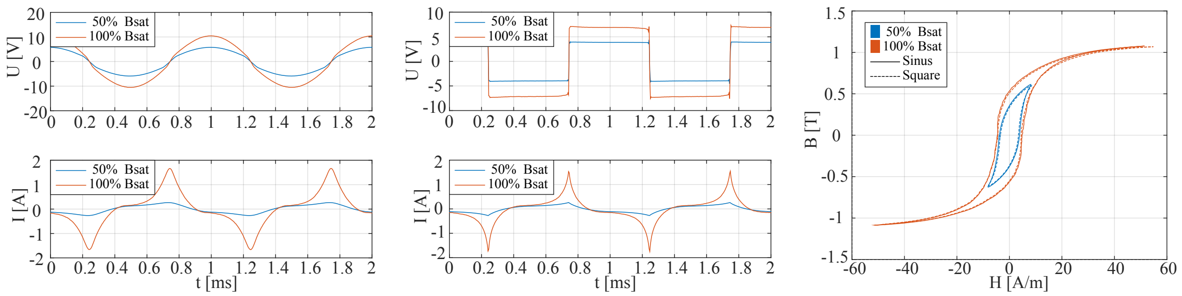

(a) (b) (c)

Fig. 5.26 Measured voltage (top) and current (bottom) plots for 50% and 100% of B_{sat} in case of sinusoidal (a) and square (b) wave excitation at 1kHz, on a nanocrystalline core sample; (c) B-H loops for all of the mentioned operating conditions.

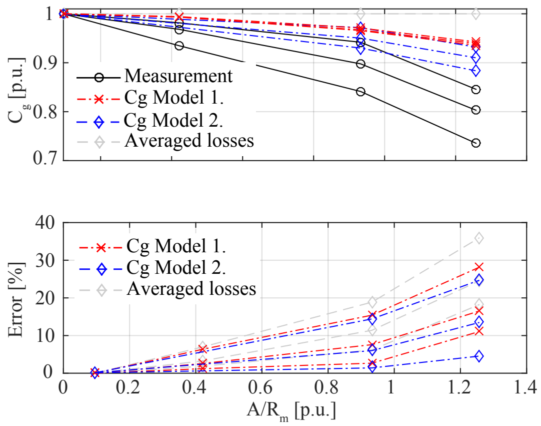

Fig. 5.27 Loss estimation and measurements on three toroidal core samples covering a wide A/R_m spectrum at three different saturation levels B_m = 0.7, 0.8 and 0.9T at 1kHz sinusoidal excitation. All of the core loses are represented in p.u. relative to the core losses measured on the sample with extremely low $A/R_m = 0.1$ where the loss distribution can be considered constant, thus directly corresponding to the derived core loss geometry coefficient. C_g model 1 and 2 refer to the core geometry coefficients obtained using the described arctan model and the exact B-H measured curve characterized on the toroidal core sample with very low $A/R_m = 0.1$, respectively.

low $A/R_m = 0.1$ where the loss distribution can be considered constant, thus directly corresponding to the derived core loss geometry coefficient. It can be seen that the derived core geometry coefficient qualitatively captures the trend of the core losses, but still relatively large errors are present up to 28%. Nevertheless, it can still offer an accuracy improvement compared to the usual averaged loss model that completely neglects the geometry related effects. It can be seen that a slightly better result can be achieved using a real measured B-H curve characterized on a toroidal core sample with a low A/R_m ratio. However, accuracy improvement is rather small, thus reinforcing the validity of the described arctan B-H model.

The rectangular uncut core and its equivalent toroidal core have been tested in the same conditions to verify the theoretical conclusions from the FEM analysis. However, in contrast to the expected, very similar/same losses, the losses within the uncut rectangular core were roughly double compared to the equivalent toroid. These increased losses within the rectangular core sample can most likely be attributed to the material stress during the manufacturing process which is known to have an effect on the resulting magnetic properties. Since this characterization was performed on only one core sample, this may not be a representative result. Additional measurements on more core samples are needed to characterize this effect with certainty and gain understanding of which are the most detrimental underlying factors. Furthermore, other core structures, i.e. isotropic and axial anisotropic, which do not experience this kind of material stress during manufacturing remain to be tested for these assumptions. This opens a topic for discussion and future work.

5.5 Conclusion

While analytical models, such as described in **Chap. 4** can solve a large part of the problem, still many phenomena cannot be accurately described in that way. This chapter proposes a computationally efficient, yet sufficiently accurate, statistical data-driven modeling framework based on FEM simulations of simple geometry details and muti-variable polinomial fitting.

The proposed modeling framework has been described in detail, showing how it is possible to transform, generalize and normalize a numerically difficult problem up to the point where a sufficiently small set of significant influences (variables) can be very efficiently captured via a neural-network inspired multi-variable polynomial model. Although already very fast (three-four orders of magnitude compared to simple 2D FEM models), these models can also be reorganized for most optimal execution depending on the specific design optimization algorithm and potentially achieve an even more drastic speed improvement. Moreover, a good estimation accuracy is achieved, with errors less than 5% relative to the 3D FEM and less than 10% relative to the measurement.

Even beyond these specific models, this type of modeling framework allows the inclusion of complex effects, which cannot be analytically approximated within reasonable accuracy limits or numerically solved within reasonable time, within the design optimization loop.

6
Design Optimization

This chapter presents the synthesis of all the models into a brute-force based design optimization algorithm. Detailed description of the proposed design optimization procedure is provided on an example of the 100kW, 10kHz *MFT designed for the operation within the SRC, featuring integrated resonant tank.*

6.1 Literature Review

There exists a multitude of formal mathematical optimization tools depending on the problem characteristics. The problem at hand is non-linear, non-convex and comprises a mix of continuous and discrete variables which classifies it as difficult and, in general, it is not possible to formally guarantee convergence or that the found solution is in fact the global optimum. Further more, proper cost setting of the multi-variable objective function, in order to reflect the desired design characteristics, is not straightforward or intuitive and any adjustments require re-optimization. In this respect, there are two dominant design optimization methodologies recurring in the literature, based either on brute-force [28], [42], [43], [100], [101] or genetic algorithms [102]–[106].

The method of choice, described in this chapter, relies on brute-force, organized using certain heuristics in such a way to allow efficient detection and avoidance of the possible design domain portions that are for sure infeasible, similar to branch and bound logic. This greatly improves the performance of this, normally very computationally intensive, approach while preserving the inherent reliability. Moreover, a very simple yet effective method is proposed for post-processing of the generated data sets, allowing intuitive navigation to the a single design or several alternative designs that best reflect the desired characteristics - volume, weight, efficiency, hot-spot temperatures, specific dimensions, etc.

6.2 Design Optimization Algorithm

The core of the proposed MFT design optimization method is the brute-force algorithm displayed in **Fig. 6.1**. It combines the functionality from design optimization techniques described in [42], [43], [100] and offers additional degrees of freedom (e.g. different characteristics and geometric proportions of the primary and secondary winding), thus generating a much more versatile design population and uncovering more design possibilities. This is enabled by proper transformations and use of novel sophisticated analytic and SDDM models [98], [107]–[110] providing improved accuracy and lower computational cost - both paramount for the quality of the overall optimization.

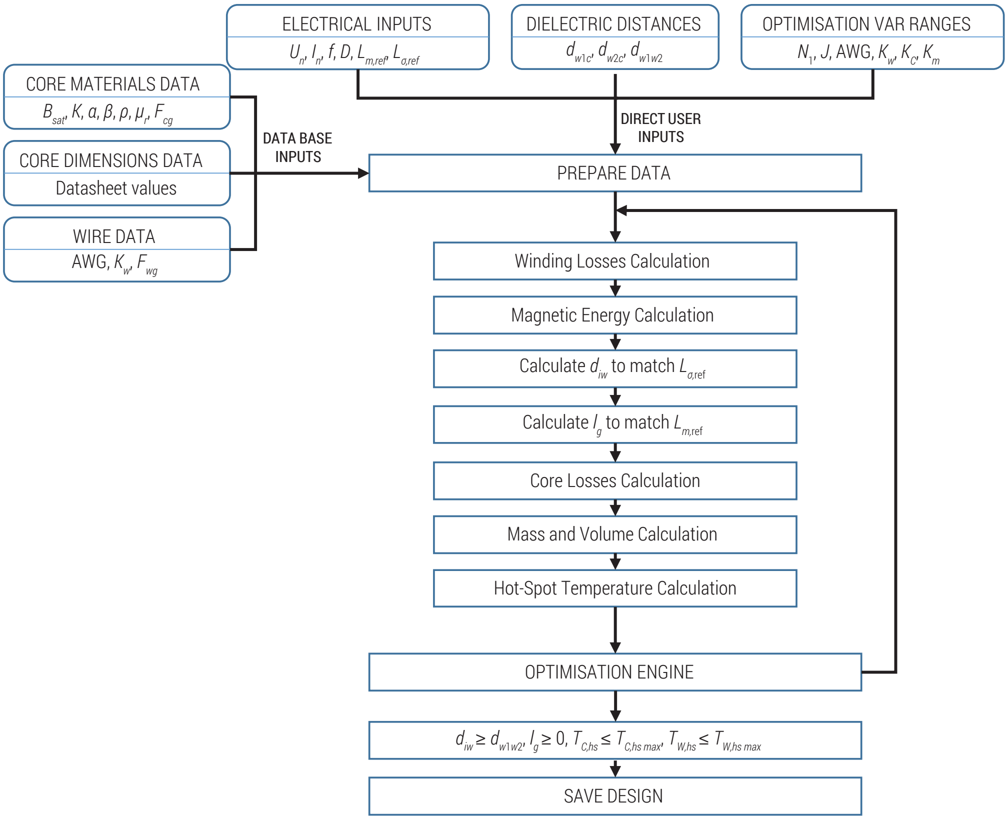

Fig. 6.1 Model-based brute-force MFT design optimization algorithm.

All the inputs are classified in two groups:

- database inputs - containing all the relevant component data-sheet specifications and
- direct user inputs - electric and dielectric parameter references and optimization variables ranges

All geometry ratios and relative field densities, as described by **Fig. 6.2** and **Tab. 6.1**, are considered as optimization variables. The function ”prepare data” generates the optimization space where each variation of these variables corresponds to a single fully defined potential MFT design. Each of these designs is processed, determining its characteristics and feasibility.

The minimal necessary dielectric distances can either be estimated under the assumption of homogeneous field (as recommended in standards) or a sophisticated local electric field SDDM model can be used - taking into account the over-voltages during the ringing transients and their effect on the local electric field maximums, as proposed in **Sec. 5.3**. According to the described models (**Secs. 4.3**, **4.4** and **5.2**), winding losses and magnetic energy density distribution are calculated. In case of the minimum leakage inductance requirement, the inter-winding dielectric distance is kept at the minimum required dielectric width. If a specific leakage inductance is needed, the dielectric clearance between the windings is reverse calculated, based on the magnetic energy density calculation, to match the reference leakage inductance, with respect to the minimum required dielectric width restriction.

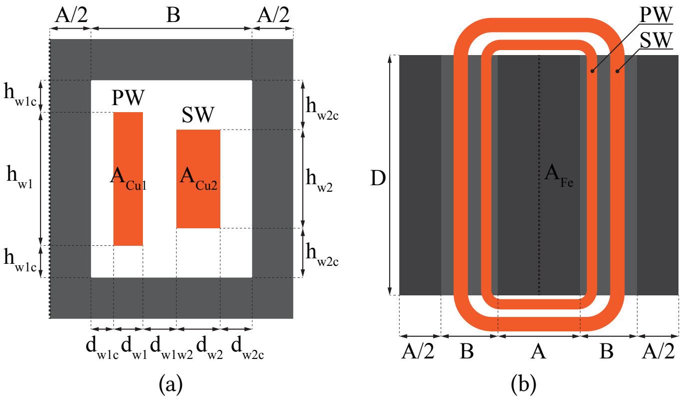

Fig. 6.2 Definition of generalized MFT geometry for parametric optimization: a) vertical cross section, where A_{Cui} denote the geometric winding cross-section area (copper and inter winding, turn-to-turn, insulation), whereas the total winding to winding (d_{w1w2}) and winding to core (d_{wic} and h_{wic}) distances include the solid insulation around the winding (in case of solid insulated) and air spacing; b) horizontal cross section, where A_{Fe} denotes the geometric core cross-section area

Tab. 6.1 Definition of optimisation variable ranges for parametric optimization according to generalized MFT geometry definition in **Fig. 6.2**

Optimization Variable	Definition	Range	Unit
PW number of turns	N_1	1 – 50	/
PW Current Density	$J_{m1} = \frac{I_n}{A_{Cu1}}$	0.5 – 6	$\frac{\text{A}}{\text{mm}^2}$
SW Current Density	$J_{m2} = \frac{I_n}{A_{Cu2}}$	0.5 – 6	$\frac{\text{A}}{\text{mm}^2}$
Magnetic Induction	$K_m = \frac{B_m}{B_{sat}}$	0.2 – 0.9	p u
PW Geometric Ratio	$K_{w1} = \frac{d_{w1}}{h_{w1}}$	0.05 – 0.5	p u
SW Geometric Ratio	$K_{w2} = \frac{d_{w2}}{h_{w2}}$	0.05 – 0.5	p u
Core Geometric Ratio	$K_c = \frac{A}{D}$	0.05 – 0.5	p u
American Wire Gouge	AWG	32	/

PW and SW refer to the primary and secondary winding, respectively

Air gap length is calculated to match the magnetization inductance reference, as given in **Sec. 4.5**. The mass and the volume are calculated based on the design dimensions and material properties. The core loss density is calculated (**Secs. 4.2** and **5.4**) and the hot-spot temperatures are estimated with the custom made detailed thermal network model that takes into account the 3D MFT structure and different material anisotropy - offering an optimal trade-off between the accuracy and computation speed, as proposed in **Sec. 4.6**.

Based on these results and using specific heuristics, the ”optimization engine” function guides the design selection process, detecting infeasible design space domains and avoiding wasting computational power on their processing. This allows for a significant increase in the execution speed. While these involve relatively complex logic, due to the multiple nested loops and constraints (one for each optimization variable), the main functionality can be explained in simple terms with the next couple of examples:

(i) The increase of current density loop is stopped for all designs with the same combination of all other optimization variables, once the maximum allowed winding or core hot-spot temperature has been reached. Note that the winding and core hot-spots are thermally coupled. Even though this coupling may be weak, depending on the specific construction, still the increase of the current density causes a further increase of the core hot-spot.

(ii) Same aforementioned strategy is employed for the magnetic induction loop.

(iii) In case there is an equality or inequality (less than a reference) constraint for the leakage inductance a complex logic constraint can be devised providing an upper bound for the number of primary winding turns (N_1) and a lower bound for the flux density individually, in the same way as described in (i). According to (4.40) and (4.42), the leakage inductance increases with the square of N_1 and linearly with the (MLT). Decrease of the flux density implies larger core cross-section and a larger (MLT) for an MFT design with the same combination of all other optimization variables. Therefore it is possible to use this constraint to further eliminate infeasible design domains.

Note that these kind of leakage inductance constraints are frequent for SRC applications, where low leakage inductance is required, or DAB, where external inductors are used. The case where a high leakage inductance needs to be integrated into the MFT for DAB applications is also simply handled with the equality constraint.

Finally, all the designs that pass the feasibility check are saved into a design database for post processing.

6.3 Optimal Design Selection

The proposed optimization methodology is applied to the Ferrite N87, rectangular Litz wire MFT design with electrical specifications, as summarized in **Tab. 8.2**. The maximum temperatures of the core and the windings are set according to the given material properties to 100°C and 150°C, respectively, while considering the ambient temperature of 20°C.

The proposed methodology consists of two steps. In the first step, all optimization variables are varied freely, in a mathematically arbitrary way, thus exposing all mathematically feasible designs, as shown in **Fig. 6.3** with circle markers, where the color-code corresponds to the highest hot-spot temperature within the windings (calculated during evaluation of that particular design). The upper boundary of the feasibility set plots represents the Pareto front, related to the trade-off between maximum achievable efficiency and power density. Its descending trend shows how efficiency must be sacrificed for the increase in power density. The lower boundary represents the thermal limit. It shows the implications of the size decrease on the cooling conditions and therefore the maximum acceptable

Tab. 6.2 MFT prototype reference electric specifications

P_n	100kW	V_1	750V	$L_{\sigma 1}, L_{\sigma 2}$	3.3 µH
f_{sw}	10kHz	V_2	750V	L_m	750 µH

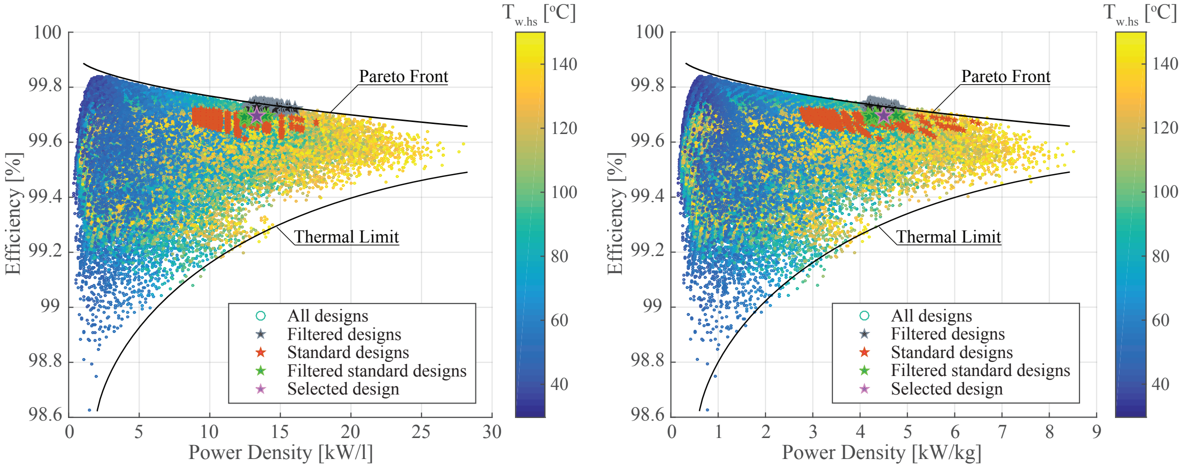

(a) (b)

Fig. 6.3 Plot of all possible MFT designs (around two million designs executed in approximately three hours) and filtered optimal designs according to specifications from **Tab. 8.2**: (a) Efficiency vs. volume power density; (b) Efficiency vs. weight power density. Color code corresponds to the highest hot-spot temperature within the windings.

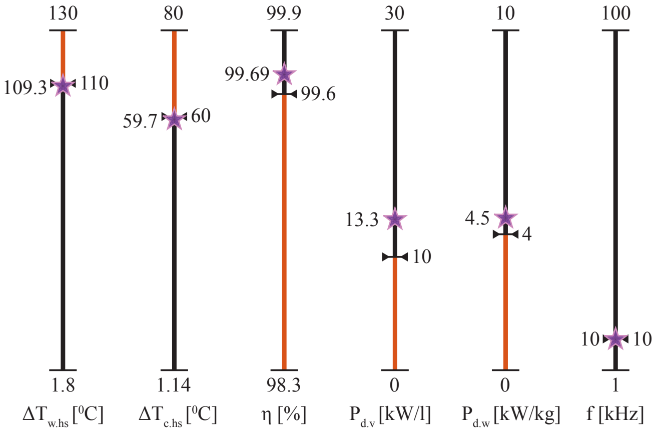

Fig. 6.4 Position of the optimal 10kHz MFT design within a multidimensional design space. Scales show the full range of possible MFT characteristics corresponding to the maximum feasibility set at 10kHz operating frequency. Performance filters, narrowing down the range of each MFT characteristic based on the desired specifications, are specified with black boundary markers and quantified with the value on the right side of each scale. Specifications of the optimal MFT design are depicted with the purple star marker and quantified with the value on the left side of each scale.

losses. In other words, it can be seen that an increase in the power density (decrease in size) of a design that is on a thermal limit is thermally feasible only if the losses are decreased - increased efficiency.

These designs are interactively filtered in terms of key performance indicators (maximum weight, volume and hot-spot temperatures, efficiency etc.) using sophisticated performance filters, such as illustrated in **Fig. 6.4**, allowing to arbitrarily shift and narrow down the filtered design domain by relaxing and tightening the corresponding constraints, as highlighted with black star markers in **Fig. 6.3**. This feature assumes expert user with knowledge of acceptable trade-offs for a given application.

In the second step, the filtered designs are analyzed against the available standard core and wire geometries and the design is re-optimized with fixed discrete values corresponding to the selected (most similar) components, as displayed in **Fig. 6.3** with red star markers. These designs are filtered in a same way as before, using the interactively defined performance filters, as highlighted with green star markers. The final design is selected from this set, based on various additional designer preferences, such as construction simplicity, experience etc., as highlighted with the purple star marker. The position of the optimal design within a multidimensional design space of interest is displayed in **Fig. 6.4**, together with the corresponding filter boundaries.

While the discussion about various Pareto optimal fronts is important, as it gives a good insight into the limitations of what is the maximum theoretically achievable performance and provides a good platform for comparison of different combinations of design choices and materials, when it comes to prototyping, it is important to take into account the safety margins, especially for the phenomena with high stochasticity such as natural convection cooling.

In that respect, it can be seen that the optimal design is not placed on the boundary of any of the parameter ranges. In order to achieve a thermally robust design, the maximum allowed core and winding hot-spot temperature rise constraint (filter) is tightened by a safety margin of 20°C, thus generating a new Pareto front between efficiency and power density. The most optimal design is selected on this new Pareto front by adjusting the efficiency and power density filters in a desired manner.

In this way, it is possible to individually take into account the different uncertainties for each MFT characteristic, caused either by the limited modeling accuracy or manufacturing and assembly imperfections. The result is a robust Pareto optimal solution that properly takes into account the

Fig. 6.5 A 3D render of the optimal MFT design, generated and selected according to the described design optimization procedure.

uncertainty of different models and processes relative to their importance for the given application.

Based on the generated design details, a 3D render of the selected optimal MFT design is displayed in **Fig. 6.5**. The realization and experimental verification of this design is presented in the following chapter.

6.4 Conclusion

It can be seen that in contrast to analysis of one or multiple sets of Pareto-optimal solutions, characteristic for formal optimization algorithms, this approach allows the designer to interactively select the best design trade-off in a very simple and intuitive way and provides great flexibility to choose between multiple design alternatives with very similar performance and specifications, but comprised of different components in case some are unavailable or too costly to be customized. Therefore, not only the characteristics of the MFT design itself, but also the whole design process and the prototype realization can be optimized.

With the described two step approach, the proposed method minimizes the sub-optimality gap between the theoretical and standard MFT designs, comprised of off-the-shelf components, and inherently provides a valuable insight into the positioning of the solutions utilizing specific hardware relative to all theoretically possible designs in a clear and intuitive way. This may be a very valuable input when it comes to component standardization, as it can clearly be seen what core or wire geometries are covering which MFT power, voltage and efficiency ranges.

7

Proof of Concept

This chapter describes in detail the realized 100kW, 10kHz *MFT prototype and the experimental verification of its electric, dielectric and thermal properties.*

7.1 MFT Prototype

Applying the described optimization process to a transformer with electric specifications shown in **Tab. 8.2**, an optimal MFT design is selected, as displayed in **Fig. 6.3** and marked with a star. The realized prototype is an air insulated and air cooled shell type MFT utilizing square litz wire for windings and N87 SIFERRIT U-cores.

Initially, the 3D CAD models are created in SOLIDWORKS, according to the resulting design specifications generated by the optimization algorithm, providing support to design and manufacturing process of coil formers. Primary and secondary winding each consist of eight turns of the square profiled (8.7x8.7 ± 0.2mm) copper litz wire with 1400 AWG 32 litz strands and a total copper crossection of 43.96mm^2, wound on the corresponding coil formers, as displayed in **Fig. 7.1(b)**. The primary and secondary coil formers have been produced using additive manufacturing process (3D printing) out of PA2200 high strength thermally resistant plastic. They have been designed and optimized, both to maximize the mechanical support strength and area for natural convective air cooling of the windings


(a) (b) (c)

Fig. 7.1 Optimal design resulting from the optimization algorithm: (a) Custom designed primary and secondary coil formers; (b) Prototype assembly; (c) The realized MFT prototype. Dimensions (H/W/D) with and without the resonant capacitor bank and the bushings are 235/340/330mm and 235/200/232mm, respectively.

with respect to the mechanical properties of the selected wire, as shown in **Fig. 7.1(a)**. The MFT core is made of 48 (12 x 4) SIFERRITE U-cores (UU9316 - CF139).

The realized 100kW, 10kHz MFT prototype with integrated resonant capacitor bank (distributed between primary and secondary winding) held by custom designed bus-bars, is displayed in **Fig. 7.1(c)**. Even though the prototype is almost identical as the 3D CAD design, there exist a couple of small (measured in parts of mm) differences in the geometry due to the limitations of the technological assembly process and material imperfections which effect the electric parameters of the MFT.

Considering brittle nature of ferrite materials and manufacturing tolerances in terms of the surfaces and dimensions, mechanical amortization is necessary at every surface of contact with another solid material. Due to this effect, there is a significant difference between the reference magnetizing inductance from **Tab. 8.2** and the one that was measured on the MFT prototype ($L_m = 750\,\mu\text{H}$) as the width of the interfacing pad maintaining the air-gap distance had to be chosen larger than calculated due to mentioned mechanical constraints.

On the other hand, bending of the large cross-section litz wire is not a simple task and relatively large bending radius, that is hard to achieve in the corner regions of the winding, needs to be considered in order to limit the bulging and twisting effect of the wire. Furthermore, there exists an offset in the winding placement of around 1mm compared to the 3D CAD and the wire itself has a slightly larger profile than stated in the data sheet. Consequently, the H field distribution in the window area and the leakage inductance are affected, and as a result, the measured leakage inductance ($L_{\sigma 1} = L_{\sigma 2} = 4.2\,\mu\text{H}$) is higher than the reference value from **Tab. 8.2**. Leakage inductance is very sensitive to imprecision of winding geometry, inter-winding dielectric spacing in particular, as the magnetic energy density is the highest in this area. That is why, even these tiny mechanical imperfections, in 1mm order of magnitude, can have a significant relative influence on the leakage inductance of MFTs for resonant converters where the reference value is typically very low, in a couple of µH order of magnitude depending on the rated power and voltage.

7.2 Experimental Verification

Several tests, under laboratory conditions, have been performed on the realized MFT prototype in order to verify design targets and operational performances.

7.2.1 Electrical Parameter Measurement

Before experimentally commissioning the MFT, its electric parameters were verified using the network vector analyzer Bode 100, as shown in **Fig. 7.2**. Plots of the measured and estimated total leakage inductance, based on the exact dimensions of the realized prototype geometry with its slight imperfections, are displayed in **Fig. 7.3(a)**. It can be seen that the developed hybrid leakage inductance model provides a much better estimation compared to direct application of the original Dowell's model, with less than 2.5% error in the entire frequency range.

Plots of the measured and estimated total MFT series resistance are displayed in **Fig. 7.3(b)**. It can be seen that the estimation follows the measured result quite well with relative error less than 5% at 10kHz and 20% in the entire frequency range. It is important to mention that the series resistance

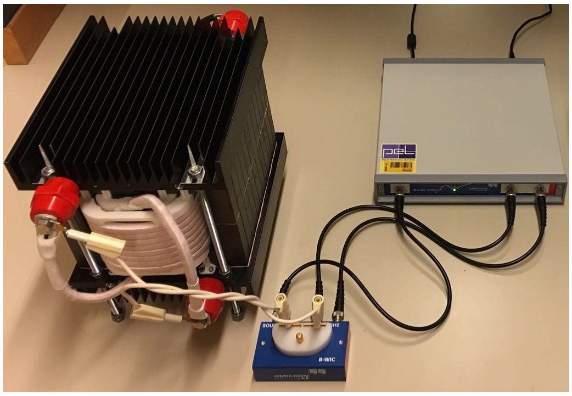

Fig. 7.2 Measurement of the electric parameters of the MFT

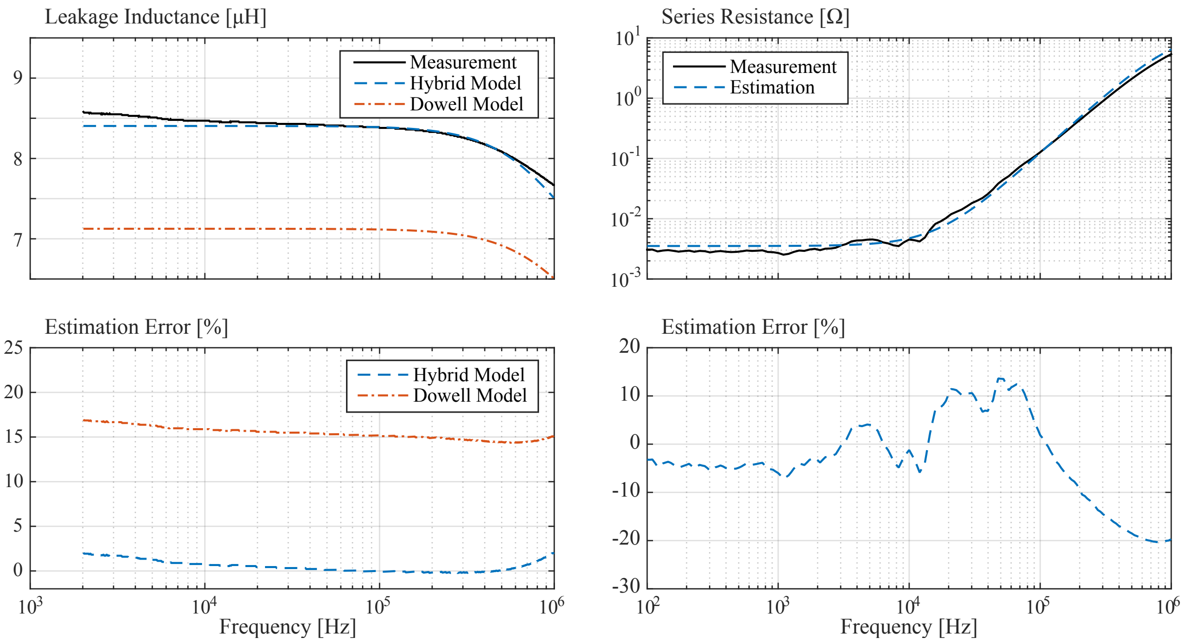

(a)

(b)

Fig. 7.3 (a) Top: plots of total leakage inductance ($L_{tot} = L_{\sigma 1} + L_{\sigma 2}$) measurement (black), estimation with hybrid model (blue dashed line) and estimation with Dowell model (red dash-dot line); Bottom: plots of total leakage inductance estimation error of the Hybrid (blue dashed line) and Dowell (red dash-dot line) model, referred to the measurement. (b) Top: plots of total MFT series resistance measurement (black) and estimation (blue dashed line); Bottom: plot of total MFT series resistance estimation error, referred to the measurement

of the connecting cables has been measured a priory and its effect on the MFT series resistance measurement has been canceled.

The distribution of winding and core losses of the realized MFT prototype, at nominal operation (100kW at 10kHz), are summarized in **Tab. 7.1**. Since, it is not possible to properly measure the MFT losses without a dedicated calorimetric setup, winding losses are calculated based on the nominal resonant current RMS and AC resistance measurement at operation frequency of 10kHz, whereas core losses are only estimated.

Tab. 7.1 MFT losses at 10kHz, 100kW operation

	R_σ[mΩ]	P_σ[W]	P_c[W]
Estimated	4.74	154.2	150.5
Measured	4.59	149.6	/

7.2.2 Electrical Measurements in a Resonant Test Setup

To carry out the electrical tests on the MFT prototype, a full power rated resonant test setup has been assembled. The electrical scheme of the test setup and its physical layout inside the protective cage are shown in **Fig. 7.4** and **Fig. 7.5(a)**, respectively. The setup consists of two H-bridge modules, one actively switched and the other operating as a diode rectifier, with their corresponding DC-bus capacitors. The resonant tank comprised of the MFT and the distributed resonant capacitors (C_{r1} and C_{r2}) is inserted between two converters and two DC sources, one operated in voltage (U_{DC1}) and the other in current (I_{DC}) control mode are used. The test setup is operated as a resonant converter at the constant frequency f_{sw} = 10kHz and with the constant duty cycle D = 0.5. Positive ends of the DC-buses on the primary and secondary side are connected, whereas their negative ends

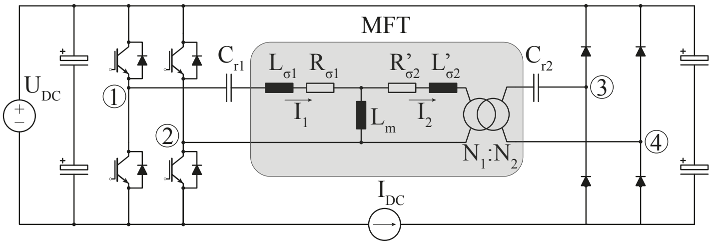

Fig. 7.4 Electrical scheme of the back-to-back resonant test setup

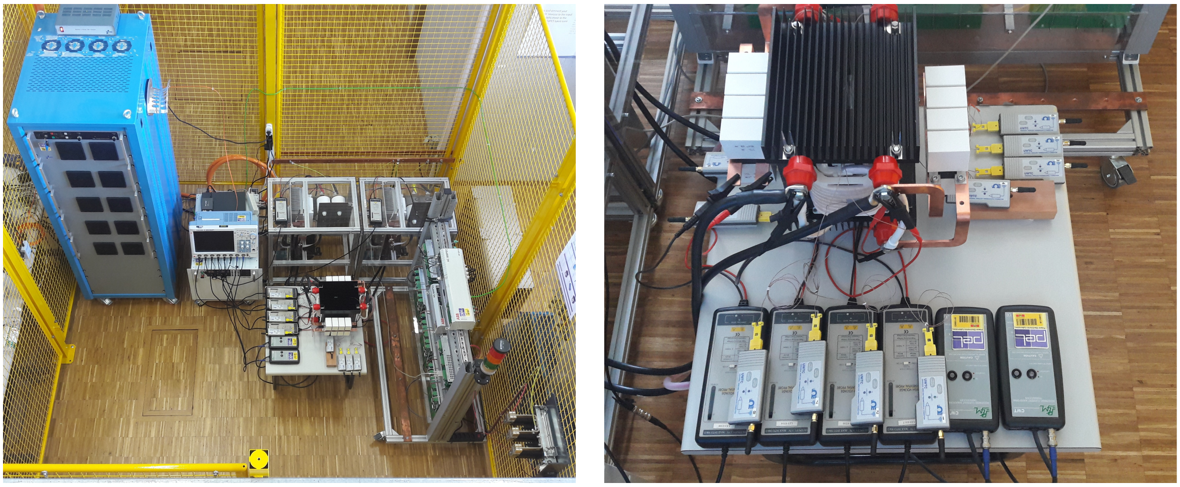

(a)

(b)

Fig. 7.5 (a) Layout of the back-to-back test setup within the protective cage. (b) MFT equipped with thermocouple probes for hot-spot temperature measurement. A list of the used equipment is provided in **App. A**.

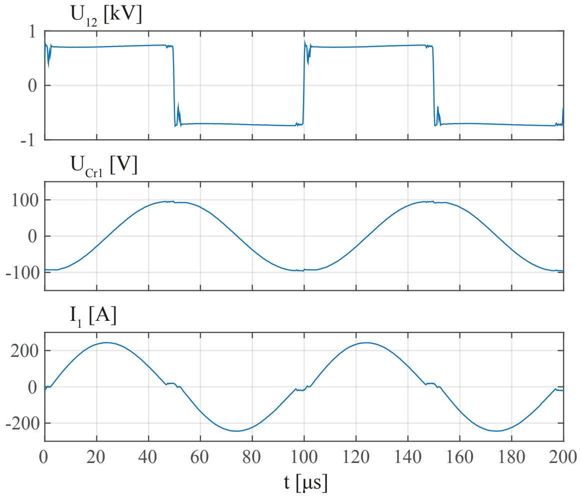

(a)

(b)

Fig. 7.6 Measured waveforms on the primary (a) and secondary (b) MFT side at nominal power: voltages on the inputs of the resonant tank (top), voltages on the resonant capacitors (middle) and resonant currents (bottom)

are connected through a current source (I_{DC}) thus allowing the circulation of the energy from the secondary side back to the primary side DC-bus, as displayed in **Fig. 7.4**.

Both primary (C_{r1}) and secondary (C_{r2}) capacitor of the distributed resonant capacitor bank are realized as a parallel connection of eight (7x5 µF + 1x2.5 µF) AC film capacitors, held by bus-bars, giving a total resonant tank capacitance of 18.75 µF and consequently the resonant tank frequency of f_0 = 12.7kHz. Therefore, the desired sub-resonant converter operation is achieved, providing soft switching turn-on for the primary side switches and zero current switching for the secondary side diodes.

The actual H-bridges are realized by utilizing two phases of two three-phase SEMIKRON Skiip modules, as seen in **Fig. 7.5(a)**. The primary side H-bridge is actively controlled with PWM signals generated by the ABB AC 800PEC high performance controller where all relevant control functions are implemented in MATLAB Simulink and executable code is generated using real-time code generation. All devices within the protective test cage, two DC sources, 8-channel oscilloscope, and AC 800PEC controller, as displayed in **Fig. 7.5(a)**, are connected through their ethernet connection to the multi-port active switch communicating with the PC via the optical cable thus ensuring safety and complete electrical decoupling of the operator from the high power test setup.

The voltages on the AC side of the H-bridge converter (U_{12}) and the diode rectifier (U_{23}) are measured together with the resonant capacitor voltages on both the primary (U_{Cr1}) and secondary (U_{Cr2}) side, as well as the primary (I_1) and secondary (I_2) resonant currents. Furthermore, the DC-bus voltages on each Skiip module, and the output AC currents of the two converters are measured with additional sensors and used to implement safety features (e.g. over-voltage and over-current protection) within the controller software. Voltages and currents of both DC sources are monitored to evaluate the power injected into the test setup, covering the total losses during the operation.

The MFT is equipped with wireless thermocouple probes at various accessible expected hot-spots

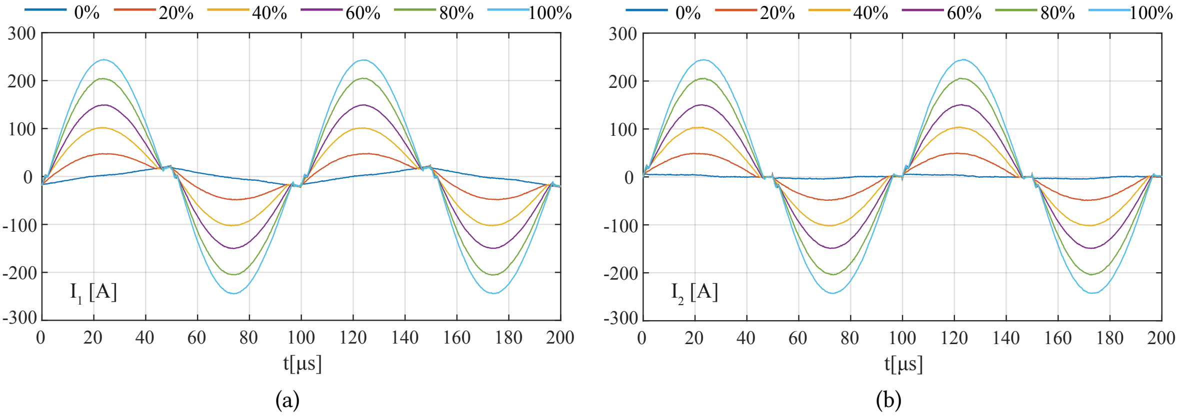

Fig. 7.7 Measured current waveforms on the primary (a) and secondary (b) side of the MFT at different loading conditions in range from 0% to 100% of the rated power

within the core and the windings for constant thermal monitoring, as displayed in **Fig. 7.5(b)**, whereas the temperature of the outer surfaces is monitored with the thermal camera.

The measured voltage and current waveforms, from the primary and secondary side of the MFT at nominal power operation, are displayed in **Fig. 7.6(a)** and **Fig. 7.6(b)**, respectively. The top plots show the voltage waveforms on the output of the H-Bridge (U_{12}) and the input of the diode rectifier (U_{34}). Primary side voltage is regulated by DC voltage source U_{DC1} to 750V. The middle plots show the voltages on the primary (U_{Cr1}) and secondary (U_{Cr2}) side resonant capacitors, while bottom plots show the primary (I_1) and secondary (I_2) resonant current waveforms. One can observe that resonant tank current and capacitor voltage are in quadrature, without any distortion, indicating well balanced operation. Resonant current plots show that the resonant frequency corresponds to the calculated value (f_0) and that the soft-switching is achieved. The maximum switch-off current of the IGBTs is therefore limited by the peak value of the magnetization current ($I_{m_{max}} = 25A$).

Plots of the primary and secondary resonant currents, under various loading conditions ranging from 0% to 100% of the rated power, are provided in **Fig. 7.7(a)** and **Fig. 7.7(b)**, respectively. Under no-load conditions, only the magnetizing current is present in the circuit, and as the power transfer is increased, typical resonant waveform is established with rms value proportional to the operating power level. Due to inability to reduce the dead-time below the minimum 3 µs set by the gate driver, it can be observed from **Fig. 7.6** that a minor and incomplete loss of the zero voltage switching occurs at 100kW operating point. This was not a major concern during MFT testing, considering that the resonant test setup was of sufficient ratings, and the objective of the thesis is not on the converter optimization.

The total losses of the whole resonant test setup can be calculated from the voltage and current readings on the two DC power supplies U_{DC1} and I_{DC}. The total power injected into the setup at the nominal power was measured as 2.9kW, indicating the overall resonant converter efficiency of 97.1%. This is a reasonable result, taking into account that, with the exception of the MFT, the setup was not optimized for the given operation. As earlier mentioned, it is not possible to properly measure the MFT losses without a dedicated calorimetric setup. On the other hand, it is hard to accurately separate the total converter losses using the data from the conducted tests, thus making the exact estimation of the MFT efficiency difficult.

However, an estimation of its low bound can be made by calculating the total semiconductor losses in the setup, considering well defined operating conditions. These account for approximately 2.2kW (this does not include the DC link and resonant capacitor losses). Thus, the lower bound for the MFT efficiency can be estimated to be above 99.3% at rated operating conditions. Note that this is not the estimation of the actual MFT efficiency, but only of its low bound where many additional losses remain unaccounted for. Moreover, the contribution of the switching losses of the IGBTs to the total losses is underestimated as a result of the direct extrapolation of the switching loss curve (of the devices optimized for hard switching) to the very low switch-off current domain, characteristic for the given soft switching operation. Properly accounting for the actual switching losses would further raise this lower bound towards the actual MFT efficiency.

7.2.3 Thermal Measurements

To verify the thermal characteristic of the MFT, a nine hour thermal run was performed, with results presented in **Fig. 7.8**. The MFT is first operating at no load, with nominal voltage excitation until the steady state is reached. As characteristic for this operation where only the core losses are present, it can be seen that the core has the highest temperature, whereas the windings are predominantly heated through the coupling thermal resistances (**Fig. 4.11(b)**), considering low primary winding magnetization current, as already presented in **Fig. 7.7**.

Following prolonged no load operation, the MFT is loaded with the nominal power, where both core and winding losses are at their maximal value. It can be seen that the winding temperature is now

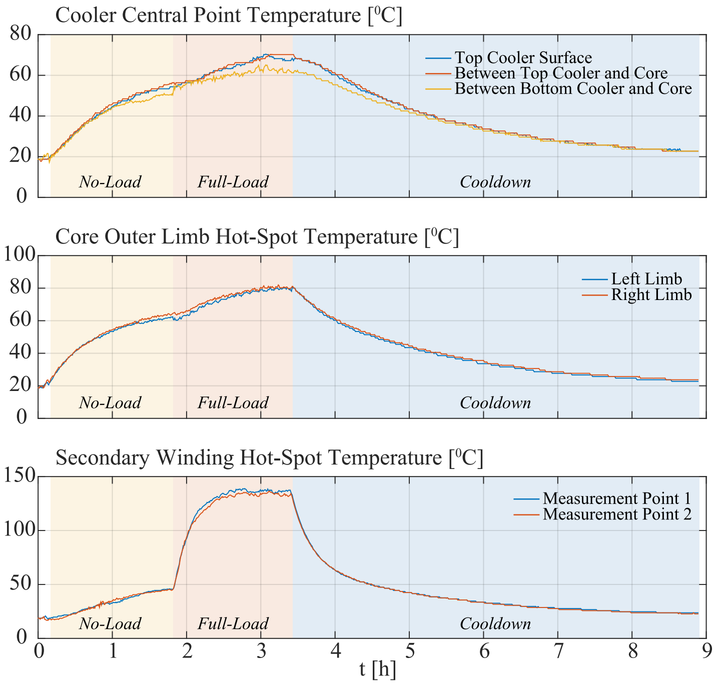

Fig. 7.8 Plots of the thermocouple probe measurements during the nine-hour thermal run. Measurement points 1 and 2 correspond to hot-spots of the portions of the winding inside and outside of the core window area, respectively.

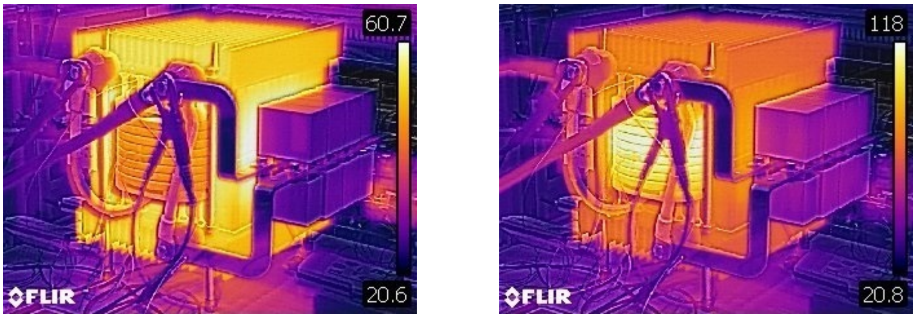

(a)

(b)

Fig. 7.9 Thermal camera images of the MFT: (a) in no-load steady state excited with nominal voltage input from primary side; (b) in full-load steady state;

the highest, in compliance with thermal design expectation, as given in **Tab. 4.2**. The measured core and secondary winding temperatures are slightly higher than estimated, but still within the safe operating limits. Given the good correlation between FEM and analytical model estimations, it can be concluded that this discrepancy is mainly due to the low accuracy of the applied empiric natural convection formulas. Thermal camera images, depicting the MFT surface temperatures at the two described steady states, are given in **Fig. 7.9**.

7.2.4 Dielectric Withstand Test

Finally, to verify the achieved voltage insulation levels, the MFT prototype was tested in a high voltage test setup (able to generate voltages up to 100kV) displayed in **Fig. 7.10**, normally used for AC dielectric withstand and partial discharge tests. The tests were carried out by applying the voltage: i) between the primary and the secondary winding; ii) between the secondary winding and the conductive parts of the MFT (top and the bottom heat-sinks and the vertical studs). The voltage profile has been set considering recommendation outlined in safety standards (e.g. IEC 60664-1). The critical partial discharge level (10pC) has been recorded at 4kV AC, applied between the primary and the secondary windings, with measurement results shown in **Fig. 7.11** (obtained with Omicron MPD600 system).

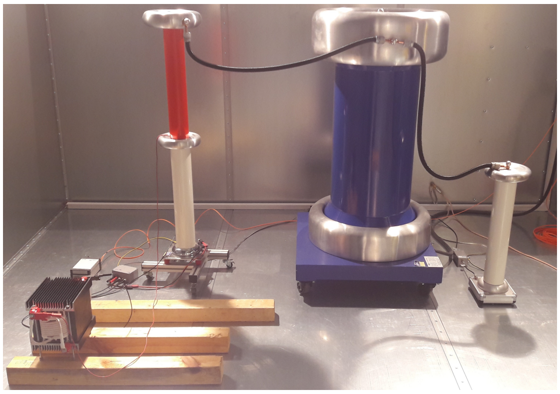

Fig. 7.10 MFT dielectric withstand test

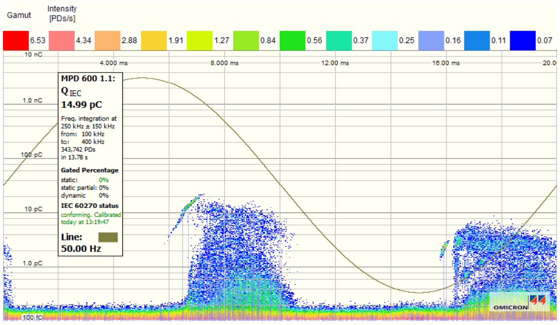

Fig. 7.11 Plot recorded during the partial discharge testing between primary and secondary winding for a standard PD test profile (front V = 6kV and flat back V = 4kV)

7.3 Conclusions

A 100kW, 10kHz, air insulated and air cooled shell type MFT prototype has been realized utilizing square litz wire for windings and N87 SIFERRIT U-cores. The prototype was subjected to thorough testing, including: electric parameter identification, PD test, loading test and a 9-hour thermal run within the realized back-to-back resonant test setup. The measurement results have confirmed the high fidelity of the developed modeling and the practicality of the proposed design optimization methodology - the custom set safety margins for the core and winding hot-spot temperatures that allowed the safe operation (below the maximum allowed material temperatures) at nominal power, regardless of the slight temperature estimation errors. It can be concluded that the proposed design optimization methodology, powered by the developed advanced models, provides a powerful robust-design framework.

8
Sensitivity Analysis of MFT Design

This chapter provides a detailed analysis of the potential for MFT scaling on the SST level, considering both the readily available Si power semiconductor devices and the emerging SiC with extended blocking voltages and operation frequency range. Special focus is put on the impact of the selected power semiconductor modules and the resulting converter modularity and operation frequency. The case study is performed on a typical 0.5MW 10kV *input series output parallel SRC based converter topology example. Interesting trends are revealed that can aid the overall solid state transformer design optimization.*

8.1 Introduction

As already discussed, novel high-power medium-voltage converter technologies offering galvanic insulation are needed to support the development of the emerging medium voltage DC (MVDC) grids and further improve performances in various other applications such as traction [111]. With the recent advancements in the power semiconductor industry, resulting in faster and more efficient switches with extended voltage and current capabilities, these converters, SSTs or PETs, have become increasingly attractive.

Due to the limited blocking voltage capabilities of the existing power semiconductors, most of the proposed solutions from the literature employ some sort of an input series output parallel (ISOP) structure, featuring multiple identical converter cells, to allow the connection to MV, as displayed in **Fig. 8.1(a)**. The most popular ISOP converter structures are based on multiple stages of either series resonant converter (SRC) or dual active bridge (DAB) topologies, as shown in **Fig. 8.1(b)** and **Fig. 8.1(c)**, respectively. As can be seen, besides the power semiconductor modules, the central component of any such switched-mode DC-DC power supply topology is the medium frequency transformer (MFT), providing both the galvanic insulation and input-output voltage matching.

Moreover, different DC-DC converter topologies impose different requirements for MFT electrical parameters and operation conditions. The analysis presented in this chapter focuses on different implications on the MFT design for a SRC based ISOP DC-DC converter structure, as displayed in **Fig. 8.1**. Note that the conclusions are transferable to any AC or DC input-output combination of the ISOP structure, as the AC input or output would only imply the addition of active front-end or inverter stage to the SRC cell shown in **Fig. 8.1(b)** without significantly influencing the MFT specifications. The only difference being the type of experienced dielectric stress: high voltage DC with superimposed high frequency AC PWM in case of DC-DC/AC SST and low frequency high voltage AC with superimposed high frequency AC PWM in case of AC-DC/AC SST, as illustrated in **Fig. 8.2**.

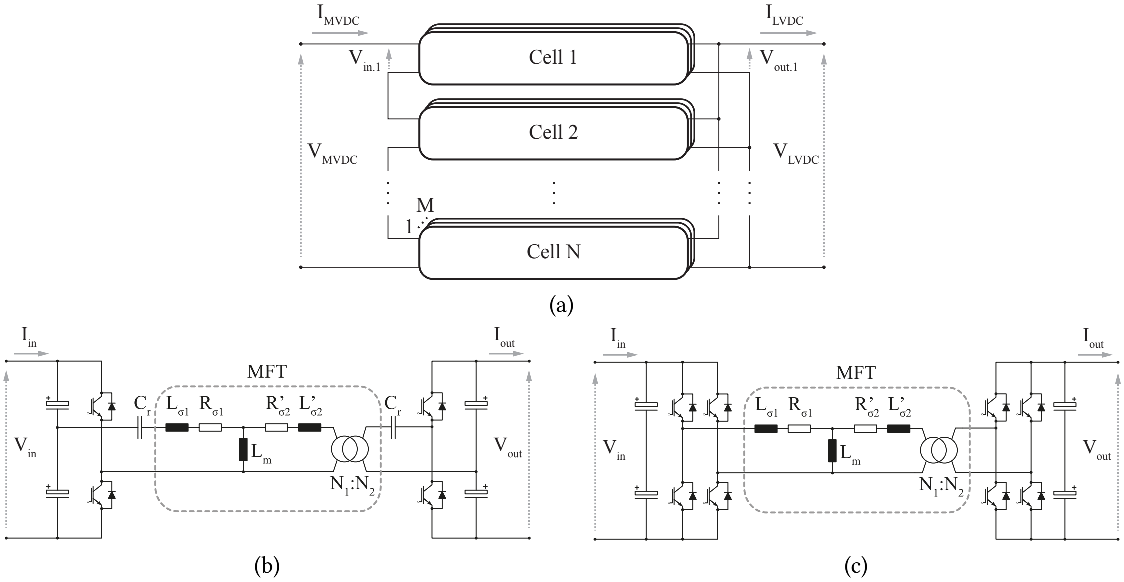

Fig. 8.1 (a) ISOP connection of DC-DC converter topologies commonly used within SSTs: (b) SRC converter (c) DAB converter

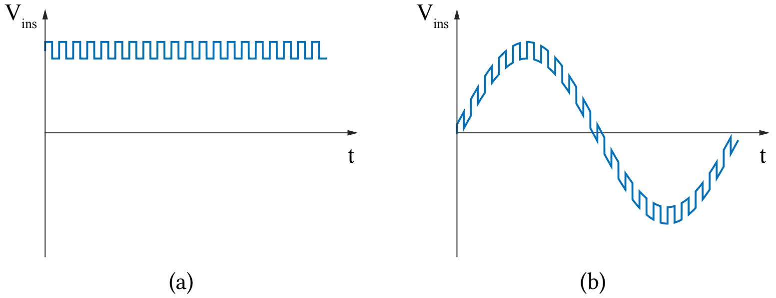

Fig. 8.2 Typical voltage stress experienced by the MFT insulation operating within an ISOP SST: (a) High-voltage DC with superimposed high-frequency AC PWM characteristic for DC-DC/AC SST; (b) Low-frequency high-voltage AC with superimposed high-frequency AC PWM characteristic for AC-DC/AC SST

Compared to the mentioned state of the art, dealing with various challenges of the MFT design for defined requirements [28], [31], [42], [43], [46], [47], [100], this work looks into the MFT design optimization from the aspect of the whole converter. Design degrees of freedom of the ISOP converter, as shown in **Fig. 8.1(a)**, and their impact on the resulting MFT specifications are analyzed. While an analysis, attempting to find the optimal number of cascaded cells of the AC-DC ISOP converter from the aspect of the MVAC input active rectifier stage has been performed in [112], this chapter tackles a similar problem from a DC-DC converter cell point of view. Considering the most relevant materials and design choices reoccurring in the literature, the MFT design is optimized in function of the ISOP converter modularity. A comparative analysis of various design choices is performed in terms of efficiency and power density, providing an overview of the dominant solutions and insight into the overall optimal design choice coordination.

As already described throughout this thesis, an MFT is a complex system with coupled multi-physics which makes understanding the effects of certain design changes rather abstract and difficult to grasp. Similar to the qualitative analysis of the MFT scaling laws, as provided in **Sec. 2.2**, this chapter discusses in detail the trends and different design outcomes in a quantitative sense using the described and verified design optimization methodology, as given in **Chap. 6**. The impact of different parameters is analyzed in a structured and intuitive manner thus exposing different design trade-offs, potential gains and expectation limitations.

8.2 Converter Design

8.2.1 Selection of the number of cells

Depending on the electrical ratings, nominal power and input-output voltages, the number of DC-DC converter cells connected in ISOP configuration (N), as shown in **Fig. 8.1**, represents a design choice related to voltage class of selected semiconductors. Moreover, each of the cells can as well be realized as a parallel connection of multiple cells (M), depending on the current ratings of selected semiconductors. All of the cells are equally sharing the high voltage at MV side, high current at the low voltage side and power, according to (8.1), (8.2) and (8.3), respectively.

$$V_{in} = \frac{V_{MVDC}}{N} \quad \text{and} \quad V_{out} = V_{LVDC} \tag{8.1}$$

$$I_{in} = \frac{I_{MVDC}}{M} \quad \text{and} \quad I_{out} = \frac{I_{LVDC}}{NM} \tag{8.2}$$

$$P_n = \frac{P_{tot}}{NM} \tag{8.3}$$

The feasible alternatives are limited by the voltage and current ratings of the available semiconductors. The maximum blocking voltage of the selected semiconductor devices on the primary side (V_b) and current ratings of the semiconductors on the secondary side (I_{max}) must satisfy the relation (8.4).

$$V_b > \frac{V_{MVDC}}{uN} \quad \text{and} \quad I_{max} > \frac{I_{LVDC}}{NM} \tag{8.4}$$

Various design alternatives, depending on the selected semiconductor blocking voltages are summarized in **Tab. 8.1**. This table considers the standard ratings of the contemporary semiconductor devices readily available on the market as well as the projection for the emerging future semiconductors with extended blocking voltage capabilities, such as the 10kV SiC [113], marked in gray, and mostly available as engineering samples.

As can be seen, there exist various design alternatives, utilizing different number of DC-DC converter cells with differently rated semiconductors to share the high input voltages and output currents. Each of these solutions imposes different electrical ratings on the DC-DC converter cell resulting in different sizing of the passive components.

8.2.2 Cell Design

The design of the resonant tank of the SRC, as shown in **Fig. 8.1(b)**, can be performed based on the desired operating mode and selected quality factor (Q). Using the first harmonic approximation, the equivalent nominal-load resistance refereed to the primary side of the transformer can be calculated according to (8.5).

$$R_{ac1} = \frac{2n^2 V_{out}^2}{\pi^2 P_n} \tag{8.5}$$

The reference values for the series resonant capacitance and inductance can be calculated with (8.6) and (8.7), respectively

$$C_r = \frac{1}{2\pi f_0} \frac{1}{QR_{ac1}} \tag{8.6}$$

$$L_r = \frac{1}{2\pi f_0} QR_{ac1} \tag{8.7}$$

where

$$f_0 = 1.2 f_{sw} \tag{8.8}$$

is the desired resonant frequency. It is set 20% above the switching frequency to achieve sub-resonant operation, where the turn-off current of the primary side switches is limited to relatively small MFT magnetizing current, whereas the secondary side diode current is reduced to zero, thus eliminating reverse recovery losses. Quality factor is set to 0.1 to ensure a resonant tank characteristic that will result in a large zero voltage switching (ZVS) region within the sub-resonant frequency range, hence ensuring the soft turn-on of the active switches at the intended operating point.

Tab. 8.1 Number of Cascaded DC-DC Converter Cells Depending on Selected Semiconductor Blocking Voltage for V_{MVDC} = 10kV and Maximum Switching Frequency

V_b [kV]	N	V_{in} [kV]	u [p u]	f_{sw} [kHz]
1.7	11	0.91	0.53	25 (50)
3.3	6	1.67	0.51	10
4.5	4	2.5	0.56	5
6.5	3	3.33	0.51	1
10	2	5	0.5	/
20	1	10	0.5	/

u is the semiconductor blocking voltage utilization factor, normally up to 50%-60% [114]. Marked in gray are the emerging SiC based semiconductors with extended blocking voltage capabilities (not yet fully commercially available). Shown in brackets are the SiC modules already available on the market. While switching frequencies of 6.5kV modules are typically below 1kHz, the resonant operation allows for a frequency increase up to 1 – 1.5kHz [115].

The reference magnetizing inductance of the resonant tank is designed to limit the maximum magnetizing current to the desired active switch turn-off current (I_{off}) according to equation (8.9).

$$L_m = \frac{V_{out}n}{8f_{sw}I_{off}} \tag{8.9}$$

Combining (8.1), (8.2),(8.3), (8.5), (8.7), (8.8) and (8.9), the reference parameters of the MFT within each SRC cell, leakage and magnetizing inductance refered to the primary side, can be expressed in function of the total converter ratings and the number of cells with (8.10) and (8.11), respectively.

$$L_r = \frac{Q}{1.2\pi^3}\frac{MV_{MVDC}^2}{Nf_{sw}P_{tot}} \tag{8.10}$$

$$L_m = \frac{1}{8I_{off}}\frac{V_{MVDC}}{Nf_{sw}} \tag{8.11}$$

The last two equations show the influence of both design variables, operation frequency and modularity, on the reference leakage and magnetization inductance of the MFT, imposed by the converter.

8.3 Quantitative Analysis of the MFT Design Trade-Offs

As already discussed in **Tab. 2.1**, there are many coupled effects that influence the scaling of the MFT, making it a rather difficult task to map the domain of possible designs or fairly assess the design improvement potential of each design choice on its own. In that respect this section proposes a method of analyzing the MFT design trade-offs in an integral manner, using the developed and verified model-based MFT design optimization tool. The focus of the analysis is on the influence of the ISOP converter modularity on the maximum achievable MFT characteristics for various design choice alternatives. The electric specifications of the ISOP converter, chosen for the case study, are summarized in **Tab. 8.2**.

Tab. 8.2 ISOP Converter Electric Specifications

P_{tot}	V_{MVDC}	V_{LVDC}
500kW	10kV	750V

8.3.1 Scope Of The Analysis

The considered design is a litz wire, natural air convection cooled shell type MFT with enhanced cooling at the top and bottom surfaces of the core, as shown in ??. While the main transformer structure is fixed, two different core materials and insulation strategies, typically reoccurring in the literature, are analyzed.

Tab. 8.3 Core Material Characteristics at 100°C [34], [43], [59]

Core Material	B_{sat} [T]	K [kW/m^3]	α	β	ρ [kg/m^3]	λ [W/mK]
Si-Ferrite N87	0.39	$1.6 \cdot 10^{-3}$	1.42	2.16	4850	4
Nanocrystalline	1.17	$3.6 \cdot 10^{-5}$	1.64	2.10	7330	1.5 (8)

Two different thermal conductance values, in normal and parallel direction to nanocrystalline sheets are considered to properly take into account the anisotropy of the nanocrystalline cores

Tab. 8.4 Dielectric Material Characteristics [46]

Material	V_d [kV/mm]	k_s	ρ[kg/m^3]	λ[W/mK]
Air	3	4	0	/
Epoxy	45	3	500	0.25

k_s is a dielectric safety margin multiplicative factor

The considered core materials are Si-Ferrite N87 and nanocrystaline, as the most common materials of choice for MFT prototypes documented in the literature, depending on the switching frequency range. The assumed material characteristics, used in the study are summarized in **Tab. 8.3**.

ISOP connection requires for each MFT to be insulated for full working voltage of 10kV. This requirement, combined with the high frequency stress with high dV/dt makes the proper MFT insulation coordination a rather challenging problem. Two different insulation strategies are considered: air insulation (litz wire winding in the air [28]) and solid insulation (litz wire winding cast in epoxy resin in the air [46]). Considered dielectric characteristics of the mentioned materials are summarized in **Tab. 8.4**.

Proper MV MFT insulation coordination is not a straight-forward task and it depends on many different details (e.g. local electric field grading) which are not easy to take into account at the optimization stage. However, for design comparison purposes, without the loss of generality, it can be claimed that, depending on the chosen insulation material, higher blocking voltage requirements (V_i) will yield larger dielectric distances (d_i), proportional to the corresponding dielectric strength (V_b) according to

$$d_i \approx k_s k_{pd} \frac{V_i}{V_b} \tag{8.12}$$

where k_{pd} is a PD test standard voltage front multiplier from the IEC 60664-1 international standard and ($k_s > 1$) is a multiplicative safety margin factor that takes into account the imperfections, degradation and pollution in non-laboratory conditions (it is down to a designer to decide). Especially high safety margin values must be taken into account for any design with air due to the possibly high dust or moisture content causing local field anomalies that can lead to Partial Discharge (PD).

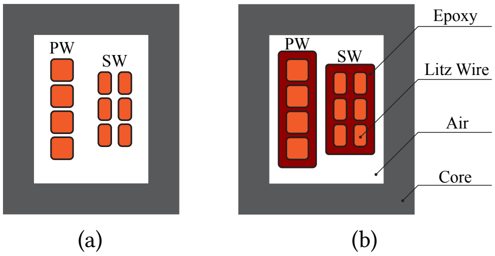

Fig. 8.3 Two considered insulation concepts: (a) Square litz wire windings without any added external insulation besides the strand enamel and outer silk binder, held in place with a coil former; (b) Square litz wire windings separately cast in epoxy resin, mechanically held by the the strength of the cast itself

Air insulated design assumes litz wire windings without any added external insulation besides the strand enamel and outer silk binder, as shown in **Fig. 8.3(a)**. In order to maximize the cooling efficiency, they are mechanically held by a specially designed coil former (not visible in **Fig. 8.3(a)**) that allows natural air convection from almost the entire winding surface, as presented in [28]. The minimum air dielectric distances (clearances) are calculated according to (8.12). Similarly, solid insulated design assumes litz wire windings, each separately cast in epoxy resin to minimize the mechanical stress on the cast due to the thermal expansion of different parts [46], mechanically held by the the strength of the cast itself, as displayed in **Fig. 8.3(b)**. Even though the minimum width of the epoxy coating is calculated for full voltage according (8.12), additional small air clearances are assumed to maximize the natural air convective cooling and allow for easy assembly.

Note that despite being an interesting design alternative, oil based designs have not been considered in this study as they in general require additional expansion vessels and radiators [47] or some other type of external heat exchanger [36] which make a fair design comparison very difficult, unless these are properly taken into account as well.

All of the aforementioned design alternatives are systematically analyzed and compared in terms of the key performance features.

8.3.2 Method of Analysis

A model-based brute-force MFT design-optimization algorithm, capable of generating the sets of all feasible MFT designs for the given electric and dielectric specifications, as already presented and experimentally verified in detail in **Chaps. 6** and **7**, respectivelly, is used for the purposes of this analysis to map various design choice influences and trade-offs.

For each possible number of cascaded DC-DC converter cells (N) from **Tab. 8.1**, core and insulation material combination, maximum feasible MFT design sets are generated for a family of frequencies in range from 0.5kHz to 50kHz in a logarithmic scale, as shown in **Fig. 8.4**. A comprehensive comparative analysis of these results is presented next, outlining the main effects and trade-offs while taking into account both the readily available power semiconductor modules on the market and exploring the potential benefit of the emerging future devices with extended blocking voltage and operating frequency range, as given in **Tab. 8.1**.

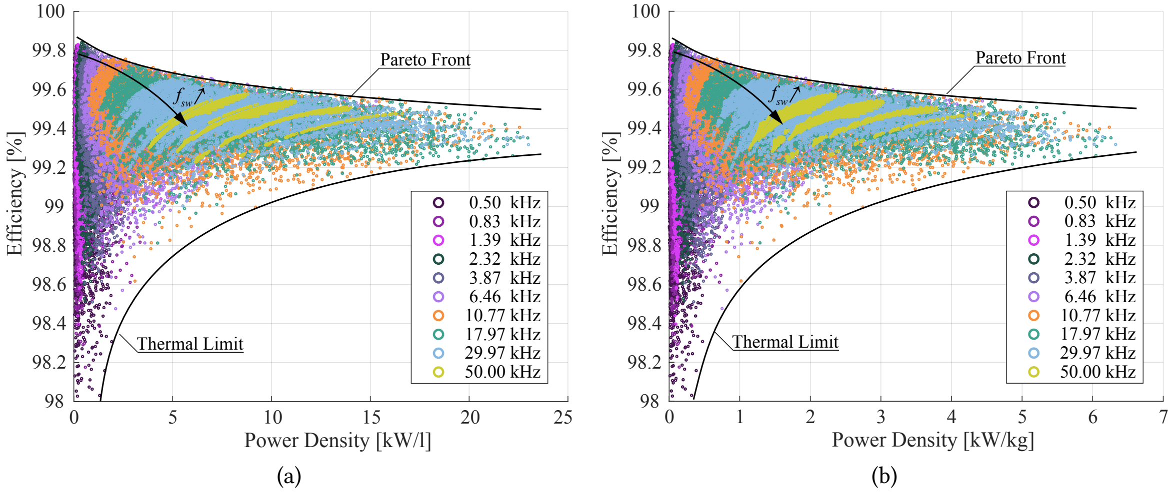

Fig. 8.4 Efficiency versus volumetric (a) and gravimetric (b) power density plots of all mathematically feasible MFT designs generated with design optimization algorithm for $N = 11$, $M = 1$, Si-Ferrite, Solid (around 12 million designs, uniformly down-sampled to 66000 for faster rendering). Designs are organized in color groups based on operating frequency. The MFT volume is defined as the minimum box which can be put around the active part of the transformer, core and the windings, as recommended metric for design comparison [49].

8.4 MFT Design Analysis

An example of the maximum feasible MFT design set, generated with the algorithm for $N = 11$, $M = 1$, Si-Ferrite, solid insulated MFT, is displayed in efficiency versus volumetric and gravimetric power density plots, as given in **Fig. 8.4**. These plots reveal the trend related to the influence of frequency increase on the disposition of the feasible MFT designs. The upper boundary of the feasibility sets represents the Pareto front corresponding to the trade-off between the efficiency and power density. On the other hand, the lower boundary is set by the thermal limitations, showing how, at the set boundary, a smaller design must have a higher efficiency in order to compensate for the decrease of the cooling surfaces and remain within the defined temperature limitations.

It can as well be seen how the feasible design sets at different frequencies reach the maximum achievable efficiency point at different power densities. The loss density within the core and the windings is higher at higher frequencies and therefore the increase of efficiency cannot be achieved by mere increase of their respective cross-sections. Therefore, with the increase of frequency, where additional loss density associated to high frequency effects is higher, maximum efficiency points are lowered and shifted towards higher power densities. Analyzing only the efficiency versus power density trade-off for any frequency, all of the designs which have lower power density than this critical value are sub-optimal as further increase of power density would allow for an increase in efficiency as well.

Beside these direct conclusions, with some simple post-processing of these feasible MFT design sets, it is possible to expose all sorts of complex design trends featuring compound constraints.

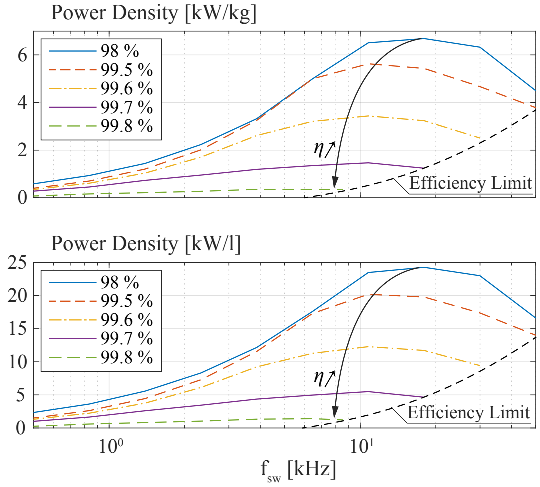

Fig. 8.5 Maximum achievable gravimetric (top) and volumetric (bottom) power density versus operating frequency plots for different minimum efficiency constraints for $N = 11$, $M = 1$, Si-Ferrite, solid insulated MFT

8.4.1 Switching Frequency and Efficiency

It is especially interesting to analyze the potential increase in power density that can be achieved with the increase of operating frequency under specified minimum efficiency constraint. This trend can easily be identified by means of filtering the maximum MFT design feasibility sets from **Fig. 8.4** by minimum allowed efficiency criteria and selection of designs with maximum power density for each frequency.

The family of curves, representing maximum achievable gravimetric and volumetric power densities versus operating frequency, for different minimum efficiency constraints, are presented in **Fig. 8.5**. It can be seen that it is not possible to achieve the scaling such as estimated with (2.10) for higher frequencies. For each minimum efficiency constraint, there exists a Pareto optimal frequency at which the maximum achievable MFT power density is at its apex. For higher frequencies, the additional frequency dependent losses start to dominate, thus preventing further scaling. Furthermore, it can be seen that, as the minimum efficiency constraint is tightened, the maximum achievable power densities decrease, as well as the feasible design set frequency range. It is also interesting to notice that Pareto optimal frequencies are lower for MFT designs with higher efficiency requirement.

8.4.2 Switching Frequency and Insulation Voltage

Taking into account the assumptions described in **Sec. 8.3.1**, it is possible to perform a simplified analysis of the influence of the required insulation level, by comparing feasible MFT design sets with different minimum dielectric distance constraints, corresponding to different insulation voltage requirements, according to (8.12). An example of the maximum achievable gravimetric and volumetric power density versus operating frequency plots for different insulation requirements are displayed in **Fig. 8.6**, for $N = 11$, $M = 1$, Si-Ferrite MFT with both insulation alternatives. As can be seen, the maximum achievable power density is lower in case of the MFT design with higher insulation voltage. This is an expected result, as the higher insulation level requires larger dielectric distances and therefore more volume is occupied for this function.

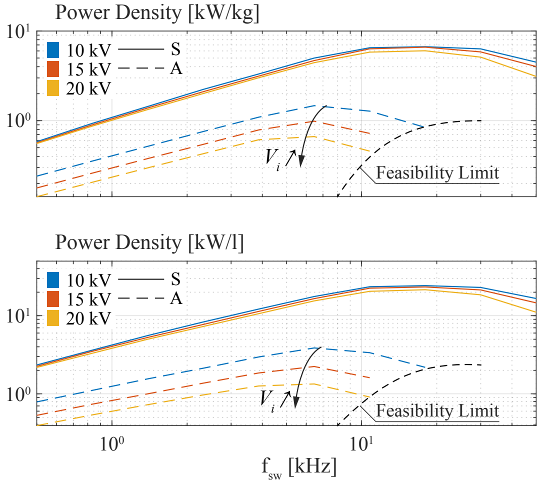

Fig. 8.6 Maximum achievable gravimetric (top) and volumetric (bottom) power density versus operating frequency plots for different insulation requirements for $N = 11$, $M = 1$, Si-Ferrite, solid (S) and air (A) insulated MFT

Moreover, it can be seen that the air insulated design is much more sensitive to the increase of the insulation voltage compared to the solid insulated alternative. As given in **Tab. 8.4**, epoxy resin has much better dielectric properties than air which lead to proportionally smaller increase in dielectric spacing, according to (8.12). Design optimization algorithm optimizes the active part of the transformer, windings and the core, whereas the minimum insulation distances must be respected for a chosen dielectric.

Consequently, dielectric properties of the insulation material determine the sensitivity of the volume and weight of the MFT design to the increase of insulation requirements. Air insulated designs will require large volume to accommodate MV applications, due to relatively poor dielectric properties of the air compared to epoxy, but they benefit from the inherent property of self healing and avoid relatively complex and expensive epoxy casting. While, air pollution and its varying properties are always a concern when it comes to air insulation, solid cast insulation suffers electrical, thermal and mechanical stress due to non equal expansion of various materials in contact which may, cause cracks over time. Moreover, any epoxy casting imperfections (e.g. air bubbles) may cause sufficiently strong local field gradients that can cause PD and eventually annihilation of dielectric properties.

Provided that a reliable data base of various insulating materials is available, insulation coordination could as well be integrated into design optimization, thus allowing the selection of the most optimal alternative.

8.4.3 Optimal Number Of ISOP Connected Cells

As discussed earlier, some type of modular series connected structure is necessary on the MV side, depending on the selected power semiconductor module blocking voltages. Taking into account the variety of available semiconductor devices and projections for the future power modules with extended operation range, as listed in **Tab. 8.1**, the number of ISOP connected DC-DC converter cells represents a design choice. Similar to operating frequency, this degree of freedom is analyzed from the aspect of potential MFT optimization. A maximum feasible design set is generated for all mentioned MFT design variations, for each possible number of ISOP cascaded cells from **Tab. 8.1**, as given in **Fig. 8.7**.

It can be seen that the downward slope of Pareto-front, showing the trade-off between efficiency and power density, becomes steeper with the increase of the number of cascaded cells. Consequently, maximum achievable MFT efficiency, for a given power density, decreases with the increase of N. This result is in line with the qualitative analysis from **Sec. 2.2**. Increase of N results in more DC-DC converter cells with lower power rating according to (8.3) and, as can be seen from **Tab. 2.1**, relative losses are reverse proportional to MFT unit of size and indirectly to rated power.

It is interesting to notice how this trend is influenced by the insulation material. As can bee seen, the Pareto fronts of the air insulated designs are much more affected by the increase of N compared to solid insulated counterparts. This is due to the fact that the size of the active parts of the transformer, winding and core cross sections, decrease with the mentioned power decrease, whereas the dielectric distances must remain the same in order to accommodate full input voltage insulation of 10kV regardless of N, as discussed in **Sec. 8.3.1**. Therefore, insulation occupies a higher relative portion of the MFT as the N increases. Higher relative dielectric distances cause larger relative mean lengths of the windings and magnetic flux path, thus increasing the volume where core and winding losses are present resulting in decreased efficiency. This effect is much stronger for air insulated designs where minimum dielectric widths are significantly higher compared to those that can be achieved with solid insulation.

It can as well be seen how the thermal limit relaxes with the increase of N. This result is also in line with the qualitative analysis. As can be seen from **Tab. 2.1**, temperature rise is proportional to the MFT unit of size and indirectly to rated power. In other words, lower power rated transformer units have larger relative cooling surfaces compared to the high power rated units, thus less efficient designs are thermally feasible.

While **Fig. 8.7** shows the ”theoretical” maximum MFT design feasibility sets, where all of the switches from **Tab. 8.1** are available and can switch in range of 0.5-50kHz, it is interesting to highlight which of these solutions can be realized with already available, ”real”, power semiconductor modules taking into account their switching frequency limitations. Bar plots, of maximum achievable gravimetric and volumetric power density versus the number of cascaded ISOP connected cells are presented in **Fig. 8.8**, denoting the real and theoretically feasible solutions for all of the design choice variations.

As can be seen, there is a clear difference between the real and theoretical solutions, especially for realizations that utilize power semiconductors modules with high blocking voltage (low N). As given in **Tab. 8.1**, higher blocking voltages yield lower maximum allowed switching frequencies due to semiconductor physics of available Si IGBTs. Therefore, the domain of practically feasible solutions is confined within this narrowed down frequency range. As the N increases, utilizing power semiconductor modules with lower blocking voltage that can switch faster, the suboptimality gap decreases.

As shown in **Figs. 8.5** and **8.6**, MFT designs with the given design combinations and requirements reach the highest power densities in the frequency range approximately between 10kHz and 20kHz. Therefore, from the point of view of the MFT power density, all of the DC-DC converter cell realizations utilizing the switches that can switch 25kHz and higher have zero optimality gap.

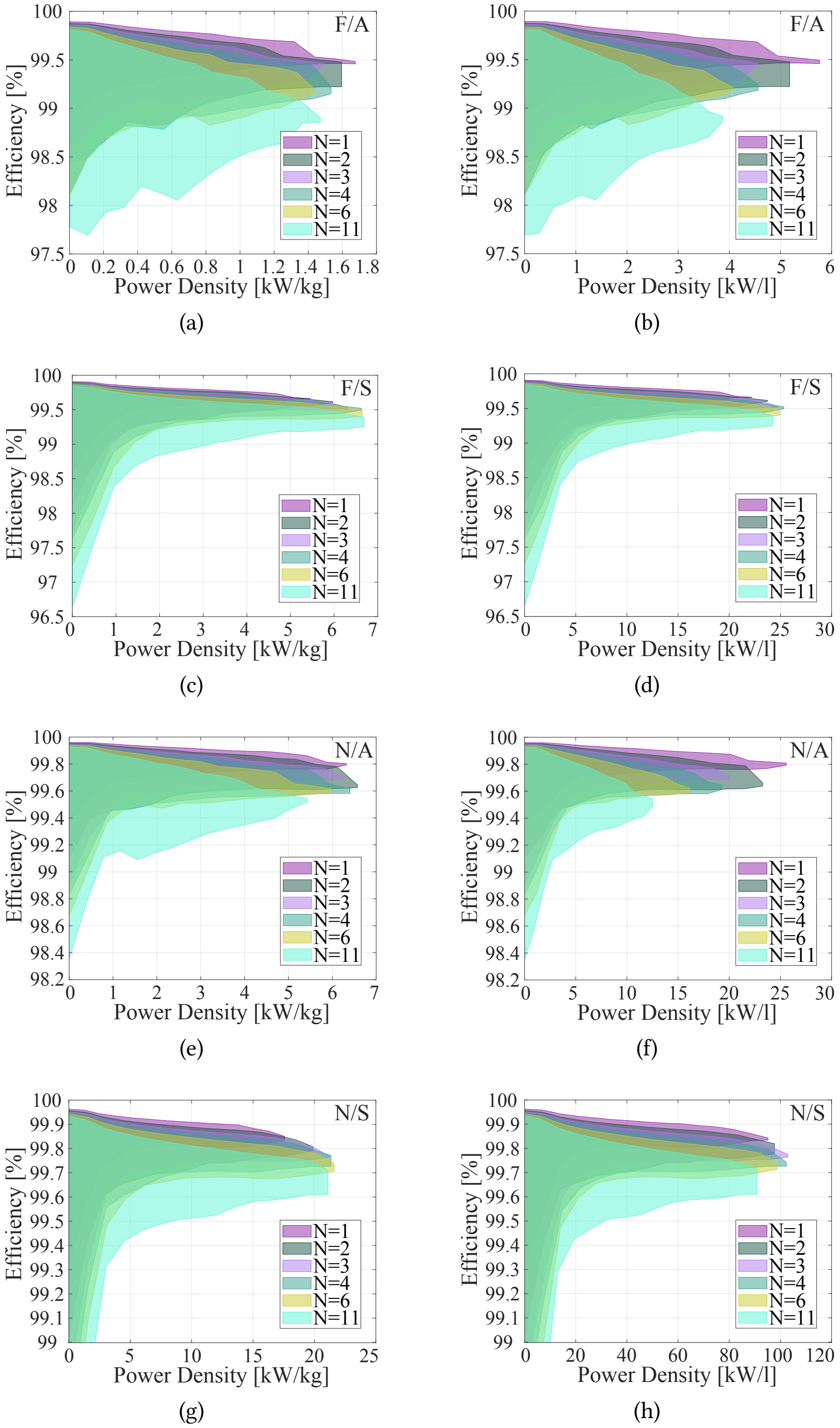

(a) (b)

(c) (d)

(e) (f)

(g) (h)

Fig. 8.7 Efficiency versus power density plots of maximum feasible MFT design sets, generated with the design optimization algorithm for each possible number of ISOP cascaded cells from **Tab. 8.1** for all mentioned design variations: Si-Ferrite (F), Nanocrystaline (N), air (A) and solid cast (S) insulated. Each cell is realized as a single DC-DC converter ($M = 1$).

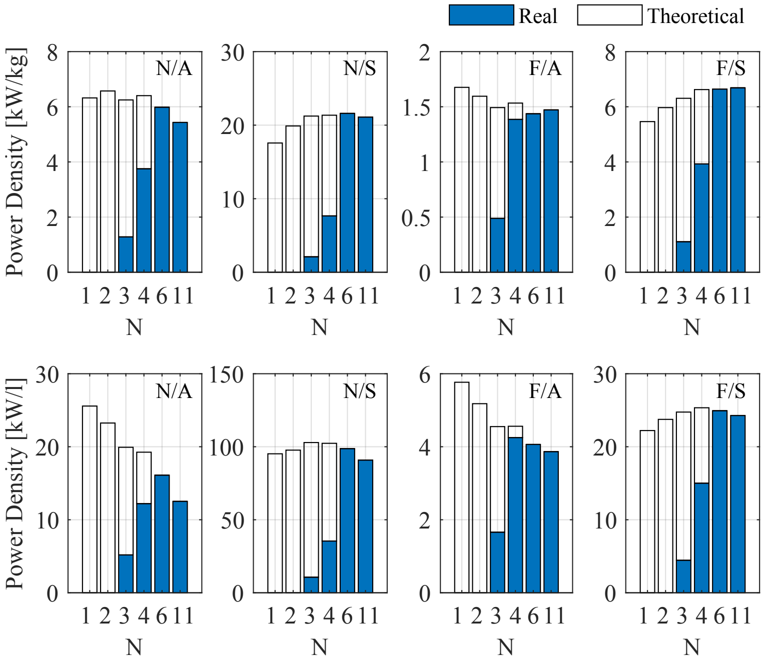

Fig. 8.8 Bar plots, of maximum achievable gravimetric and volumetric power density versus the number of cascaded ISOP connected cells, denoting the real (Si semiconductor based) and theoretically feasible (emerging SiC semiconductor based) solutions for all mentioned design variations: Si-Ferrite (F), Nanocrystaline (N), air (A) and solid cast (S) insulated. Each cell is realized as a single DC-DC converter ($M = 1$).

It can be observed that the maximum theoretically achievable volumetric power density of the MFT designs featuring air insulation significantly drops with the increase of N. Same as for efficiency, this can directly be explained by the fact that the necessary insulation occupies a higher relative portion of the MFT as the N increases, thus preventing the expected scaling.

On the other hand, for the solid insulated designs, maximum theoretical volumetric power densities are achieved at ($N = 3, 4$). The volume occupied by the insulation is not as significant in this case, due to the high dielectric strength of the epoxy resin. However, epoxy coating increases the thermal resistances of the windings and therefore these designs converge to their theoretical optimum at higher N where relative cooling conditions are easier.

Moreover it is interesting to notice that, depending on the particular case, nanocrystalline designs achieve around 3-4 times higher power densities compared to Si-Ferrite based alternative. Moreover, solid insulation allows for increase in gravimetric power density in range of 3-4 times and in volumetric power density in range of 3-7 times. Note that only the active part of the MFT, windings, core and insulation, are considered for the volume and weight calculation, as recommended metric for design comparison [49]. Therefore, these differences would amount to lower values after the inclusion of coolers, bushings and other assembly components.

From the aspect of solutions that can be realized with readily available power semiconductor modules, it can be seen that a substantial volume and weight reduction can be achieved with higher modularity (N), utilizing faster power semiconductor modules with lower blocking voltage. Moreover, when it comes to gravimetric power density, the optimal solutions that can be achieved with the existing devices at higher N are either better or not significantly suboptimal compared to the absolute theoretical maximum. This statement holds for the volumetric densities as well, except for the air insulated designs, where relative increase of insulation volume prevents the scaling.

This result shows that, as far as the MFT is concerned, for the considered design choices and under the assumption of smart technology coordination and design optimization, the utilization of faster switching semiconductors does not enable any further substantial power density increase of the MFT (there are obvious benefits on the converter level). Different variations of design choices and lower modularity may become more attractive, but the overall potential power density gain reaches a saturation at some point.

8.4.4 Optimal Number Of Parallel Connected DC-DC Converters Within a Cell

Similar to cascaded ISOP connection of DC-DC converter cells, each of the cells can as well be realized as a parallel connection of M DC-DC SRC converters. This is an interesting concept from the efficiency point of view. In most of applications, the given converter would very rarely operate at full load for which it is optimized. Unfortunately, the switching losses and losses in the passive components do not decrease proportionally to the load which usually has a significant impact on efficiency at light load conditions. Similar to concepts deployed in electric vehicle chargers, this type of modular structure allows to turn off an arbitrary number of parallel SRC cells at light load conditions, instead of lossy freewheeling, thus increasing the overall converter efficiency. Therefore, an optimized operation can be achieved in all conditions.

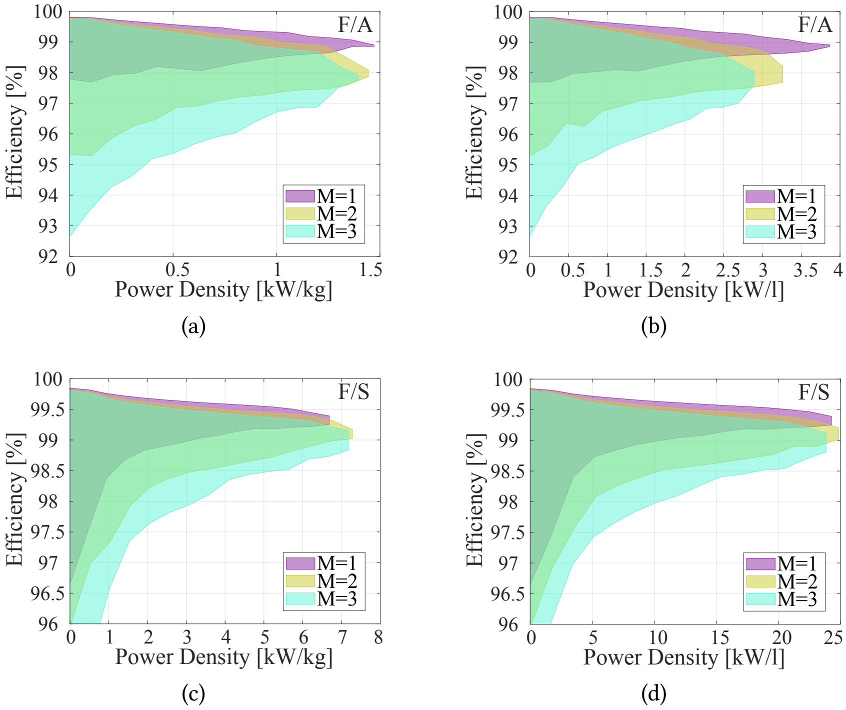

(a) (b)

(c) (d)

Fig. 8.9 Efficiency versus power density plots of maximum feasible MFT design sets, generated with the design optimization algorithm for different number of parallel connected DC-DC SRCs within a converter cell from **Fig. 8.1(a)** for the next design variations: Si-Ferrite (F), air (A) and solid cast (S) insulated where $N = 11$

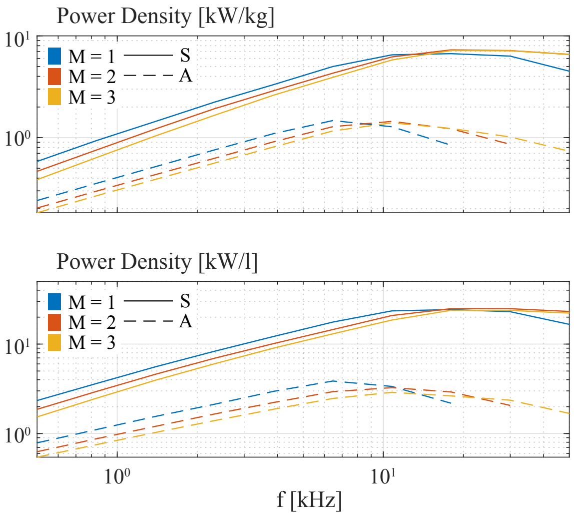

Fig. 8.10 Maximum achievable gravimetric (top) and volumetric (bottom) power density versus operating frequency plots for different number of parallel connected DC-DC SRCs within a cell for $N = 11$, Si-Ferrite, solid (S) and air (A) insulated MFT designs

Same as for the number of cascaded ISOP connected DC-DC converter cells, this type of modularity is analyzed from the aspect of potential MFT optimization. A maximum feasible design set is generated for all mentioned MFT design variations with Si-Ferrite core, for different number of parallel connected DC-DC SRCs within a converter cell from **Fig. 8.1(a)**, as displayed in **Fig. 8.9**.

Similar to the case of N, it can be seen that a price in MFT efficiency has to be paid for higher M modularity. Note that, unlike N, M influences only the required rated power of the MFT, whereas input-output voltages remain the same and thus insulation requirements as well. As already discussed in **Sec. 8.4.3**, the maximum achievable efficiency is lower for the lower power rated MFT designs, or higher M. However, due to better relative cooling conditions of lower power transformers, relaxing the thermal limit, high power densities can still be achieved in spite of decreased efficiency.

Maximum achievable gravimetric and volumetric power density versus operating frequency plots, for different number of parallel connected DC-DC SRCs within a cell, are presented in **Fig. 8.10**, for $N = 11$, Si-Ferrite, solid and air insulated MFT designs. While it can be seen that lower power rated MFT designs have inferior power density at lower frequencies, they maintain the scaling up to higher frequencies, achieving the highest power densities in some cases (e.g. for $M = 3$ and solid insulation). Easier cooling of lower power transformers makes designs on higher frequencies, where power loss density is higher, thermally feasible thus increasing the frequency range where MFT scales favorably.

The ultimate choice of M is a trade-off between how much the nominal converter efficiency can be compromised in favor of added flexibility, allowing for optimized (more efficient) operation at light load conditions. This choice should reflect the expected operating conditions in a way that minimizes the overall amortized losses.

8.5 Conclusion

One of the main drivers for SST operation at medium frequency is the potential to substantially decrease the size of magnetic components. Various design choices on a converter level have a significant influence on the required MFT characteristics and therefore need to be analyzed together. In order to fully explore the potential of this concept, an MFT design optimization is required to properly take into account all of the effects associated to medium-frequency high-power operation at MV and various design choices and materials. This work has considered a representative subset of possible technologies, which is by no means exhaustive and future work is still required.

Considering the targeted technical specifications, it was shown that for the considered variations of MFT design choices and materials, the highest power densities are achieved in approximate frequency range from 10kHz to 20kHz. While it might be possible to maintain the scaling up to slightly higher frequencies by implementing more efficient cooling, this would have an impact on efficiency, cost and system complexity. Further MFT scaling is tied to improvements from the material science - providing better transformer core and winding materials with better high frequency loss characteristic. Therefore, from the point of view of the MFT efficiency and power density, considering the analyzed variations of design choices and materials (covering the most relevant available and technically reasonable core and winding design choices), the operation at frequencies above these critical values does not bring any additional benefits for the scenario and ratings analyzed in this thesis. Furthermore, insulation requirements and the associated dielectric distances do not decrease with frequency increase (even need reinforcing), thus imposing severe constraints on maximum achievable power density.

Although the maximum achievable MFT power density reaches a saturation at mentioned frequencies, development of less lossy semiconductor modules capable of much faster switching is very beneficial from the converter efficiency point of view. Furthermore, the availability of the emerging semiconductors with extended blocking voltage range will offer additional design alternatives which may prove optimal for certain applications.

Finally, besides intuitively clear conclusions that MFT power density can be improved using stronger dielectric materials for insulation and better core materials (for the given frequency range), it was shown that by properly exploiting modularity, it is possible to achieve designs within the frequency range of the existing semiconductors, featuring high MFT power densities comparable to the theoretical maximum. On the other hand, emerging wide-bandgap devices will certainly improve the converter part of efficiency.

9

Conclusion and Future Work

9.1 Summary and Contributions

With the recent advancements in the power semiconductor industry, resulting in faster and more efficient switches with extended voltage and current capabilities, the SST concept has become increasingly attractive. Besides the power semiconductor modules, the central component of any SST, providing both the necessary galvanic insulation and input-output voltage matching, is the MFT. However, the progress of the magnetic components has not been following the same pace as the semiconductor industry leaving transformers as critical elements - limiting the converter efficiency and power density.

The basic motivation and technical challenges tied to transformer operation at medium frequency within power electronic applications are described in **Chapter 2**, together with the state of the art. In contrast to traditional line frequency transformers (LFTs), normally operating at low grid frequency with sinusoidal voltage and current excitation, MFTs operate at higher switching frequencies with square voltage and in general non-sinusoidal current waveforms, characteristic for the given power electronic converter topology. According to the scaling laws, there is a great potential for the reduction of the MFT size and relative cost with the increase of the operating frequency. However, this frequency scaling is tied to several challenges. From the electromagnetic aspect, the operation at elevated frequencies leads to: (i) additional losses due to skin and proximity effect within the windings and eddy currents within the laminated cores; (ii) increased dielectric stress due to high dV/dt, characteristic for the square voltage pulses within power electronic converters. Additionally, non-sinusoidal current waveform, containing higher order harmonics, results in further increase of the frequency dependent winding losses.

Moreover, the size decrease on its own implies decreased cooling surfaces resulting in higher thermal impedance towards the ambient and higher hot-spot temperature gradients. In addition to this, the high frequency core and winding structures feature material anisotropy making the electromagnetic and thermal coordination even more coupled and complex. Moreover, correct design of electric parameters is essential for the proper operation of the given converter and therefore imposes strict requirements on the accuracy of the corresponding models. With respect to the variety of the applications and depending on the converter topology, MFT specifications can vary drastically from one application to another. In other words, unlike traditional LFTs where the requirements and materials are standardized, MFTs have not yet reached the technological maturity, thus leaving many areas open for research.

Therefore the design of the MFTs is a complex task, featuring nonlinear coupled multi-physics. The need for design customization within the wide range of specifications, required in various power electronic applications, while taking into account a relatively large number of design choices, can only be served with a well established design optimization framework, powered by advanced models featuring a wide application range.

An analysis of the state-of-the art is provided in respect to the required specifications and selected technologies and materials. While it is hard to standardize the MFTs or provide some general design guidelines, some outlines of the dominant technologies and materials can be established. These are further discussed in **Chapter 2** where a high level description of the MFT design optimization process is provided. Desired MFT features and relevant technologies and materials are identified and classified, forming the design space for the design optimization. The impact of each of these parameters is briefly discussed in a qualitative manner.

A review of the available analytical modeling techniques and the necessary developments for their application on various MFT structures are provided in **Chapter 4**. Appropriate MFT modeling for design optimization is not straightforward. Besides the accuracy requirements, facilitating any optimization scheme implies hard constraints in terms of computational cost, thus in general excluding the possibility of direct application of very sophisticated numeric tools such as FEM. That is where the light weight analytical models perform extremely well as long as the necessary approximations/assumptions hold within reasonable accuracy limits.

Several modifications are proposed improving the accuracy and application range of the critical models, allowing to better address the high-power MV medium-frequency applications. Especially, a correction of the Dowel's frequency dependent leakage inductance model via Rogowski factor is proposed allowing to properly take into account the non-ideal core-window fill-factors characteristic for MV applications where dielectric distances are increased in order to facilitate the appropriate insulation level. A detailed thermal network model is derived, allowing to take into account the 3D structure of the MFT and the anisotropy of its solid components - the core and the windings.

While light weight analytical models, such as described in **Chapter 4** can solve a large part of the problem, still many phenomena cannot be accurately described in that way. **Chapter 5** proposes a computationally efficient, yet sufficiently accurate, statistical data-driven modeling framework based on FEM simulations of simple geometry details and muti-variable polinomial fitting. The proposed modeling framework has been described in detail, showing how it is possible to transform, generalize and normalize a numerically difficult problem up to the point where a sufficiently small set of significant influences (variables) can be very efficiently captured via a neural-network inspired multi-variable polynomial model. Although already very fast (three-four orders of magnitude compared to simple 2D FEM models), these models can also be reorganized for most optimal execution depending on the specific design optimization algorithm and potentially achieve an even more drastic speed improvement. Moreover, a good estimation accuracy is achieved, with errors less than 5% relative to the 3D FEM and less than 10% relative to the measurements. Even beyond the specific models described in this thesis, this type of modeling framework allows further inclusion of complex effects, which cannot be analytically approximated within reasonable accuracy limits or numerically solved within reasonable time, within the design optimization loop.

A synthesis of all the presented models into a brute-force based design optimization algorithm, capable of generating sets of all feasible MFT design alternatives, is presented in **Chapter 6**. Utilizing a certain set of heuristics as a sort of branch and bound conditions, it is possible to drastically improove the performance of this algorithm. A detailed description of the proposed design optimization procedure is provided on an example of the 100kW, 10kHz MFT designed for the operation within the SRC, featuring integrated resonant tank.

In contrast to analysis of one or multiple sets of Pareto-optimal solutions, characteristic for formal optimization algorithms, this approach allows the designer to interactively select the best design trade-off in a very simple and intuitive way and provides great flexibility to choose between multiple design alternatives with very similar performance and specifications, but comprised of different components in case some are unavailable or too costly to be customized. Therefore, not only the characteristics of the MFT design itself, but also the whole design process and the prototype realization can be optimized.

With the described two step approach, the proposed method minimizes the sub-optimality gap between the theoretical and standard MFT designs, comprised of off-the-shelf components, and inherently provides a valuable insight into the positioning of the solutions utilizing specific hardware relative to all theoretically possible designs in a clear and intuitive way. This may be a very valuable input when it comes to component standardization, as it can clearly be seen what core or wire geometries are covering which MFT power, voltage and efficiency ranges.

As a proof of concept, a 100kW, 10kHz, air insulated and air cooled shell type MFT prototype has been realized utilizing square litz wire for windings and N87 SIFERRIT U-cores. As described in **Chapter 7** the prototype was subjected to thorough testing, including: electric parameter identification, PD test, loading test and a 9-hour thermal run within the realized back-to-back resonant test setup. These measurement results have confirmed the high fidelity of the developed modeling and the practicality of the proposed design optimization methodology - offering a powerful robust-design framework.

With the established design methodology and reliable models, a technology coordination and an MFT design sensitivity study have been performed on the SST level, as given in **Chapter 8**. A 0.5MW, 10kV ISOP SRC based converter topology has been selected for the case study, taking into account different available semiconductor ratings and the resulting converter modularity. This study has shown that, considering the most popular/relevant available technologies and materials, the expected MFT power density reaches its apex at around 10 – 20kHz. While modern wide-band-gap semiconductors will for sure increase the efficiency and power density of the converter stage, this result indicates that further size reduction of the magnetic components above these frequencies will only be possible through improvements in the materials - providing core and winding materials with better high frequency loss characteristic.

9.2 Overall Conclusions

From the work presented in the thesis and experience gained by the author, it can be concluded that SSTs are not a mature technology and there are still no standards related to any MFT requirement. This is challenging from the design point of view, as a broad spectrum of requirements and different design choices has to be taken into account. This can be done properly only through a well established and flexible design optimization framework.

Many commercial technologies can either be used directly or with few modifications in the future SSTs and MFTs. A cross-comparison of all feasible design alternatives, considering the representative available MFT technologies shows that the MFT scaling reaches its apex at frequencies around

10 – 20kHz. While it might be possible to maintain the scaling up to slightly higher frequencies by implementing more efficient cooling, this would have an impact on efficiency, cost and system complexity. Moreover, by properly exploiting the converter modularity, it is possible to achieve designs within the frequency range of the commercial semiconductors, featuring high MFT power densities comparable to the theoretical maximum.

Although the maximum achievable MFT power density reaches a saturation at mentioned frequencies, development of less lossy semiconductor modules capable of much faster switching is very beneficial from the converter efficiency point of view. Furthermore, the availability of the emerging semiconductors with extended blocking voltage range will offer additional design alternatives which may prove optimal for certain applications.

9.3 Future Work

The work in this thesis opens up new avenues on both MFT and SST design and development. A further exploration of the maximum achievable performance and limitations of various design alternatives, considering the available technologies, may lead to some general design guidelines as a precursor to eventual standardization.

From a modeling and design optimization point of view, the proposed SDDM modeling framework shows great promise. In order to fully utilize the material, the design margins need to be kept at a minimum. This requires precise modeling of the given phenomena at the design optimization stage. With SDDMs, it is possible to include complex phenomena, such as local electric field maximums and magnetic energy within asymmetric winding geometry, into the main design optimization loop. In other words, this allows to elegantly take into account all of the relevant effects and optimize the design in respect to all of the associated implications and constraints, thus avoiding blind over-dimensioning due to non-modeled effects and achieving a truly optimal design. Further propagation of these models will allow for an increasing number of effects to be taken into account at the design optimization stage leading to better quality designs.

Appendices

A

Test Setup Instruments

A list of the measurement instruments and power supplies, utilized within the back-to-back resonant test setup, is provided here.

A.1 Used Instruments

Tab. A.1 Measurement instruments and power supplies within the back-to-back resonant test setup

Device	Specification
Differential voltage probes	SI-9010
Eight channel oscilloscope	YOKOGAWA DLM4058
Control and PWM signal generation platform	ABB AC 800PEC rig
3-phase bridge	SEMIKRON SKIIP 110 NAK
Power supply 1 of primary side DC bus	2 x DELTA ELEKTRONIKA SM 600-10 in master-slave series connection
Power supply 2 of primary side DC bus	TECHNIX SRK20KV-100KW
Low-voltage high-current power supply for power circulation in CCM	MAGNA POWER TSD20-2250/380+LXI
Thermocouple probes attached to the wireless transmitter/receiver	OMEGA SCASS-020U-12
Thermal camera	FLIR-E64501

Where CCM and VCM stand for current and voltage controlled mode, respectively. Depending on the availability, two different power supplies (1 and 2) were alternatively used to control the primary side DC bus

Bibliography

[1] *Watermill, from Wikipedia, the free encyclopedia.* `https://en.wikipedia.org/wiki/Watermill`.

[2] "Triumph of AC. 2. The battle of the currents," *IEEE Power and Energy Magazine*, vol. 1, no. 4, pp. 70–73, Jul. 2003.

[3] *War of the currents, from Wikipedia, the free encyclopedia.* `https://en.wikipedia.org/wiki/War_of_the_currents`.

[4] International Electrotechnical Commission, "Power transformers - Part 1: General," en, International Electrotechnical Commission, Geneva, CH, Standard IEC 60076-1:2011, 2011.

[5] *Faraday's law of induction, from Wikipedia, the free encyclopedia.* `https://en.wikipedia.org/wiki/Faraday's_law_of_induction`.

[6] *50 Hertz vs. 60 Hertz, from Next Kraftwerke.* `https://www.next-kraftwerke.com/knowledge/utility-frequency`.

[7] G. Neidhofer, "50-hz frequency [history]," *IEEE Power and Energy Magazine*, vol. 9, no. 4, pp. 66–81, Jul. 2011.

[8] W. McMurray, *Multipurpose power converter circuits.* U.S. Patent 3 487 289, Dec.30, 1969.

[9] W. McMurray, *Power converter circuits hav-ing a high frequency link.* U.S. Patent 3 517 300, June23, 1970.

[10] W. McMurray, "The thyristor electronic transformer: A power converter using a high-frequency link," *IEEE Transactions on Industry and General Applications*, vol. IGA-7, no. 4, pp. 451–457, Jul. 1971.

[11] U. Drofenik and F. Canales, "European trends and technologies in traction," in *2014 International Power Electronics Conference (IPEC-Hiroshima 2014 - ECCE ASIA)*, May 2014, pp. 1043–1049.

[12] D. Dujic, F. Kieferndorf, F. Canales, and U. Drofenik, "Power electronic traction transformer technology," in *Proceedings of The 7th International Power Electronics and Motion Control Conference*, vol. 1, Jun. 2012, pp. 636–642.

[13] N. Hugo, P. Stefanutti, M. Pellerin, and A. Akdag, "Power electronics traction transformer," in *2007 European Conference on Power Electronics and Applications*, Sep. 2007, pp. 1–10.

[14] D. Dujic, C. Zhao, A. Mester, J. K. Steinke, M. Weiss, S. Lewdeni-Schmid, T. Chaudhuri, and P. Stefanutti, "Power Electronic Traction Transformer-Low Voltage Prototype," *IEEE Transactions on Power Electronics*, vol. 28, no. 12, pp. 5522–5534, Dec. 2013.

[15] C. Zhao, D. Dujic, A. Mester, J. K. Steinke, M. Weiss, S. Lewdeni-Schmid, T. Chaudhuri, and P. Stefanutti, "Power Electronic Traction Transformer-Medium Voltage Prototype," *IEEE Transactions on Industrial Electronics*, vol. 61, no. 7, pp. 3257–3268, Jul. 2014.

[16] B. Engel, M. Victor, G. Bachmann, and A. Falk, "15kV/16.7Hz energy supply system with medium frequency transformer and 6.5kV IGBTs in resonant operation," in *Proceedings of the 10th European Conference on Power Electronics and Applications (EPE 2003), Toulouse*, 2003.

[17] J. Taufiq, "Power Electronics Technologies for Railway Vehicles," in *2007 Power Conversion Conference - Nagoya*, Apr. 2007, pp. 1388–1393.

[18] M. K. Das, C. Capell, D. E. Grider, S. Leslie, J. Ostop, R. Raju, M. Schutten, J. Nasadoski, and A. Hefner, "10 kV, 120 A SiC half H-bridge power MOSFET modules suitable for high frequency, medium voltage applications," in *2011 IEEE Energy Conversion Congress and Exposition*, Sep. 2011, pp. 2689–2692.

[19] D. Wang, J. Tian, C. Mao, J. Lu, Y. Duan, J. Qiu, and H. Cai, "A 10-kv/400-v 500-kva electronic power transformer," *IEEE Transactions on Industrial Electronics*, vol. 63, no. 11, pp. 6653–6663, Nov. 2016.

[20] U. Javaid, D. Dujić, and W. van der Merwe, "MVDC marine electrical distribution: Are we ready?" In *IECON 2015 - 41st Annual Conference of the IEEE Industrial Electronics Society*, Nov. 2015, pp. 000 823–000 828.

[21] U. Javaid, F. D. Freijedo, D. Dujic, and W. van der Merwe, "MVDC supply technologies for marine electrical distribution systems," *CPSS Transactions on Power Electronics and Applications*, vol. 3, no. 1, pp. 65–76, Mar. 2018.

[22] J. Uzair, "MVDC Distribution Fed High Power Multi-Motor Drives," PhD thesis, EPFL Lausanne, Switzerland, 2018.

[23] S. Kim, D. Dujic, and S. Kim, "Protection Schemes in Low-Voltage DC Shipboard Power Systems," in *PCIM Europe 2018; International Exhibition and Conference for Power Electronics, Intelligent Motion, Renewable Energy and Energy Management*, Jun. 2018, pp. 1–7.

[24] S. Kim, D. Dujic, and S. Kim, "Achieving Protection Selectivity in DC Shipboard Power Systems Employing Additional Bus Capacitance," in *IECON 2018 - 44th Annual Conference of the IEEE Industrial Electronics Society*, Oct. 2018, pp. 3377–3382.

[25] *Example of a MVDC distribution.* `www.english.hhi.co.kr`.

[26] *Example of a MVDC ship distribution.* `www.abb.com`.

[27] M. Mogorovic and D. Dujic, "Sensitivity Analysis of Medium-Frequency Transformer Designs for Solid-State Transformers," *IEEE Transactions on Power Electronics*, vol. 34, no. 9, pp. 8356–8367, Sep. 2019.

[28] M. Mogorovic and D. Dujic, "100 kW, 10 kHz Medium-Frequency Transformer Design Optimization and Experimental Verification," *IEEE Transactions on Power Electronics*, vol. 34, no. 2, pp. 1696–1708, Feb. 2019.

[29] D. Kalic and R. Radosavljevic, *Power Transformers*, Serb. K.B., Mar. 1995.

[30] C. W. T. McLyman, *Transformer and Inductor Design Handbook, Third Edition*, en. CRC Press, Mar. 2004.

[31] I. Villar, “Multiphysical Characterization of Medium-Frequency Power Electronic Transformers,” PhD thesis, EPFL Lausanne, Switzerland, 2010.

[32] C. R. Sullivan, “Optimal choice for number of strands in a litz-wire transformer winding,” *IEEE Transactions on Power Electronics*, vol. 14, no. 2, pp. 283–291, Mar. 1999.

[33] M. Jaritz and J. Biela, “Analytical model for the thermal resistance of windings consisting of solid or litz wire,” in *2013 15th European Conference on Power Electronics and Applications (EPE)*, Sep. 2013, pp. 1–10.

[34] *SIFERRIT material N87 data sheet, EPCOS*. `https://en.tdk.eu`.

[35] L. Heinemann, “An actively cooled high power, high frequency transformer with high insulation capability,” in *APEC. Seventeenth Annual IEEE Applied Power Electronics Conference and Exposition (Cat. No.02CH37335)*, vol. 1, Mar. 2002, 352–357 vol.1.

[36] *STS MF-Transformator für Traktion*. `www.sts-trafo.de`.

[37] H. Hoffmann and B. Piepenbreier, “Medium frequency transformer in resonant switching dc/dc-converters for railway applications,” in *Proceedings of the 2011 14th European Conference on Power Electronics and Applications*, Aug. 2011, pp. 1–8.

[38] H. Hoffmann and B. Piepenbreier, “High voltage igbts and medium frequency transformer in dc-dc converters for railway applications,” in *SPEEDAM 2010*, Jun. 2010, pp. 744–749.

[39] H. Hoffmann and B. Piepenbreier, “Medium frequency transformer for rail application using new materials,” in *2011 1st International Electric Drives Production Conference*, Sep. 2011, pp. 192–197.

[40] I. Villar, L. Mir, I. Etxeberria-Otadui, J. Colmenero, X. Agirre, and T. Nieva, “Optimal design and experimental validation of a medium-frequency 400kva power transformer for railway traction applications,” in *2012 IEEE Energy Conversion Congress and Exposition (ECCE)*, Sep. 2012, pp. 684–690.

[41] M. Steiner and H. Reinold, “Medium frequency topology in railway applications,” in *2007 European Conference on Power Electronics and Applications*, Sep. 2007, pp. 1–10.

[42] M. Bahmani, “Design and Optimization Considerations of Medium-Frequency Power Transformers in High-Power DC-DC Applications,” PhD thesis, Chalmers University of Technology Gothenburg, Sweden, 2016.

[43] G. Ortiz, “High-Power DC-DC Converter Technologies for Smart Grid and Traction Applications,” PhD thesis, ETH Zurich, Switzerland, 2014.

[44] M. Leibl, G. Ortiz, and J. W. Kolar, “Design and experimental analysis of a medium-frequency transformer for solid-state transformer applications,” *IEEE Journal of Emerging and Selected Topics in Power Electronics*, vol. 5, no. 1, pp. 110–123, Mar. 2017.

[45] G. Ortiz, M. G. Leibl, J. E. Huber, and J. W. Kolar, “Design and experimental testing of a resonant dc-dc converter for solid-state transformers,” *IEEE Transactions on Power Electronics*, vol. 32, no. 10, pp. 7534–7542, Oct. 2017.

[46] T. Gradinger, U. Drofenik, and S. Alvarez, “Novel Insulation Concept for an MV Dry-Cast Medium-Frequency Transformer,” in *19th European Conference on Power Electronics and Applications (EPE’17 ECCE Europe)*, Warsaw, Poland, 2017., pp. 1–10.

[47] S. Isler, T. Chaudhuri, D. Aguglia, and A. Bonnin, “Development of a 100 kW, 12.5 kV, 22 kHz and 30 kV Insulated Medium Frequency Transformer for Compact and Reliable Medium Voltage Power Conversion,” in *Proceedings of the 19th European Conference on Power Electronics and Applications (EPE 2017 - ECCE Europe), Warsaw, Poland*, 2017.

[48] T. P. H. Guillod, “Modeling and Design of Medium-Frequency Transformers for Future Medium-Voltage Power Electronics Interfaces,” PhD thesis, ETH Zurich, Switzerland, 2018.

[49] C. W. T. McLyman, *Designing magnetic components for high frequency DC-DC converters*, en. KG Magnetics, Feb. 1993.

[50] T. Appel and D. Benner, “Fundamental Investigation of very fast Transients in Power-Electronic Winding for Solid-State Transformers,” in *19th European Conference on Power Electronics and Applications (EPE’17 ECCE Europe)*, Warsaw, Poland, 2017., pp. 1–10.

[51] Z. Ouyang, O. C. Thomsen, and M. A. E. Andersen, “Optimal design and tradeoff analysis of planar transformer in high-power dc–dc converters,” *IEEE Transactions on Industrial Electronics*, vol. 59, no. 7, pp. 2800–2810, Jul. 2012.

[52] C. Quinn, K. Rinne, T. O’Donnell, M. Duffy, and C. O. Mathuna, “A review of planar magnetic techniques and technologies,” in *APEC 2001. Sixteenth Annual IEEE Applied Power Electronics Conference and Exposition (Cat. No.01CH37181)*, vol. 2, Mar. 2001, 1175–1183 vol.2.

[53] *ISE Magnetics*. `https://www.isemagnetics.com`.

[54] *Payton Planar*. `http://www.paytongroup.com/Planar_Transformers`.

[55] S. S. Baek, S. Bhattacharya, B. Cougo, and G. Ortiz, “Accurate equivalent circuit modeling of a medium-voltage and high-frequency coaxial winding dc-link transformer for solid state transformer applications,” in *2012 IEEE Energy Conversion Congress and Exposition (ECCE)*, Sep. 2012, pp. 1439–1446.

[56] M. Mogorovic and D. Dujic, “High-Power Medium-Frequency Transformer Design Optimization,” pp. 1–120.

[57] *STO-50 Silicone Transformer Oil, Clearco.* `http://www.clearcoproducts.com/silicone_transformer_oil.html`.

[58] T. Belgrand and R. Lemaître, “Grain Oriented Electrical Steel for Solid State Transformers,” in *ECPE Workshop: New Technologies for Medium-Frequency Solid-State Transformers in Lausanne, Switzerland, 2019.*

[59] *FINEMET F3CC Series Cut Core and material properties data sheet, Hitachi Metals, Ltd.* `https://www.hitachi-metals.co.jp`.

[60] C. C. Barry and N. M. Grant, *Ceramic Materials.* Springer, 2014.

[61] *Table of basic conductor properties: Resistivity and Temperature Coefficients.* `http://230nsc1.phy-astr.gsu.edu/hbase/Tables/rstiv.html`.

[62] *Table of metals and alloys densities: The Engineering ToolBox.* `https://www.engineeringtoolbox.com`.

[63] D. C. Jiles and D. L. Atherton, “Theory of ferromagnetic hysteresis (invited),” *Journal of Applied Physics*, vol. 55, no. 6, pp. 2115–2120, Mar. 1984.

[64] F. Preisach, “Über die magnetische Nachwirkung,” de, *Zeitschrift für Physik*, vol. 94, no. 5-6, pp. 277–302, May 1935.

[65] J. Chan, A. Vladimirescu, X.-C. Gao, P. Liebmann, and J. Valainis, “Nonlinear transformer model for circuit simulation,” *IEEE Transactions on Computer-Aided Design of Integrated Circuits and Systems*, vol. 10, no. 4, pp. 476–482, Apr. 1991.

[66] G. Bertotti, “Some considerations on the physical interpretation of eddy current losses in ferromagnetic materials,” *Journal of Magnetism and Magnetic Materials*, vol. 54, pp. 1556–1560, Feb. 1986.

[67] D. Lin, P. Zhou, W. Fu, Z. Badics, and Z. Cendes, “A dynamic core loss model for soft ferromagnetic and power ferrite materials in transient finite element analysis,” *IEEE Transactions on Magnetics*, vol. 40, no. 2, pp. 1318–1321, Mar. 2004.

[68] K. Venkatachalam, C. Sullivan, T. Abdallah, and H. Tacca, “Accurate prediction of ferrite core loss with nonsinusoidal waveforms using only Steinmetz parameters,” in *Proc. of IEEE Workshop on Computers in Power Electronics*, Jun. 2002, pp. 36–41.

[69] J. Reinert, A. Brockmeyer, and R. De Doncker, “Calculation of losses in ferro- and ferrimagnetic materials based on the modified Steinmetz equation,” *IEEE Transactions on Industry Applications*, vol. 37, no. 4, pp. 1055–1061, Jul. 2001.

[70] S. V. Kulkarni and S. A. Khaparde, *Transformer Engineering: Design and Practice.* Marcel Dekker, Inc., 2004.

[71] J. Muhlethaler, J. Biela, J. Kolar, and A. Ecklebe, “Improved core loss calculation for magnetic components employed in power electronic system,” in *2011 Twenty-Sixth Annual IEEE Applied Power Electronics Conference and Exposition (APEC)*, Mar. 2011, pp. 1729–1736.

[72] M. Luo, D. Dujic, and J. Allmeling, “Modeling frequency dependent core loss of ferrite materials using permeance-capacitance analogy for system-level circuit simulations,” *IEEE Transactions on Power Electronics*, pp. 1–1, 2018.

[73] A. Van den Bossche and V. C. Valchev, *Inductors and Transformers for Power Electronics.* Taylor & Francis, Mar. 2005.

[74] P. L. Dowell, “Effects of eddy currents in transformer windings,” *Proc. of the Institution of Electrical Engineers*, vol. 113, no. 8, pp. 1387–1394, Aug. 1966.

[75] J. A. Ferreira, “Improved analytical modeling of conductive losses in magnetic components,” *IEEE Transactions on Power Electronics*, vol. 9, no. 1, pp. 127–131, Jan. 1994.

[76] F. Robert, P. Mathys, and J. P. Schauwers, “The layer copper factor, although widely used and useful, has no theoretical base [smps transformers],” in *2000 IEEE 31st Annual Power Electronics Specialists Conference. Conference Proceedings (Cat. No.00CH37018)*, vol. 3, Jun. 2000, 1633–1638 vol.3.

[77] X. Nan and C. R. Sullivan, “An improved calculation of proximity-effect loss inhigh-frequency windings of round conductors,” in *IEEE Power Electronics Specialists Conference,June 2003*, vol. 3, Jun. 2003, pp. 853–860.

[78] A. Reatti and M. K. Kazimierczuk, “Comparison of various methods for calculating the AC resistance of inductors,” *IEEE Transactions on Magnetics*, pp. 1–1, 2002.

[79] J. A. Ferreira, “Aanalytical computation of ac resistance of round and rectangular litz wire windings,” *IEE Proceedings B - Electric Power Applications*, vol. 139, no. 1, pp. 21–25, Jan. 1992.

[80] F. Tourkhani and P. Viarouge, “Accurate analytical model of winding losses in round Litz wire windings,” *IEEE Transactions on Magnetics*, vol. 37, no. 1, pp. 538–543, Jan. 2001.

[81] K. Ilves, “Thermal modeling of a medium frequency transformer,” MSc Thesis. KTH, Stockholm, Sweden, 2009.

[82] *Convection From a Rectangular Plate.* http://people.csail.mit.edu/jaffer/SimRoof/Convection/.

[83] F. M. White, *Viscous Fluid Flow.* McGraw-Hill Higher Education, 2006.

[84] F. Dorfler and F. Bullo, “Kron Reduction of Graphs With Applications to Electrical Networks,” *IEEE Transactions on Circuits and Systems I: Regular Papers*, vol. 60, no. 1, pp. 150–163, Jan. 2013.

[85] M. Luo, D. Dujic, and J. Allmeling, "Leakage Flux Modeling of Medium-Voltage Phase-Shift Transformers for System-Level Simulations," *IEEE Transactions on Power Electronics*, vol. 34, no. 3, pp. 2635–2654, Mar. 2019.

[86] P. Hammond, "Roth's method for the solution of boundary-value problems in electrical engineering," *Proceedings of the Institution of Electrical Engineers*, vol. 114, no. 12, pp. 1969–1976, Dec. 1967.

[87] A. Fouineau and et al., "Semi-Analytical Methods for Calculation of Leakage Inductance and Frequency-Dependent Resistance of Windings in Transformers," in *IEEE Transactions on magnetics, 2018.*, pp. 1–10.

[88] M. Luo, D. Dujic, and J. Allmeling, "Leakage Flux Modeling of Multiwinding Transformers for System-Level Simulations," *IEEE Transactions on Power Electronics*, vol. 33, no. 3, pp. 2471–2483, Mar. 2018.

[89] J. Smajic, T. Steinmetz, M. Rüegg, Z. Tanasic, R. Obrist, J. Tepper, B. Weber, and M. Carlen, "Simulation and measurement of lightning-impulse voltage distributions over transformer windings," *IEEE Transactions on Magnetics*, vol. 50, no. 2, pp. 553–556, Feb. 2014.

[90] T. Župan, B. Trkulja, R. Obrist, T. Franz, B. Cranganu-Cretu, and J. Smajic, "Transformer windings' rlcparameters calculation and lightning impulse voltage distribution simulation," *IEEE Transactions on Magnetics*, vol. 52, no. 3, pp. 1–4, Mar. 2016.

[91] R. W. Erickson and D. Maksimovic, *Fundamentals of Power Electronics*, en. Springer US, Jan. 2001.

[92] J. Wojtkun, B. Bródka, and D. Stachowiak, "The influence of core geometry on no-load losses of medium power transformers," in *2018 International Interdisciplinary PhD Workshop (IIPhDW)*, May 2018, pp. 123–127.

[93] A. Kahveci, P. Szary, F. Herget, A. K. Putri, and K. Hameyer, "Methods for hysteresis losses determinations at non-standard ring core geometries equivalent to epstein measurements," in *2016 6th International Electric Drives Production Conference (EDPC)*, Nov. 2016, pp. 135–142.

[94] D. Robertson, "Magnetic Losses in Cores of Various Shapes," in *Nuclear Instruments and Methods 5 (1959) 133–141, North-Holland Publishing co.*.

[95] M. Puskarczyk, B. Jamieson, and W. Jurczak, "The influence of Core Shape and Material Nonlinearities to Corner Losses of Inductive Element," in *Excerpt from the Proceedings of the 2013 COMSOL Conference in Rotherdam.*

[96] M. Luo and D. Dujić, "Permeance based modelling of the core corners considering magnetic material nonlinearity," in *IECON 2015 - 41st Annual Conference of the IEEE Industrial Electronics Society*, Nov. 2015, pp. 000 950–000 955.

[97] C. Perez-Rojas, "Fitting saturation and hysteresis via arctangent functions," *IEEE Power Engineering Review*, vol. 20, no. 11, pp. 55–57, Nov. 2000.

[98] M. Mogorovic and D. Dujic, "Computationally Efficient Leakage Inductance Estimation of Multi-Winding Medium Frequency Transformers," in *PCIM Europe 2019; International Exhibition and Conference for Power Electronics, Intelligent Motion, Renewable Energy and Energy Management*, May 2019, pp. 1–6.

[99] M. Luo, D. Dujic, and A. J., "Test Setup for Characterisation of Biased Magnetic Hysteresis Loopsin Power Electronic Applications," in *The 2018 International Power Electronics Conference (IPEC)*, Niigata, Japan, 2018., pp. 422–426.

[100] U. Drofenik, "A 150kW Medium Frequency Transformer Optimized for Maximum Power Density," in *2012 7th International Conference on Integrated Power Electronics Systems (CIPS)*, Mar. 2012, pp. 1–6.

[101] M. Mogorovic and D. Dujic, "Medium Frequency Transformer Design and Optimization," in *PCIM Europe 2017; International Exhibition and Conference for Power Electronics, Intelligent Motion, Renewable Energy and Energy Management*, May 2017, pp. 423–430.

[102] A. Garcia-Bediaga, I. Villar, A. Rujas, L. Mir, and A. Rufer, "Multiobjective optimization of medium-frequency transformers for isolated soft-switching converters using a genetic algorithm," *IEEE Transactions on Power Electronics*, vol. 32, no. 4, pp. 2995–3006, Apr. 2017.

[103] D. Phaengkieo and S. Ruangsinchaiwanich, "Optimization of three-phase transformer design using adaptive genetic algorithm," in *2016 19th International Conference on Electrical Machines and Systems (ICEMS)*, Nov. 2016, pp. 1–5.

[104] A. K. Janjua, S. N. Mughal, and A. Z. Khan, "Transformer's core size optimizaiton using genetic algorithm," in *2015 6th International Conference on Intelligent Systems, Modelling and Simulation*, Feb. 2015, pp. 179–183.

[105] S. Zhang, Q. Hu, X. Wang, and Z. Zhu, "Application of chaos genetic algorithm to transformer optimal design," in *2009 International Workshop on Chaos-Fractals Theories and Applications*, Nov. 2009, pp. 108–111.

[106] S. Sudhoff, *Power Magnetic Devices: A Multi-Objective Design Approach*, en. Wiley-IEEE Press, 2014.

[107] M. Mogorovic and D. Dujic, "Thermal modeling and experimental verification of an air cooled medium frequency transformer," in *2017 19th European Conference on Power Electronics and Applications (EPE'17 ECCE Europe)*, Sep. 2017, P.1–P.9.

[108] M. Mogorovic and D. Dujic, "Medium frequency transformer leakage inductance modeling and experimental verification," in *2017 IEEE Energy Conversion Congress and Exposition (ECCE)*, Oct. 2017, pp. 419–424.

[109] M. Mogorovic and D. Dujic, "Modeling And Experimental Verification of Geometry Effects on Core Losses," in *10th International Conference on Power Electronics – ECCE Asia (ICPE 2019-ECCE Asia)*, May 2019, pp. 1–7.

[110] M. Mogorovic and D. Dujic, “Computationally Efficient Estimation of the Electric-Field Maximums for the MFT Insulation Coordination,” in *2019 IEEE Energy Conversion Congress and Exposition (ECCE)*, Oct. 2019, accepted.

[111] M. Claessens, D. Dujic, F. Canales, J. K. Steinke, P. Stefanutti, and C. Vetterli, “Traction Transformation: A Power-Electronic Traction Transformer (PETT),” *ABB Review, No: 1/12*, pp. 11–17, 2012.

[112] J. Huber and J. Kolar, “Optimum number of cascaded cells for high-power medium-voltage ac-dc converters,” in *IEEE Journal of Emerging and Selected Topics in Power Electronics*, vol. 5, Mar. 2017, pp. 213–232.

[113] Q. Zhu, L. Wang, L. Zhang, W. Yu, and A. Q. Huang, “Improved medium voltage ac-dc rectifier based on 10kv sic mosfet for solid state transformer (sst) application,” in *2016 IEEE Applied Power Electronics Conference and Exposition (APEC)*, Mar. 2016, pp. 2365–2369.

[114] D. Kaminski and A. Kopta, “Failure rates of HiPak modules due to cosmic rays (AN 5SYA 2042-04),” in *ABB Switzerland Ltd., Lenzburg, Switzerland: Tech. Rep., 2011.*.

[115] D. Dujic, A. Mester, T. Chaudhuri, A. Coccia, F. Canales, and J. K. Steinke, “Laboratory scale prototype of a power electronic transformer for traction applications,” in *Proceedings of the 2011 14th European Conference on Power Electronics and Applications*, Aug. 2011, pp. 1–10.

Marko Mogorovic

Doctoral Assistant - Power Electronics Laboratory

✉ *mogorovic.marko@gmail.com*
born on 02.08.1990
Serbia

HIGHER EDUCATION

École Polytechnique Fédérale de Lausanne, Lausanne, Switzerland

2015-2019 Ph.D., Doctoral program in Energy, Power Electronics Laboratory
Modeling and Design Optimization of Medium Frequency Transformers for Medium-Voltage High-Power Converters

2013-2015 M.Sc., Smart Grid Science and Technology
M.Sc. thesis *Techno-Economic Study of 3L-NPC Based Hybrid-Front-End Solutions utilizing discontinuous OPPs* (at ABB Switzerland, MV Drives R&D, Turgi)

School of Electrical Engineering, University of Belgrade, Serbia

2009-2013 B.Sc., Electrical Engineering: Electrical Power Systems and Drives
B.Sc. thesis *Function for calculation of pressure drops and temperature distribution within the oil transformer windings with labyrinth geometry*

TEACHING / SUPERVISION EXPERIENCE

2015-2016 Assistant for the course *Industrial Electronics I* (Modeling and control of grid connected converters)

2016-2019 Assistant for the course *Power Electronics* (Modeling and design of power electronics converters)

2018-2019 Two BSc semester projects supervision (*Core loss modeling and characterization of ferromagnetic materials for medium frequency*)

2018 MSc semester project supervision (*Analysis, simulation and experimental verification of dual active bridge load dynamics*)

2015 MSc summer internship supervision (*Mechanical design of two high power 3-phase bridge module assemblies with DC bus and gate signal adaptation*)

PROFESSIONAL EXPERIENCE

2015	Master project, ABB Switzerland, MV Drives R&D, Turgi, *Techno-Economic Study of 3L-NPC Based Hybrid-Front-End Solutions utilizing discontinuous OPPs*	6 months
2014	Internee, ABB Switzerland, MV Drives R&D, Turgi, *Study of maximum Power Capabilities of 3L - NPC, ANPC and NPP Voltage Source Converter Topologies Utilizing IGCTs*	6 months
2012	Internee, Schrack Technik, Sales Department, Serbia	2 months

LANGUAGES

English	Full working proficiency
German	B2 level
French	A1 level
Serbian	Native

COMPUTER TOOLS AND CODING

Simulation	Matlab simulink, PLECS, Ansys Maxwell, Comsol Multiphysics, PSpice, LabView
3D design	Solidworks, Inventor
Coding	Matlab, Python, C, C++, Assembly, Latex
OS	Windows, Unix

REVIEW

Regular reviewer for IEEE Transactions on Power Electronics and IEEE Transactions on Industrial Electronics, plus various conferences

Ce document a été imprimé au Centre d’impression EPFL,
imprimerie climatiquement neutre, certifiée myClimate.